Diffusion, reorientation and small magnetic fields

studied by μSR

Diffusie heroriëntatie en
kleine magnetische velden

onderzocht m.b.v. μSR

Diffusion, reorientation and small magnetic fields

studied by μSR

PROEFSCHRIFT

ter verkrijging van de graad van doctor
aan de Technische Universiteit Delft,
op gezag van de Rector Magnificus prof.ir. K.F. Wakker,
voorzitter van het College van Promoties,
in het openbaar te verdedigen

op maandag 5 november 2001 om 13:30 uur

door

Charles Theodorus KAISER

natuurkundig ingenieur
geboren te Noordwijkerhout

Dit proefschrift is goedgekeurd door de promotor:
Prof.dr. G.J. Kearley

Toegevoegd promotor: Dr. P.C.M. Gubbens

Samenstelling promotiecommissie:

Rector Magnificus, voorzitter
Prof.dr. G.J. Kearley, Technische Universiteit Delft, promotor
Dr. P.C.M. Gubbens, Technische Universiteit Delft, toegevoegd promotor
Prof.dr. S.F.J. Cox, University College London
Prof.dr. L.J. de Jongh, Universiteit Leiden
Prof.dr. I. de Schepper, Technische Universiteit Delft
Dr. U.A. Jayasooriya, University of East Anglia
Dr. A. Yaouanc, Commissariat à l'Energie Atomique
Prof.dr.ir. A.H.M. Verkooijen, Technische Universiteit Delft, reservelid

Printed in The Netherlands

Contents

Chapter 1

About this thesis

1.1 Introduction

The thread, that runs through this booklet is the use of muons to address a variety of physical problems. Here the spin of the muon will be used to give information on both static and dynamic physical properties of the compounds under study. In all of these studies this technique is used complementarily with others, in order to get additional information on the physics involved. The aim was to explore and extend the possibilities of this technique to provide unique information supporting some of the many different research projects within the department of Neutron scattering and Mössbauer spectroscopy at the Interfacultair Reactor Instituut in Delft. In this chapter the muon will be introduced by a brief overview of its history, and it applications in different fields of physics. After that, the different compounds studied will be introduced.

1.2   A brief history

The μ^+SR technique is based on the specific properties of the elementary particle known as the muon $\mu^\pm$. Muons were observed for the first time in cosmic ray experiments in the 1930's. It was noted that a certain particle penetrated deeper into the material than was possible for either electrons or protons [1]. One initially hoped the new particle was responsible for the strong nuclear force as postulated by Yukawa in 1935. The new particle however, appeared to have weak nuclear interaction with matter, in contradiction with his predictions. Later studies proved that the muon is actually born from the decay of the pion $\pi^\pm$, the particle predicted by Yukawa [2]. The muon appeared to have properties similar to the electron, but with a half life time τ_μ of 2.2 μs and a mass in between the proton and electron mass. The muon at this time was an unwanted child in the elementary particle family, as it undermined the accepted understanding of particle physics at that time. Inciting the famous physicist Rabi to his legendary question: "Who ordered that?" [3].

The muon disintegrates spontaneously by β-decay. The emission of positrons is most intense in the direction of the muon spin. This property is due to the non-parity conservation of the weak interaction, and was established for this decay by Garwin *et al.* [4]. The authors were well aware of the implications of this as is illustrated by their concluding remark: '...it seems possible that polarized positive and negative muons will become a powerful tool for exploring magnetic fields in nuclei, atoms and interatomic regions...'.

The development of particle accelerators in the 1950's enabled the production of pions and muons, and initiated muon experiments. Second generation accelerators and the creation of user facilities in the 1980's, gave an extra impulse to muon science. It has since developed into a technique applicable to a wide range of problems. On the one hand its practitioners are rigorously probing the fundamentals of quantum electrodynamics (QED) or exploring and developing the potential of muon catalysed fusion (μCF). On the other hand, solid state physicists are increasingly utilizing implanted muons to probe the static and dynamic properties of local magnetic fields to investigate both scientifically and technologically important aspects of magnetic and electronic phenomena in magnets and superconductors. Moreover the muon is used as a light isotope of hydrogen to study diffusion in metals and the influence of hydrogen impurities in semiconductors. Next to that, chemists have been using the muon to monitor chemical reactions involving radicals and dynamics of various organic compounds in different environments. Now looking back, seventy years after its discovery, we can conclude that the muon has indeed generously fulfilled its promise.

1.3   Brief introduction of the compounds under study

In this thesis three different compounds have been studied originating from various scientific disciplines and interests. The questions posed, for these various compounds, are connected to different experimental μSR techniques. A general introduction to these techniques will be given in chapter 2, followed by an accompanying theoretical survey in chapter 3. More details will be given in the relevant chapters. We will now introduce the compounds studied, with an outline of their physical interest.

Chapter 4 starts off with a study on a promising cathode material for rechargeable Li

batteries. The mobility of the Li charge carrier has been studied with μSR. The muon probes the nuclear moment of the Li ions. It has provided information of the Li diffusion additional to that of neutron diffraction and Nuclear Magnetic Resonance (NMR) results.

In catalysis nano-porous materials, like zeolites, are often used in separation and catalytic processes. In recent years the interest for organic molecules adsorbed in these materials has gained interest. The confinement of isolated molecules in the pores surrounded by charge compensating cations, will restrict the dynamics of these molecules. Chapter 5 deals with a model system of ferrocene in KY zeolite, in an attempt to characterize the dynamics of the ferrocene molecules.

In chapter 6 we report on the study of Pd nano-sized clusters. Their size puts the physical properties of these cluster intermediate between bulk and atomic behaviour. Recently, consequences have been observed in the thermodynamic properties of these clusters. These measurements have suggested an extremely small magnetic moment on the cluster due to one delocalized electron per cluster. As the muon is a very sensitive local probe for magnetism, it has been used to study this phenomenon.

Bibliography

[1] H. Muirhead *The Physics of elemetary particles* Pergamon Press, Oxford 1965

[2] C.M.G. Lattes, H Muirhead, G.P.S. Occhialini and C.F. Powel, Nature **159** 694 1947

[3] G. Hooft 't, *De bouwstenen van de Schepping*, Prometheus, Amsterdam

[4] R.L. Garwin, L.M. Lederman and M. Weinrich, Phys. Rev. **105** 1415 1957

Chapter 2

Experimental Techniques

2.1 Introduction

Muon Spin Rotation is the main experimental technique, and the link between the different chapters of this thesis. It is commonly indicated with the acronym μSR, which stands for Muon Spin Rotation, Relaxation or Resonance. Here we will only focus on the first two. This is a widespread technique nowadays, used in nuclear solid state physics and as the acronym already suggests, closely related to Nuclear Magnetic Resonance (NMR). It is based on the unique properties of the muon μ. The muon is an elementary particle with spin $\frac{1}{2}$. When the spin polarized muon is implanted in a material, the local magnetic field B_μ will exert a torque causing the muon spin S_μ to precesses with a Larmor frequency proportional to the field strength, $\omega_\mu = \gamma_\mu B_\mu$. After a given time the muon will decay and emit a positron. This decay positron is preferentially emitted along the direction of the muon spin. By collecting several millions of positrons one can reconstruct the muon spin depolarization function, reflecting both spatial and temporal distribution of the magnetic field at the muon site. This depolarization may then be interpreted in terms of local field distributions, fluctuations of local field, or sometimes muon diffusion through the sample. Here the general principles of the μSR technique will be discussed, including the muon production, its properties and implantation into the sample. Furthermore, the two common experimental geometries and some depolarization functions often used in data analysis will be introduced. For more details on the μSR technique the reader is referred to some comprehensive textbooks [1, 2, 3, 4].

2.2   Muon properties and production

The positive muon μ^+ is an elementary antiparticle, which together with its lighter counterpart the electron and the heavier tauon belongs to the family of leptons. Together with its accompanying neutrino's (ν_μ, $\bar\nu_\mu$), the charmed and the strange quarks and the corresponding antiparticles it forms the second generation of elementary particles. Although the negative muon μ^- is of importance in some particle physics experiments, e.g. muon catalysed fusion μCF, it is hardly used in solid state physics. So from here on we will mainly focus on the applications of the μ^+SR technique. Some properties of μ^+ are given in Table 2.1

Table 2.1: *Some properties of the μ^+ particle, compared to both electron and proton.*

mass	m_μ	206.763835(11) m_e
		0.1126096 m_p
charge		$+e$
spin	S_μ	$\frac{1}{2}$
magnetic moment	μ_μ	8.8905981(13) μ_N
		3.1833452(20) μ_p
gyromagnetic ratio	γ_μ	851.6 Mrad s^{-1} T^{-1}
	$\gamma_\mu/2\pi$	135.53879(1) MHz T^{-1}
lifetime	τ_μ	2.19714(7) μs

Intense beams of muons are commonly produced at intermediate energy particle accelerator facilities. Here a light target, usually graphite or berylium, is bombarded with high energy protons (~ 600 Mev). In the nuclear reactions induced by proton p collisions neutrons n and pions π^+ are produced:

$$p + p \rightarrow \pi^+ + p + n \qquad (2.1)$$
$$p + n \rightarrow \pi^+ + n + n$$

The pion itself is an unstable particle and decays within a lifetime of $\tau_\pi = 26$ ns into a muon and a muon neutrino:

$$\pi^+ \rightarrow \mu^+ + \nu_\mu \qquad (2.2)$$

This two body decay process forms the physical basis of μSR. Conservation of momentum requires the muon and its neutrino to be emitted in opposite directions for a frame of reference attached to π. Due to the parity violation of the weak interaction, the neutrino has a negative helicity, thus a spin antiparallel to its momentum. Because the pion has zero spin, and for reasons of conservation of angular momentum, the muon spin has to be directed opposite to its momentum as well (see Fig. 2.1). This results in a polarized muon beam. In this way, two different kinds of muon beams can be produced, according to the momentum of the pion upon decay. For the first, most commonly used in solid state physics, the muons used arise from pions at rest just below the surface of the
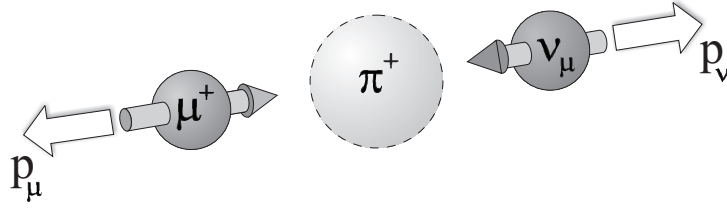
Figure 2.1: *The decay of π^+ into μ^+ and ν_μ. For reasons of conservation of angular momentum the muon spin S_μ is directed antiparallel to its momentum p_μ*

production target. These "surface" beams produce almost 100 % polarized muons with a comparatively low momentum ($\sim$30 MeV/c). This results in a typical range in matter of about 180 mg cm^{-2}, which is desirable if only a small amount of sample material is available [6]. In the second "conventional" muon beam, the pion decays in flight, usually in a long superconducting solenoid. Here the muon spins can be polarized parallel or antiparallel to their momentum, depending on whether they were emitted parallel or antiparallel to the pion momentum in the laboratory frame. Both types can be separated at the exit aperture of the solenoid, by momentum selection. Due to the finite kinematical acceptance of the decay channel, resulting in contamination by imperfect backward decays, the muon polarization of these beams is about 70 to 80 %. Here, stopping ranges in matter vary from 10 to 15 g cm^{-2} [6]. These beam types can also produce negative muons, because the pion decays in vacuum, whereas in a surface beam, the negative muon is immediately captured by the nuclei in the production target. After production the muons are directed to the dedicated μSR spectrometers by electromagnetic guide fields using bending magnets and focussing quadrupole magnets. Along this path electric/magnetic field separators can be included to remove contaminant particles (mainly positrons) from the muon beam. After implantation in the sample the muon will thermalize. Along the first part of its track the muon thermalizes by energy exchange through ionizing host atoms and creating vacancies. This however doesn't influence experimental results since the final area of localization will not be effected. Along the last part of its track the muon thermalizes by successive captures and dissociation of electrons from the host. The neutral bound state with an electron is known as muonium (μ^+e^-), an exotic light version of the hydrogen atom. In semi-conductors and insulators muonium can be stable, and it can even be incorporated in some organic materials. In metals, however, muonium finally dissociates, and the muon will localize at an interstitial site or vacancy. Here it will be surrounded by a charge screening cloud of conduction electrons of its host. The implantation and thermalization processes occur so rapidly (10^{-9} s) that depolarization is insignificant. At its localisation site the muon interacts with the surrounding matter. The muon carries a relatively large magnetic moment which even exceeds the largest nuclear moment μ_μ=3.2μ_p. It therefore acts as a very sensitive local magnetic field probe. However, due to the absence of a quadrupolar electric moment (S$_\mu$=$\frac{1}{2}$) the muon doesn't couple to electric field gradients. The second vital process of μSR is the weak interaction decay of the muon, with a lifetime of 2.2 μs into a positron (e$^+$) according to:

$$\mu^+ \rightarrow e^+ + \nu_e + \bar{\nu}_\mu \tag{2.3}$$

where ν_e and $\bar{\nu}_\mu$ are the neutrino and antineutrino associated with the positron and the
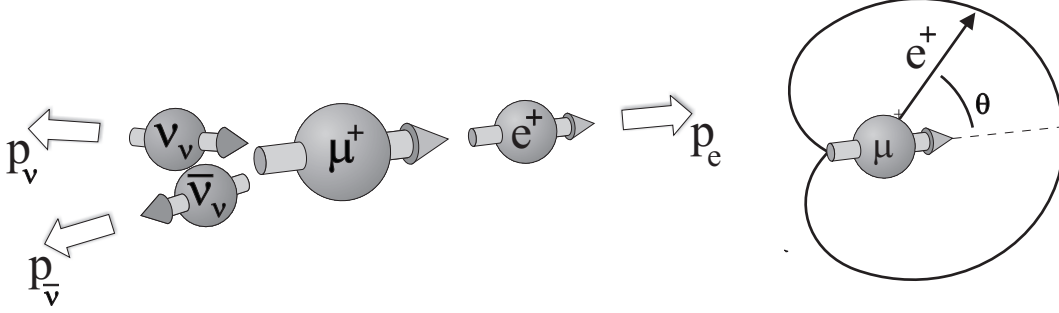
Figure 2.2: *Decay of the muon into a positron and two neutrino's. The angular distribution of the positron intensity illustrates the preference of positron emission along the muon spin direction*

muon respectively. Here the positron is preferentially emitted in the direction of the muon spin. This preference eventually allows the muon polarization to be monitored. The probability distribution of positron emission is given by:

$$W(\theta)d\theta \propto (1 + a\cos(\theta))d\theta \tag{2.4}$$

Here θ is the angle between muon spin and positron trajectory (see Fig. 2.2). The asymmetry parameter $a=1$ for maximum positron energy and $a=\frac{1}{3}$ when integrated over all positron energies. Since the positron detectors are scintillation detectors with a high time but low energy resolution, the latter value is of importance. Because of their large kinetic energy the positrons can easily pass through the sample and are only weakly absorbed by cryostat or furnace walls. This allows complex sample environments to be used.

2.3   Principles of the μSR technique

The emitted positrons are detected and collected in an intensity versus time histogram. The histogram is described by:

$$N_{det}^{e^+}(t) = N_0 \exp(-t/\tau_\mu)[1 + aP(t)\cos(\phi_{det})] + b \tag{2.5}$$

and illustrated by Fig. 2.4 Here the exponential is due to muon decay with a lifetime τ_μ and b represents the time independent background. a is the initial asymmetry. Due to the finite solid angle of the detectors, energy dependent efficiency of detection and possible reduced beam polarization, a is usually $\simeq 0.23$, which is smaller than the theoretical value of 1/3. The spin depolarization function is written as $aP(t)$. Here $P(t)$ reflects the time dependence of the μ^+ polarization. The phase factor ϕ^{det} accounts for the angle between the initial muon polarization and the positron detector. In general two types of experimental geometries are used. So called Zero field (ZF) and Longitudinal field (LF) measurements are performed in a geometry shown in the left half of Fig 2.3. Here two detectors are placed parallel and antiparallel to the initial polarization of the muon beam S_μ. These detectors are usually referred to as forward and backward, respectively. In a
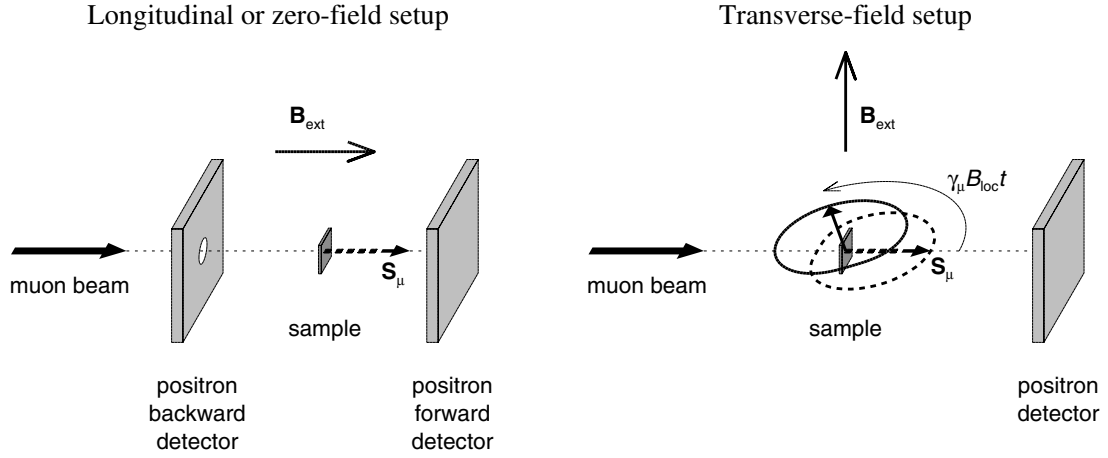
Figure 2.3: *The two types of experimental geometry: the longitudinal and transverse setups are illustrated in the left and right panel respectively. Here the muon spin is drawn parallel to the muon momentum for clarity. The dashed- and solid-line arrows and cardioids in the transverse set-up, represent the Larmor precession of the muon spin in the applied field and the accompanying angular positron distribution. This figure is taken from Ref. [5].*

longitudinal field experiment a magnetic field is applied parallel to S_μ. In the transverse field mode (TF), a magnetic field is applied perpendicular to S_μ, and the positron detectors are placed in a plane perpendicular to this applied field (see right panel Fig. 2.3b).

The muon sources can be divided into two categories: pulsed beams are produced at both ISIS (United Kingdom) and KEK (Japan), while beams at PSI (Switzerland) and TRIUMF (Canada) are (quasi)-continuous. Experiments in this thesis have been done at both ISIS and PSI setups. The different time structure of the beam of these two options, allow both possibilities and limitations for experiments and data analysis. Below these differences will be discussed. It turns out that the muon beams of these two categories are complementary.

2.3.1 Pulsed μ^+ beam

In pulsed beam lines, an ensemble of muons is implanted into the sample at a given time t_0. Two features of the time structure of the beam are of importance here; the pulse width, and the separation between the pulses. Usually the latter is chosen long compared to the muon lifetime. This unique characteristic together with the negligible background between the pulses enables the detection of very small magnetic moments. Here the muon spin precesses around the local magnetic field with a Larmor precession frequency $\omega_\mu = 2\pi\nu_\mu = \gamma_\mu B_{loc}$. Here γ_μ the muon gyromagnetic ratio ($\gamma_\mu = 851.6$ Mrad s^{-1} T^{-1}). Since an angle of 0.5 rad is detectable and a μSR measurement at a pulsed beam can routinely be carried out up to 15 μs, a local field as small as 0.04 mT can be detected. To put this in to perspective, this is in the order of a dipolar contribution due to a nuclear magnetic moment at typical atomic distances and about 10^{-3} times smaller than a similar
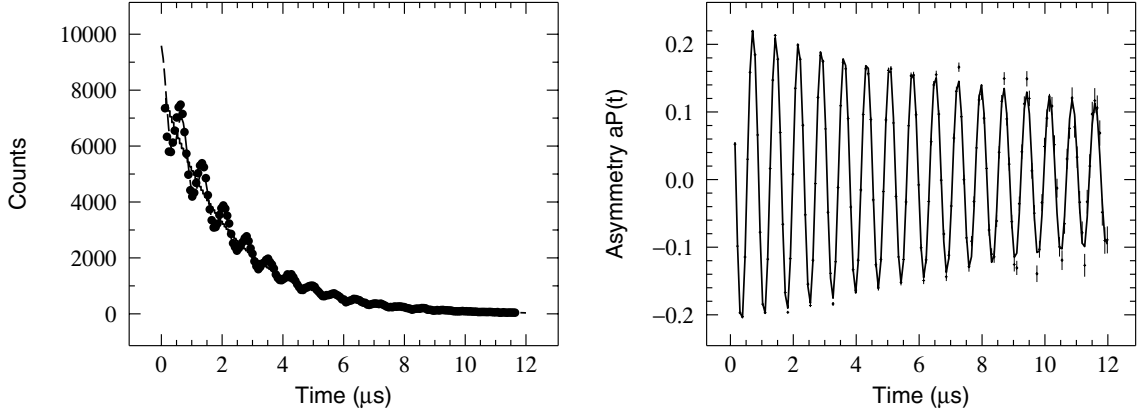
Figure 2.4: *On the left, the positron count rate $N_{det}^{e^+}(t)$ shows a periodic modulation, super imposed on the trivial exponential muon decay. The dotted line represents a fit with Eq. 2.5. For low background experiments, such as with a pulsed beam, one can use Eq. 2.6 for analyses, shown on the right. Due to this procedure the muon decay is leveled out and only the asymmetry $aP(t)$ remains.*

field induced by an electronic moment. Furthermore, the negligible background simplifies the way the spin depolarization function $aP(t)$ can be extracted from the raw data. Since the background in both forward and backward detectors are negligible, *i.e.* b=0 in Eq. 2.5, one can now represent the depolarization function in the following way:

$$aP(t) = \frac{N_F(t) - \alpha N_B(t)}{N_F(t) + \alpha N_B(t)} \tag{2.6}$$

This procedure is illustrated in Fig. 2.4. α is an experimental factor which accounts for the different characteristics of the detectors such as geometry and efficiency. The appropriate α can be calculated from with a transverse field measurement in the same geometry. After correction for α the spectrum should oscillate symmetrically about zero average polarization. A disadvantage of the pulsed beam facilities at ISIS is the relatively large spot size. This is due to the remote collimation, which causes a significant enhancement of the spot size ($\sim$ 3 cm) due to the muons associated with the beam penumbra. On the other hand the finite pulse width of the implanted muon ensemble, limits the time resolution. The pulse width of 70 ns at ISIS, makes it unsuitable for systems exhibiting fast relaxation processes (larger than 5 MHz) or appreciable local field (exceeding 50 mT).

2.3.2   Continuous μ^+ beam

At a continuous muon beamline, every event is treated separately. Each incoming muon will be detected by a thin scintillation detector, and starts a clock. When the implanted muon decays, the emitted positron will be detected and the clock is stopped. A collection of a number of events, typically $\sim 10^7$, will eventually give an intensity versus time histogram. If a second muon enters before decay of the previous muon, data collection is stopped for a few muon lifetimes, in order to prevent mixing. This of course puts special demands on the specifications of the muon rate entering the set up, for optimal operation. The single event method also allows to veto events using logical coincidence electronics. For instance, this can be used when a muon misses the sample and the sample holder,
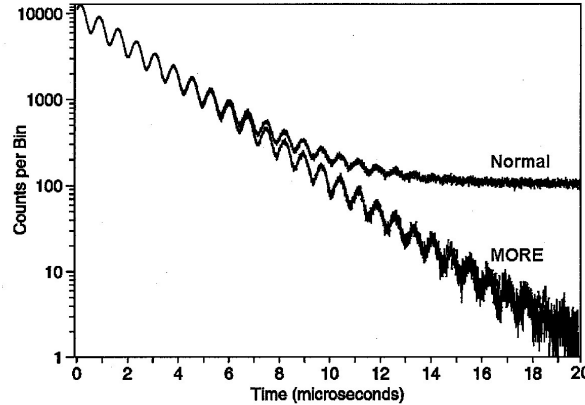
Figure 2.5: *Intensity versus time histogram for silver in a 10 mT transverse field, both in conventional and MORE mode. This figure is taken from Ref. [7], with kind permission from Kluwer Academic Publishers. It clearly shows that the MORE mode enlarges the time window over which oscillations can be observed.*

it will then simultaneously be detected in backward and forward detector and can be rejected. Apart from reducing background, it also allows small samples to be measured, because the spot size in this way is set by the combination of sample and sample holder (0.5 cm is possible). Another advantage of the continuous beam, is the fact that the time of implantation of every single muon is known very accurately, increasing the time resolution of the experiment. In this way Larmor precession frequencies up to ∼400 MHz have been measured. There remains however, relatively high background, which restricts the observation of slow effects. On top of that, it complicates the extraction of the spin depolarization function from the data. Because the level of background is unknown but non-negligible and also detector dependent, Eq. 2.6 can not be used here. Fits to the data are made with Eq. 2.5 where the shape of spin depolarization function and the two extra parameters N_0 and b are included. Here a proper estimate for the initial asymmetry can simplify the analysis.

Recently a new technique has been introduced at the πM3 beam line at PSI, in order to get round some problems linked to continuous beams. The technique is called 'Muons On REquest'(MORE) [7]. The system is based on a kicker which sends in a single muon to the instrument, only when this is required. This reduces background and extends the time accessible to measure (see Fig. 2.5). The reduction of the background allows for an analysis similar to that used for pulsed beams as given by Eq. 2.6. This property is exchanged for detection of fast relaxations, because the MORE device induces an uncertainty in the first 0.2 μs of the spectra.

Bibliography

[1] S.L. Lee, S.H. Kilcoyne and R. Cywinsky, *Muon Science, Muons in Physics, Chemistry and Materials* Institute of Physics, Bristol 1999

[2] E.B. Karlson, *Solid state phenomena, as seen by muon, protons and excited nuclei* Clarendon press, Oxford 1995

[3] A. Schenck, *Muon spin spectroscopy, Principles and applications in solid state physics* Adam Hilger Ltd, Bristol 1985

[4] J. Chappert and R.I. Gryszpan, *Muons and pions in materials research* North-Holland, Amsterdam 1984

[5] P. Dalmas de Réotier and A. Yaouanc, J. Phys.: Condens. Matter **9** (1997) 9113

[6] G.H. Eaton in *Muon Science, Muons in Physics, Chemistry and Materials* edited S.L. Lee, S.H. Kilcoyne and R. Cywinsky, Institute of Physics, Bristol 1999 pp 11-37

[7] R. Abela, A. Amato, C Baines, X. Donath, R. Erne, D.C. George, D Herlach, G. Irminger, I.D. Reid, D. Renker, G. Solt, D. Suhi, M. Werner and U. Zimmermann, Hyperfine Interact. **120-121**,(1999) 575

Chapter 3

Depolarization models

3.1 Introduction

In the previous chapter the basic principles and the way a μSR experiment is run, have been introduced. The spin depolarization function $P(t)$ extracted from the experiment contains the information on the physics of the sample. It can be due to either a static distribution of local fields (dephasing the muon ensemble) or fluctuating fields (relaxation of muon spins). In order to interpret an experimental $P(t)$, some basic cases will be studied here. First, several common magnetic field distributions and their related depolarization functions will be introduced for both zero as well as transverse and longitudinal applied fields. After this, the influence of fluctuating fields will be given. The effect of fluctuating fields will be considered from two different points of view, introducing both motional narrowing and spin lattice relaxation.

3.2   Zero field μSR

In a zero field experiment one measures the time dependence of the polarization of a muon ensemble in the sample under the action of the local field at the muon site. These local fields can either be of electronic origin or be caused by nuclear magnetic moments on neighboring atoms. The different interactions will be considered later in section 3.4. For now, we will just assume a static magnetic field at the muon site. We recall that a magnetic moment will precess around a local field $\mathbf{B}_{loc}$ with a frequency proportional to this field. For the muon this frequency is given by, $\omega = 2\pi\nu_\mu = \gamma_\mu \mathbf{B}_{loc}$, with γ_μ the muon gyromagnetic ratio (γ_μ=851.6 Mrad s^{-1} T^{-1}). The normalized depolarization function is written as P_α(t). The cartesian label α indicates the direction along which the muon polarization S$_\mu$ is measured. Because the applied field B$_{ext}$ is taken along the Z-axis, S$_\mu$ be parallel to the Z or X axis, in the longitudinal or transverse set-ups respectively. In the transverse field set-up, both P_X(t) and P_Y(t) contain the same information, except for a phase shift. Therefore only P_X(t) is considered.
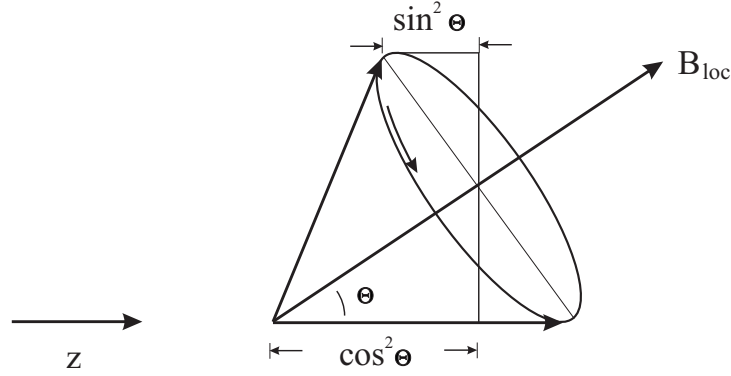
Figure 3.1: *Muon spin precession describing a cone around a local magnetic field $\mathbf{B}_{loc}$. Here θ denotes the angle between the initial muon spin polarisation and the local field.*

$P_\alpha(t)$ reflects the time dependence of S$_\mu$. If all muons spins precess in the same static magnetic field, oriented at an angle θ relative to the initial muon spin direction S$_\mu$(0), the Larmor equation yields:

$$P_\alpha(t) \;\; = \;\; \cos^2(\theta) + \sin^2(\theta)\cos(\omega_\mu t) \tag{3.1}$$

This Larmor precession is illustrated in Figure 3.1. From both figure and equation one can clearly see that P$_Z$(t) describes a cone around the local field. Here only the component of the muon spin perpendicular to the local field oscillates, whereas the parallel component gives a time-independent contribution. This result is one of the fundamentals of the μSR technique. Eq. 3.1 could be observed in a single crystalline magnet, with its easy-axis at an angle of θ. This can be extended to a magnet in polycrystalline form by averaging over all θ. If the sample is not textured this results in:

$$P_Z(t) \;\; = \;\; \frac{1}{3} + \frac{2}{3}\cos(\omega_\mu t) \tag{3.2}$$

Here the first time independent term reflects the fact that on average one third of the field is parallel to the S$_\mu$(0). Clearly the oscillating component reflects the local magnetic

field at the muon site. If the muon spins precess too quickly relative to the resolution of the spectrometer, i.e. in large magnetic fields, the asymmetry of the oscillating part will be averaged to zero. This can typically be observed at a magnetic phase transition. So far, we have assumed only one unique magnetic field at the muon site. This of course is a simplification. Muons can be located at different sites, or even at crystallographically equivalent sites, but with different magnetic environments. This effectively means that the muon ensemble probes a number of magnetic fields. If the number is limited to a few different fields, this will result in a beating of the oscillating signal. However, for larger numbers, a magnetic field distribution, the oscillation will be damped. The time evolution of an ensemble of muon spins probing a field distribution $D(\mathbf{B}_{loc})$ can be computed by solving the Larmor equation in classical mechanics. The depolarization function can simply be written as:

$$P_\alpha(t) \;\; = \;\; \int \hat{\mathbf{S}}_{\mu,\alpha}(t, \mathbf{B}_{loc}) D(\mathbf{B}_{loc}) d\mathbf{B_{loc}} \tag{3.3}$$

Here $\hat{\mathbf{S}}_{\mu,\alpha}$ is defined as the projection along the α-axis of the unit vector parallel to the muon spin S_μ. In the case of a sharp distribution, $D(\mathbf{B}_{loc})$ can be represented as a Dirac δ-function. Then Eq. 3.1 is recovered. Different origins of $\mathbf{B}_{loc}$, give rise to several different magnetic field distributions. One of the most commonly used is the Gaussian field distribution. Since the Gaussian distribution is a very good approximation of a binomial with large multiplicity, this distribution can be expected in the case of randomly oriented nuclear moments. For this case the distribution is isotropic, has a zero average field and can be written as:

$$D(\mathbf{B_{loc}}) = \left(\frac{\gamma_\mu}{\sqrt{2\pi}\Delta}\right)^3 \exp\left[-\frac{(\gamma_\mu B_{loc}^X)^2}{2\Delta^2}\right] \exp\left[-\frac{(\gamma_\mu B_{loc}^Y)^2}{2\Delta^2}\right] \exp\left[-\frac{\gamma_\mu^2(B_{ext}-B_{loc}^Z)^2}{2\Delta^2}\right] \tag{3.4}$$

where $\Delta^2/\gamma_\mu^2 = \langle B_i^2 \rangle$ is the second moment of the field distribution along one of the cartesian axes. B_{ext} introduces the external applied field in a longitudinal set up experiment. The zero field depolarization function for this case, can be obtained by averaging Eq. 3.1 over $D(\mathbf{B_{loc}})$. This yields:

$$P_Z^G(t) = \frac{1}{3} + \frac{2}{3}(1 - \Delta^2 t^2)\exp\left(-\frac{1}{2}\Delta^2 t^2\right) \tag{3.5}$$

which is well known as the Kubo-Toyabe function [1] and is illustrated in Figure 3.2. $P_Z(t)$ exhibits a strongly damped oscillation with a minimum at t=$\sqrt{3}/\Delta$. For small Δt, $P_Z(t)$ can be approximated by a parabolic form $P_Z(t) = 1 - \Delta^2 t^2$. It saturates to a value of 1/3 for sufficiently large Δt, for the same reason as in Eq. 3.2. Application of a relatively large longitudinal field in this static case, causes the resultant field at the muon site (*i.e.* $\mathbf{B}_{loc} + B_{ext}$) to effectively align along the Z-axis. This will effectively reduce the depolarization rate. With an averaging similar to the one for zero-field, the LF depolarization function with Gaussian distribution becomes [2]:

$$\begin{aligned} P_Z^G(t, B_{ext}) \;\; = \;\; & 1 - \frac{2\Delta^2}{\gamma_\mu^2 B_{ext}^2}\left[1 - e^{-\frac{1}{2}\Delta^2 t^2}\cos(\gamma_\mu B_{ext}t)\right] \\ & + \frac{2\Delta^3}{\gamma_\mu^3 B_{ext}^3}\int_0^{\Delta t} e^{-\frac{1}{2}y^2}\cos\left(\frac{\gamma_\mu B_{ext}}{\Delta}y\right) dy \end{aligned} \tag{3.6}$$
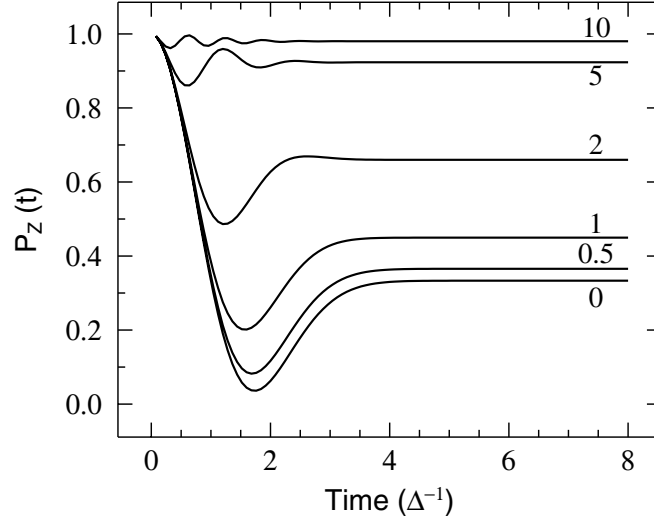
Figure 3.2: *The magnetic field dependence of the longitudinal depolarization function derived for a static isotropic Gaussian field distribution. The values of the magnetic field are given in units of Δ/γ_μ*

Here the second and third terms become vanishingly small for $\Delta/\gamma_\mu B_{ext} \to 0$. Figure 3.2 illustrates the field dependence of $P_z^G(t)$ for several values of B_{ext} given in units of Δ/γ_μ. It clearly shows that the depolarization is almost canceled for $B_{ext} \gg B_{loc}$. In addition to the Gaussian distribution there are several other possible distributions. The Lorentzian distribution is often used in dilute spin glass systems. The transverse geometry is mainly used to investigate microscopic field distributions, distinguish different kinds of muon adducts and to measure the local susceptibility. The latter experiment yields both information on the symmetry and the hyperfine coupling at the muon site. If B_{ext} is taken sufficiently large compared to Δ/γ_μ, $P_X(t)$ will only probe the distribution along B_{ext}. This results in a dephasing of the muon spins, which with Eq. 3.3 gives:

$$P_X(t) = \exp\left(-\frac{\Delta^2 t^2}{2}\right)\cos(\omega_\mu t) \tag{3.7}$$

Similar to the $P_Z(t)$, if Δt is small, the envelope of $P_X(t)$ can be approximated with the parabolic form $(1 - \Delta^2 t^2/2)$. Here however, the initial depolarization is reduced by half, since only the one component of the distribution along B_{ext} participates in the depolarization. As mentioned earlier, the depolarization in the transverse set-up as is due to the dephasing of the muon spins by the local field distribution along B_{ext}. The characteristic damping rate of the oscillations is related to the typical time T_2. If the phase differences $\Delta\theta$ exceed a few radians, the detector will no longer be able to pick up a precessing signal. The spin system will be out of phase by 1 rad when:

$$\Delta\theta = \Delta\omega T_2 = 1 \Rightarrow \frac{1}{T_2} = \Delta\omega \tag{3.8}$$

where $\Delta\omega = \gamma_\mu\sqrt{\langle B_Z^2 \rangle}$. T_2 is commonly used in NMR and is referred to as spin-spin relaxation. It discerns itself from another form of relaxation, known as spin-lattice relaxation

(T_1), by the fact that it is a pure dephasing process and as such does not require energy exchange with the system. We will have a closer look at spin-lattice relaxation in the next section, where the influence of fluctuating fields will be described.

3.3 Dynamic depolarization/relaxation functions

In the previous paragraph the magnetic fields at the muon site were assumed to be static compared to the halflife of the muon governing the μSR experiment. In fact, the magnetic fields at the muon site often do fluctuate on time scales measurable by μSR. The origin of this can be several. It can be due to the time fluctuations of the muon environment *e.g.* due to spin waves, or slowing down of paramagnetic fluctuations near a magnetic transition temperature. But it can also be due to motion of the muon itself, *e.g.* muon diffusion. Both phenomena can be treated in the same way. Here, we will discuss the influence of a fluctuating magnetic field on T_2. A qualitative estimate can be made by the assumption that the component of the local field is perpendicular to the initial muon spin at the muon site and alternates between two defined values $\pm B_{loc}$. After a correlation time τ_c the direction of the field is chosen randomly from the two opposite directions with an equal probability. If $\Delta\omega\tau_c \ll 1$, the summed angle will be the result of a 'random walk'. The mean square dephasing angle for such a process is:

$$\langle\theta^2\rangle = n\Delta\omega^2\tau_c^2 \tag{3.9}$$

Here n is the number of steps that take place in a time $T_2 = n\tau_c$. Being out of phase by 1 rad now requires that:

$$\langle\theta^2\rangle = \Delta\omega^2\tau_c T_2 = 1 \Rightarrow \frac{1}{T_2} = \Delta\omega^2\tau_c \tag{3.10}$$

Note that for shorter τ_c (*i.e.* the more rapid the motion), the depolarization rate decreases. In other words, if during its lifetime the muon has the opportunity to probe a large number of fields forming a field distribution, it will average over all of them, and reduce the total dephasing of the whole muon ensemble.

3.3.1 The strong collision approximation

A complete mathematical description is obtained by the strong collision approximation. It is assumed that the local field changes orientation and magnitude with a single fluctuation rate, and a probability distribution of $\rho(t) \propto \exp(-\nu t)$. After collision, the field is randomly chosen from a probability distribution $P(B_{loc})$, without any correlation to the field before the collision. This process is also know as a Markov process. For the distribution we will assume a Gaussian distribution $P^G(B_{loc})$ in zero field. Before the first collision the polarisation should follow the static Kubo-toyabe function. After the first collision the ensemble will now decay, following a Kubo-Toyabe function but with the initial time zero taken at the time of collision. This process can be written down for multiple collisions and leads to:

$$
\begin{aligned}
P_Z^G(t) &= e^{-\nu t}[p_Z(t) + \nu \int_0^t p_Z(t_1)p_Z(t-t_1)dt_1 \\
&\quad +\nu^2 \int_0^t \int_0^{t_2} p_Z(t_1)p_Z(t_2-t_1)p_Z(t-t_2)dt_1 dt_2 + ...]
\end{aligned} \tag{3.11}
$$
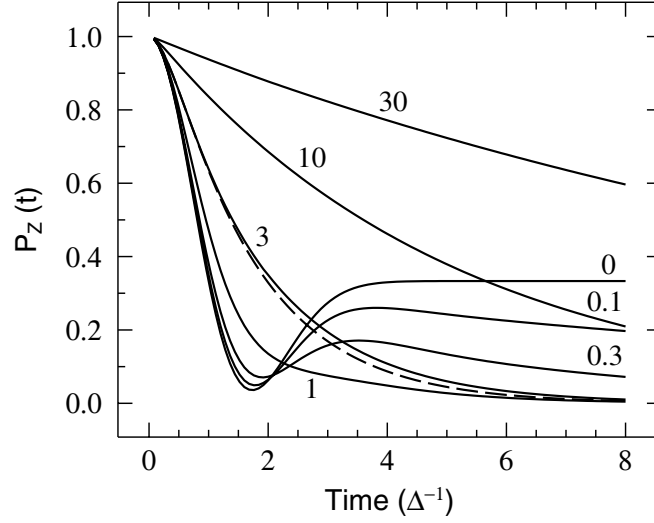
Figure 3.3: *The fluctuation rate dependence of the zero-field depolarization function derived for an isotropic Gaussian field distribution and a Markov dynamical process. The values of the fluctuation rate are given in units of Δ.*

In this equation $\nu p_Z(t_i) \exp(-\nu t)$ represents the product of the static Kubo-Toyabe with the probability of collision within a time interval dt. The expression in general can not be expressed analytically and needs to be solved numerically. Figure 3.3 shows numerically calculated depolarization functions for several fluctuation rates ν, where ν is given in units of Δ. For an increasing fluctuation rate, one observes a collapse of the tail, followed by a reduced depolarization at short times. If ν/Δ is sufficiently large, an analytical approximation of $P_Z(t)$ can be made via a Laplace transform [3]. This results in the formula:

$$P_Z(t) = \exp\left\{-\frac{2\Delta^2}{\nu^2}[\exp(-\nu t) - 1 + \nu t]\right\} \tag{3.12}$$

This approximation is compared with the numerical solution in Fig 3.3 for ν/Δ=3. In the motional narrowing limit, $P_Z(t)$ simplifies to an exponential function:

$$P_Z(t) = \exp(-\lambda_Z t) \qquad\qquad \lambda_Z = 2\Delta^2/\nu \tag{3.13}$$

For a transverse set-up an analytical approximation can be made in a similar way:

$$P_X(t) = \exp\left\{-\frac{\Delta^2}{\nu^2}[\exp(-\nu t) - 1 + \nu t]\right\}\cos(\omega_\mu t) \tag{3.14}$$

This formula is commonly referred to as "Abragam formula", although it was first derived by Anderson (1954) as a model for the NMR Line shape [4]. It gives results very close to the strong collision approximation and interpolates between the static and motional narrowing limits. For the latter the envelope will give an exponential function

$$P_X(t) = \exp(-\lambda_X t)\cos(\omega_\mu t) \qquad\qquad \lambda_X = \Delta^2/\nu \tag{3.15}$$

3.3.2 Relaxation

Up to now we have only considered the depolarization due to the Larmor precession around a series of temporal local fields, given by a specific field distribution. There is, however, another process which can depolarize the muon ensemble. This process usually involves an exchange of the muon Zeeman energy in a magnetic field, with a dynamical process in the spin-lattice system. In this process the muon spin will be flipped. We will refer to this as the previously mentioned spin-lattice relaxation, T_1. For a proper description, we must use quantum mechanics. Here, the muon energy is quantized into two energy levels split by the magnetic field. The occupancies of these levels in thermal equilibrium, are related by the Boltzmann factor. However, since the muon beam is fully polarized, only one level is occupied at implantation. Therefore, it is expected that the spin-lattice relaxation decreases the initial polarization towards an equilibrium. A simple approach describes the rate equations of the occupancies of the two levels by the formulea:

$$\frac{dn_+}{dt} = -W_\downarrow n_+ + W_\uparrow n_-$$
$$\frac{dn_-}{dt} = W_\downarrow n_+ - W_\uparrow n_- \tag{3.16}$$

where n_+ and n_- are the occupancies of the spin-up and spin-down levels, respectively. $W_\uparrow$ and $W_\downarrow$ represent the transition probabilities between the two spin states going from n_- to n_+ and *vice versa*. At common temperatures the thermal equilibrium occupancies of both levels can be considered equal and $W_\uparrow \simeq W_\downarrow$. The polarization can be written as $P = (n_+ - n_-)/(n_+ + n_-)$, giving a simple exponential decay as a solution:

$$P_Z(t) \propto e^{(W_\uparrow + W_\downarrow)t} \simeq e^{-2Wt} = e^{-\lambda_z t} = e^{-t/T_1} \tag{3.17}$$

Various notations are given here: the most commonly used in μSR is the relaxation rate λ, which is simply the inverse of the relaxation time T_1. For spin-lattice relaxation a time-dependent perturbation of the local magnetic field is needed. For a simple two level system this fluctuation needs to be transverse to the main static average longitudinal field. Furthermore, it must be able to supply an energy quantum equal to the muon Zeeman splitting, in order to flip the muon spin. This implies that the fluctuation must have a significant intensity at the Larmor frequency:

$$\omega_\mu = \Delta E/\hbar = \gamma_\mu B_{loc} \tag{3.18}$$

This corresponds to 0.57 μeV per Tesla. One way to formulate the time-dependent perturbation starts from the density matrix theory [5], in order to calculate the transition rate W. It is closely related to Fermi's Golden rule and shows that the transition rate is proportional to the spectral density function $J(\omega)$ taken at the Larmor frequency ($W \propto J(\omega_\mu)$). If the fluctuations of the local fields are modeled with a simple exponential decay of the auto-correlation function:

$$\frac{\langle B_{loc}(0)B_{loc}(t)\rangle}{\langle B_{loc}(0)^2\rangle} = \exp(-\nu t) \tag{3.19}$$

the spectral density function can be obtained by Fourier transformation. This results in a relaxation rate $\lambda_Z = 1/T_1 \propto \nu/(\omega_\mu^2 + \nu^2)$. Combining this with the case of ZF, *i.e.* $\omega_\mu = 0$, as was given in Eq. 3.13 the relaxation function is obtained:

$$P_Z(t, \nu, \omega_\mu) = \exp[-(2\Delta^2\nu t)/(\omega_\mu^2 + \nu^2)] \tag{3.20}$$

This is commonly known as the BPP expression, after its original formulators, Bloembergen, Purcell and Pound. It is valid only for the narrowing limit $\nu/\Delta \gg 1$, where the depolarization is dominated by spin-lattice relaxation. The Larmor frequency in common applied magnetic fields is of the order of ten to hundred MHz and is usually negligible compared to the typical fluctuation rates in solids ranging from $\nu = 10^7$-10^3 MHz. Therefore, in most cases, dynamic $1/T_1$ relaxation will show only little dependence on longitudinal fields. Application of a longitudinal field provides a way to distinguish between dynamic and static situations. A good example is the use of a small magnetic field of typically 10 mT, to take out any depolarization due to the nuclear moments, which on a muon time scale appear to be static.

3.4 The magnetic field at the muon site

So far we have not considered the origin of the local field at the muon site. Here the most important interactions will be introduced in the case of an interstitial muon, as observed *e.g.* in metals. After thermalization the muon will usually come to rest in one location, or distributed over several interstitial sites in the crystal. The local magnetic field can in general be given by a sum of four terms:

$$\mathbf{B}_{loc} = \mathbf{B}_{ext} + \mathbf{B}_{dip} + \mathbf{B}_{con} \tag{3.21}$$

Here $\mathbf{B}_{ext}$ accounts for the magnetic field which is applied externally on the system. $\mathbf{B}_{dip}$ reflects the interaction with the localized lattice spins through the dipolar interaction. In contrast to *e.g.* NMR, the dipolar field will be the dominant contribution, since the muon does not have any bound electrons. The localized moments can be both of nuclear or electronic origin, and their contributions to the local field are described by:

$$B_i^{dip} = \frac{\mu_0}{4\pi}\gamma_k \hbar \sum_k \frac{1}{r^3}\left(\frac{3x_{i,k}x_{j,k}}{r^2} - \delta_{ij}\right)I_{i,k} \tag{3.22}$$

Where μ_0 is the permeability of vacuum and the indices i,j refer to x,y,z. The dipolar field $\mathbf{B}_{dip}$ at site r_μ is determined from the sum over all k moments $I_{i,k}$ at positions $r_i = x_{i,k} - x_{i,\mu}$, and $r = |\mathbf{r}|$. δ_{ij} represents Kronecker's symbol and γ_k indicates the gyromagnetic ratio of the nuclear or electron spin at r_k. For rare earth ions it is common to use the Landé factor g_{J_i} instead. These are related via $g_{J_i} = -\gamma_i \hbar/\mu_B$, where μ_B is the Bohr magneton. It must be noted that the dipolar field at the muon site due to either nuclear or electronic moments differ typically by three orders of magnitude. For example, a nuclear moment with $\gamma_k = 100$ Mrad s^{-1}T^{-1} at a distance of 1.5 Å from the muon gives a contribution of 0.31 mT. A rare earth metal on the other hand with a Landé factor of 2 (Gd^{+3}) at the same distance gives 0.56 T.

Although the contribution of a spin at a distance r drops with r^{-3}, the number of spins at this distance will increase with r^2. In order to calculate Eq. 3.22 properly, the sample volume it is usually decomposed into two sections, with a part inside and part outside of a "Lorentz sphere". Now, one can write the dipolar field as:

$$\mathbf{B}_{dip} = \mathbf{B}_{dip'} + \mathbf{B}_{Lor} + \mathbf{B}_{dem} \tag{3.23}$$

with $\mathbf{B}_{dip'}$ is given by a lattice sum similar to Eq. 3.22, but restricted to the Lorentz sphere with a radius r_{Lor}. If r_{Lor} is chosen large enough, the outer part can be approximated

with an integral. The result of this integral yields the Lorentz field $\mathbf{B}_{Lor} = 1/3\mu_0\mathbf{M}_{sat}$ and the demagnetisation field $\mathbf{B}_{dem} = -\mu_0\mathrm{N}\mathbf{M}_{bulk}$. $\mathbf{M}_{sat}$ and $\mathbf{M}_{bulk}$ are the saturation and bulk magnetization, respectively, and N is the demagnetization tensor which is related to the shape of the sample. For a sphere, $\mathbf{B}_{dem} = -\mu_0\mathbf{M}_{bulk}/3$. At fields strong enough $\mathbf{M}_{bulk} = \mathbf{M}_{sat}$ and $\mathbf{B}_{Lor} + \mathbf{B}_{dem}$ cancels out.

Returning to the other terms contributing to the local field B_{loc} in Eq. 3.21. $\mathbf{B}_{con}$ is the contact hyperfine field, due to the Fermi contact interaction. It results from spin density at the muon site. In metals $\mathbf{B}_{con}$ is induced by polarized conduction electrons and thus proportional to the Pauli susceptibility χ_{Pauli}. $\mathbf{B}_{con}$ is assumed to be isotropic and follows the magnetization.

3.5 Theory for muonated radicals

3.5.1 Introduction: MuSR on muonium and muonated radicals

Until now we have considered the muon as located in an unbound state at an interstitial site in the sample. This is common in metallic materials. However in a variety of materials, such as organic compounds, insulators and semi-conductors, the muon can form a neutral bound state with an electron, known as muonium (Mu). This muonium can be viewed as a light hydrogen atom. Muonium will interact with its surroundings and can even add to *e.g.* unsaturated bonds in organic materials, forming muonated radicals. Both interstitial muonium and muonated radicals open a whole new range of applications often referred to as MuSR. In this section some of the basic concepts will be introduced on the basis of free muonium.

3.5.2 The Breit-Rabi diagram

The Hamiltonian of free muonium is similar to atomic hydrogen. It consists of two terms. The first couples the electron (S) and muon spin (I^μ) by an interaction variously known as the Fermi or contact interaction. An applied magnetic field B introduces Zeeman splitting, resulting in a Hamiltonian in frequency units:

$$\frac{\hat{\mathcal{H}}_0}{\hbar} = A_\mu \hat{S} \cdot \hat{I}^\mu + \gamma_e B \hat{S}_z - \gamma_\mu B \hat{I}_z^\mu \tag{3.24}$$

where $\gamma_e \gg \gamma_\mu$ are the electron and muon gyromagnetic ratios, and A_μ the hyperfine coupling constant. The generated energy level scheme is shown in Fig 3.4a. This is known as the $Breit - Rabi$ diagram, which was originally conceived for atomic hydrogen. Expressions for the four energy levels and their corresponding eigenvectors are given in Table 3.1. At high field the eigenstates are pure Zeeman states represented by $|\chi\rangle = |m^s, m^\mu\rangle$. At zero field the four levels form a singlet and a triplet state. The energy splitting between these two states equals A_μ. Intermediate field eigenvectors can be written as the sum of Zeeman states, *i.e.*: $|\psi\rangle = \sum_i c_i |\chi_i\rangle$. Here the coefficients c_{im} depend on both A_μ and the magnetic field B, and are often indicated as sin and cos, see Table 3.1.

When a muonium atom (Mu) is formed, the muon spin I_μ interacts strongly with the spin S of the electron. Here the temporal development of the muon spin needs to be

Table 3.1: *Zero-order eigenvectors and energies of muonium with isotropic hyperfine interaction $\hat{\mathcal{H}}_0$. Eigenvectors are given in the basis $|m_e, m_\mu\rangle$.*

$$\hat{\mathcal{H}}_0/\hbar = \gamma_e B \hat{S}_z - \gamma_\mu B \hat{I}_z^\mu + A_\mu \hat{S} \cdot \hat{I}^\mu$$

$$E_1 = \tfrac{1}{4}A_\mu + \tfrac{1}{2}(\nu_e - \nu_\mu)$$
$$E_2 = -\tfrac{1}{4}A_\mu + \tfrac{1}{2}[A_\mu^2 + (\nu_e + \nu_\mu)^2]^{\frac{1}{2}}$$
$$E_3 = \tfrac{1}{4}A_\mu - \tfrac{1}{2}(\nu_e - \nu_\mu)$$
$$E_4 = -\tfrac{1}{4}A_\mu - \tfrac{1}{2}[A_\mu^2 + (\nu_e + \nu_\mu)^2]^{\frac{1}{2}}$$

$$|1\rangle = |\tfrac{1}{2}, \tfrac{1}{2}\rangle$$
$$|2\rangle = \cos(\alpha)|\tfrac{1}{2}, -\tfrac{1}{2}\rangle + \sin(\alpha)| -\tfrac{1}{2}, \tfrac{1}{2}\rangle$$
$$|3\rangle = | -\tfrac{1}{2}, -\tfrac{1}{2}\rangle$$
$$|4\rangle = \sin(\alpha)|\tfrac{1}{2}, -\tfrac{1}{2}\rangle + \cos(\alpha)| -\tfrac{1}{2}, \tfrac{1}{2}\rangle$$

$$\cos(\alpha) = 1/\sqrt{2}\{1 + (\nu_e + \nu_\mu)/[A_\mu^2 + (\nu_e + \nu_\mu)^2]^{\frac{1}{2}}\}^{\frac{1}{2}}$$
$$\sin(\alpha) = 1/\sqrt{2}\{1 - (\nu_e + \nu_\mu)/[A_\mu^2 + (\nu_e + \nu_\mu)^2]^{\frac{1}{2}}\}^{\frac{1}{2}}$$

described with a quantum mechanical model. Here the muon polarization will be based on a spin density matrix approach [5]. The basis for the density operators must span the spin spaces of both the muon and the electron. Because the muon and electron spins mutually influence each other, the density matrix contains mixed elements as well. The time evolution of the longitudinal muon polarization is given by:

$$P_Z(B,t) = N^{-1} \sum_m \left(\left| \sum_i 2m_i^\mu c_{im}^* c_{im} \right|^2 + 2 \sum_{n<m} \left| \sum_i 2m_i^\mu c_{im}^* c_{in} \right|^2 \cos(\omega_{nm}t) \right) \quad (3.25)$$

Here N=4 is the dimension of the energy matrix and $\omega_{nm} = (E_n - E_m)/\hbar$ is the separation of the two mixing levels. For muonium with an isotropic hyperfine interaction, this results in:

$$P_Z(B,t) = \frac{1}{2}\left[1 + \frac{x^2}{1+x^2} + \frac{1}{1+x^2}\cos(\omega_{24}t) \right] \quad (3.26)$$

where $x = B/B_0$ and $B_0 = A_\mu/(\gamma_e + \gamma_\mu)$. From this formula one can see that the time independent part of the polarization increases with increasing field. The field related to $x = 1$ is referred to as repolarizing field, because at this field repolarization is half way. For free muonium this will happen at $B = B_0 \approx 150$ mT, but muonuated radicals this can be an order of magnitude lower, due to the reduced hyperfine interaction A_μ. Because for most spectrometers the time resolution is too low to observe the frequencies related to the energy splitting ω_{ij}, only the time-averaged part $\overline{P}_Z(B)$ is observed:

$$\overline{P}_Z(B) = \frac{1}{2}\left[1 + \frac{x^2}{1+x^2} \right] \quad (3.27)$$

This is variously known as a decoupling, quenching or repolarization curve and is illustrated with a dotted line in Fig. 3.4.
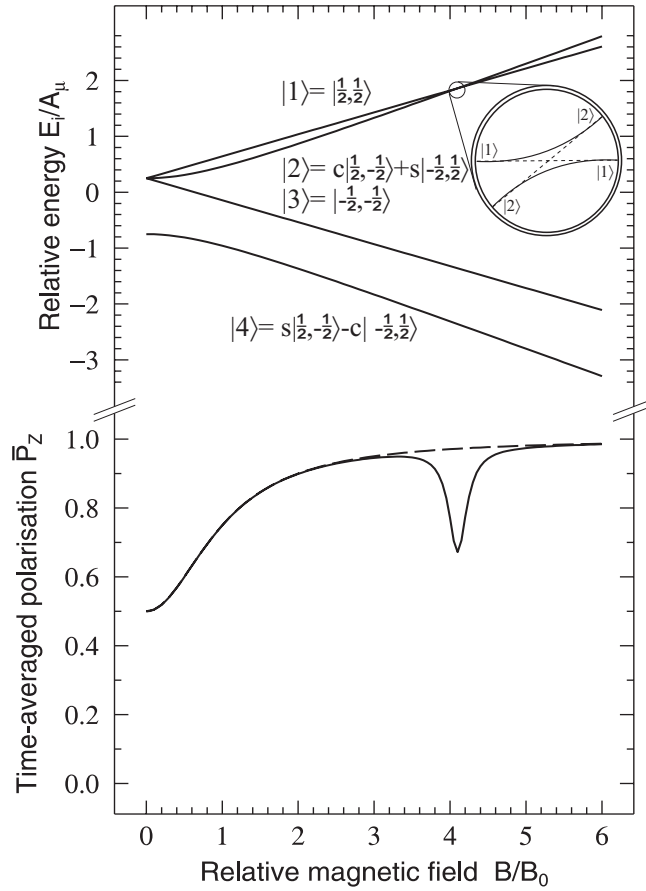
Figure 3.4: *Energy levels and time-averaged polarisation versus magnetic field. The Breit-Rabi diagram (top) is borrowed from atomic hydrogen, but applies also to muonium and muonium substituted molecular radicals when the time-average muon-electron hyperfine coupling is isotropic (Eq. 3.24). The crossing of energy level 1 and 2 occurs at a magnetic field $B = (\gamma_e^2 - \gamma_\mu^2)B_0/(2\gamma_e\gamma_\mu) \approx \frac{A_\mu}{2\gamma_\mu}$, which is accessible for radical states. At the crossing static dipolar perturbations dominate and mix the eigenvectors of both levels. This results in an avoided level crossing (ALC), see insert. The dotted lines represent the unperturbed situation. With increasing field the muon spin is decoupled from the hyperfine interaction, resulting in an increasing time-averaged polarisation $\overline{P}_Z(B)$. At an ALC, $\overline{P}_Z(B)$ is reduced due to mixing of states. The Figure is sketched using an unphysically large value for γ_μ/γ_e (here 0.12) in order to display the level crossing.*

In general the interaction will be more complex, due to the symmetry of site, or the dipolar contribution induced in the electron-muon hyperfine coupling. Analytical solutions are know for a few limited cases of field and orientation of the field with respect to the principle axis, for example for zero field or field applied along a principle axis [6]. For a general orientation and for orientationally averaged case, such as powder samples, repolarization has to be computed numerically. For a hyperfine coupling with axial symmetry, only one characteristic field B_1 is needed to represent the anisotropy. Pratt showed that the computed repolarization can well be represented with [7]:

$$\overline{P}_Z(B) = \frac{q + x^2}{1 + x^2} \quad with \quad q = \frac{1}{2}\frac{\langle\cos^2\phi\rangle + y^2}{1 + y^2}, \quad x = \frac{B}{B_0}, \quad y = \frac{B}{B_1} \qquad (3.28)$$
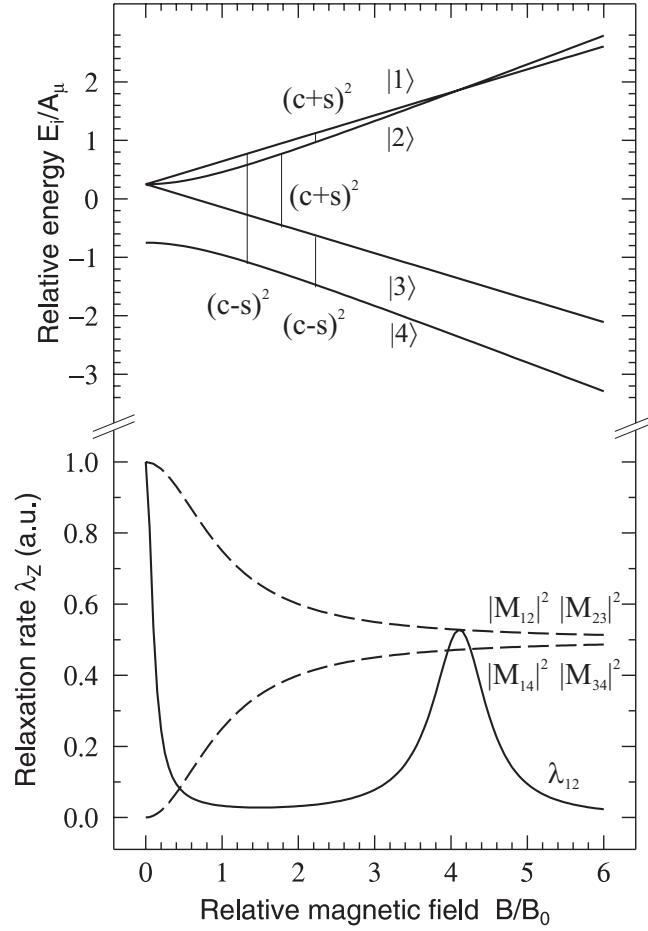
Figure 3.5: *Energy level diagram for an isotropic hyperfine interaction $A_\mu \hat{S} \cdot \hat{I}_\mu$. The interconnecting lines represent transitions induced by fluctuation of an anisotropic dipolar perturbation (top). The lower graph shows the transition probabilities for several transitions (dotted line) and the relaxation rate for the 1-2 transition λ_{12} (solid line). At the crossing the spectral distribution function ($J(\omega_{12})$ see Eq. 3.33) maximizes, resulting in a peak in the relaxation rate λ_{12}. This is also observed for the crossing at $B/B_0=0$.*

ϕ represents the angle between the field and the principal axis of the hyperfine interaction. In the polycrystalline case $\langle \cos^2 \phi \rangle = \frac{1}{3}$. For an isotropic interaction $B_1 \approx 0$, q approaches $\frac{1}{2}$ and Eq. 3.27 is retrieved. For relatively low anisotropies the repolarization is a two-stage process, but for large anisotropy the two stages merge into a broad repolarization. Additionally the introduced anisotropy lowers the polarization to $\frac{1}{6}$th of the full asymmetry at low fields, in stead of $\frac{1}{2}$ for the isotropic case. The repolarization curves can be an alternative for studying anisotropic muonium in non-single-crystal samples, where the orientation dependence of transverse-field μSR frequencies result in broad, weak and often undetectable lines.

3.5.3   Avoided Level Crossing

As was mentioned above, the electron-muon hyperfine interaction can become anisotropic, due to the surroundings of the muonium. In organic materials, for example, muonium can often react with the host molecules to create open-shell species or radicals. Electronic spin

Table 3.2: *The static anisotropic perturbation $\hat{\mathcal{H}}_1$. $\hat{\mathcal{H}}_1$ is subdivided in components based on the effective change of spin ΔM. The energies and eigenvectors are obtained from the submatrix, which describes the Hamiltonian close to the level crossing. Eigenvectors are given in the basis $|m_e, m_\mu\rangle$.*

$$\hat{\mathcal{H}}_1 = -D_\perp^\mu \left[A + B + C + D + E + F \right]$$

$$D_\perp^\mu = -\tfrac{1}{2} D_\parallel^\mu = \gamma_e \gamma_\mu h / 4\pi^2 r^3$$
$$A = (1 - 3\cos^2\theta) \, \hat{S}_z \hat{I}_z^\mu$$
$$B = -\tfrac{1}{4}(1 - 3\cos^2\theta) \left[\hat{S}_+ \hat{I}_-^\mu + \hat{S}_- \hat{I}_+^\mu \right] \qquad\qquad \Delta M = 0$$
$$C = -\tfrac{3}{2} \left(\sin\theta \cos\theta e^{-i\phi} \right) \left[\hat{S}_z \hat{I}_+^\mu + \hat{S}_+ \hat{I}_z^\mu \right] \qquad\qquad \Delta M = 1$$
$$D = -\tfrac{3}{2} \left(\sin\theta \cos\theta e^{+i\phi} \right) \left[\hat{S}_z \hat{I}_-^\mu + \hat{S}_- \hat{I}_z^\mu \right] \qquad\qquad \Delta M = 1$$
$$E = -\tfrac{3}{4} \left(\sin^2\theta e^{-2i\phi} \right) \left[\hat{S}_+ \hat{I}_+ \right] \qquad\qquad\qquad \Delta M = 2$$
$$F = -\tfrac{3}{4} \left(\sin^2\theta e^{+2i\phi} \right) \left[\hat{S}_- \hat{I}_- \right] \qquad\qquad\qquad \Delta M = 2$$

$$\left| \begin{array}{cc} \tfrac{1}{2}(\nu_e - \nu_\mu) - \tfrac{1}{2}\nu_0 - E & \tfrac{1}{2}q e^{-i\phi} \\ \tfrac{1}{2}q e^{+i\phi} & \tfrac{1}{2}(\nu_e + \nu_\mu) - \tfrac{1}{2}\nu_0 - E \end{array} \right|$$

$$\nu_0 = \tfrac{1}{2} \left(A^\mu - D_\perp^\mu (1 - 3\cos^2\theta) \right)$$
$$q = \tfrac{3}{2} D_\perp^\mu \sin\theta \cos\theta$$

$$E_1 = \tfrac{1}{2}\nu_e + \tfrac{1}{2}\sqrt{(\nu_\mu - \nu_0)^2 + q^2}$$
$$E_2 = \tfrac{1}{2}\nu_e - \tfrac{1}{2}\sqrt{(\nu_\mu - \nu_0)^2 + q^2}$$

$$|1\rangle = \cos(\beta) |\tfrac{1}{2}, \tfrac{1}{2}\rangle + \sin(\beta) |\tfrac{1}{2}, -\tfrac{1}{2}\rangle$$
$$|2\rangle = \sin(\beta) |\tfrac{1}{2}, \tfrac{1}{2}\rangle - \cos(\beta) |\tfrac{1}{2}, -\tfrac{1}{2}\rangle$$

$$\cos(\beta) = 1/\sqrt{2} \{ 1 + (\nu_\mu - \nu_0) / [(\nu_\mu - \nu_0)^2 + q^2]^{\frac{1}{2}} \}^{\frac{1}{2}}$$
$$\sin(\beta) = 1/\sqrt{2} \{ 1 - (\nu_\mu - \nu_0) / [(\nu_\mu - \nu_0)^2 + q^2]^{\frac{1}{2}} \}^{\frac{1}{2}}$$

density is then distributed throughout the molecule, resulting in an anisotropic (dipolar) component of the hyperfine interaction in addition to the isotropic (contact) term. If this dipolar interaction is written out in spin operators, additional off-diagonal terms will appear in the Hamiltonian. The magnitude, in frequency units, is about $\gamma_e \gamma_\mu h / 4\pi^2 r^3$, typically 10% of the isotropic contact interaction A_μ.

It is often useful to split the exact Hamiltonian of a system into the sum of a main contribution $\hat{H}_0$ and a small perturbation $\hat{H}_1$ as $\hat{H} = \hat{H}_0 + \hat{H}_1$. The effect of $\hat{H}_1$ leads to corrections to the zero order energies En^0 which are given up to second order by:

$$E_n - En^0 = \langle \chi_n | \hat{H}_1 | \chi_n \rangle + \sum_{m \neq n} \frac{|\langle \chi_n | \hat{H}_1 | \chi_m \rangle|^2}{E_n^0 - E_m^0} \qquad (3.29)$$

This correction is generally very small. However, if the zero-order energy levels cross, which is true for E_1 and E_2 in Fig. 3.4, the expression for second order perturbation diverges provided the numerator is non zero. Close to the crossing the dipolar term can now be considered the main contribution, and off-diagonal isotropic hyperfine interaction terms can be neglected. Table 3.2 gives the dipolar interaction in the case of axial symmetry written out in electron and muon spin operators. Three types of resonances are characterized by the selection rules $\Delta M = \Delta(m_e + m_\mu)$, depending on whether both or only a single spin flips and whether the spin flips are in the same direction [8]. One important aspect to note is that all contributing terms in the dipolar interaction depend on the angle θ between the symmetry axis and the field. This orientation dependence is transferred to both the energy levels and the eigenstates. From the expressions for the energy levels in Table 3.2, one can see that the levels do not actually cross but repel each other. This behaviour is referred to as avoided level crossing (ALC) (others call it level crossing or anticrossing). The resonance field is given by:

$$B_r(\Delta_1) = \nu_0 = \left(A_\mu - D_\perp^\mu(1 - 3\cos^2\theta)\right)\left[\frac{1}{2\gamma_\mu}\right] \tag{3.30}$$

and the corresponding gap frequency on resonance is

$$\omega_{12}(B_r, \Delta_1) = q = \frac{3}{2}D_\perp^\mu \sin\theta\cos\theta \tag{3.31}$$

With $D_\perp^\mu$ in the order of ten MHz, the oscillating term in Eq. 3.25 is within the time resolution of continuous beam spectrometers. For ALC-μSR, however, usually a time integrated set up is used, because usually one is only interested in peak position and shape, as will be discussed in the next section.

3.5.4   ALC-μSR line shapes

In an actual ALC-experiment, resonances are observed as changes in decay positron count rates in detectors placed in 'forward' and 'backward' directions relative to the initial spin polarization of the muon. In a time integrated set up, time information is exchanged in favor of an increased muon flux and hence improved counting statistics. This effectively averages the oscillating terms in Eq. 3.25 reducing them to zero. Nevertheless, a static contribution mixing the avoiding levels remain, which for the above dipolar interaction gives:

$$\overline{P}_Z(B, \theta) = 1 - \frac{1}{2}\frac{q^2}{q^2 + (\nu_\mu - \nu_0)^2} \tag{3.32}$$

This represents a polarization dip with a Lorentzian shape centered at the avoided level crossing and is illustrated in Fig. 3.4 with the solid line. Note that both the peak position ν_0 and the width q depend on the orientation of the system in the field. A powder pattern which is obtained by averaging over θ, gives a very characteristic asymmetric line shape, representing the higher statistical weight of orientations with θ=90 over those with θ=0. Here the minimum is either located below the field corresponding to A^μ for $D_\perp^\mu <0$ or above it if $D_\perp^\mu >0$.

In rigid media the $\Delta M = 1$ resonance has the most intense transition and has been shown to be a sensitive tool in the study of reorientational dynamics of radicals. A good
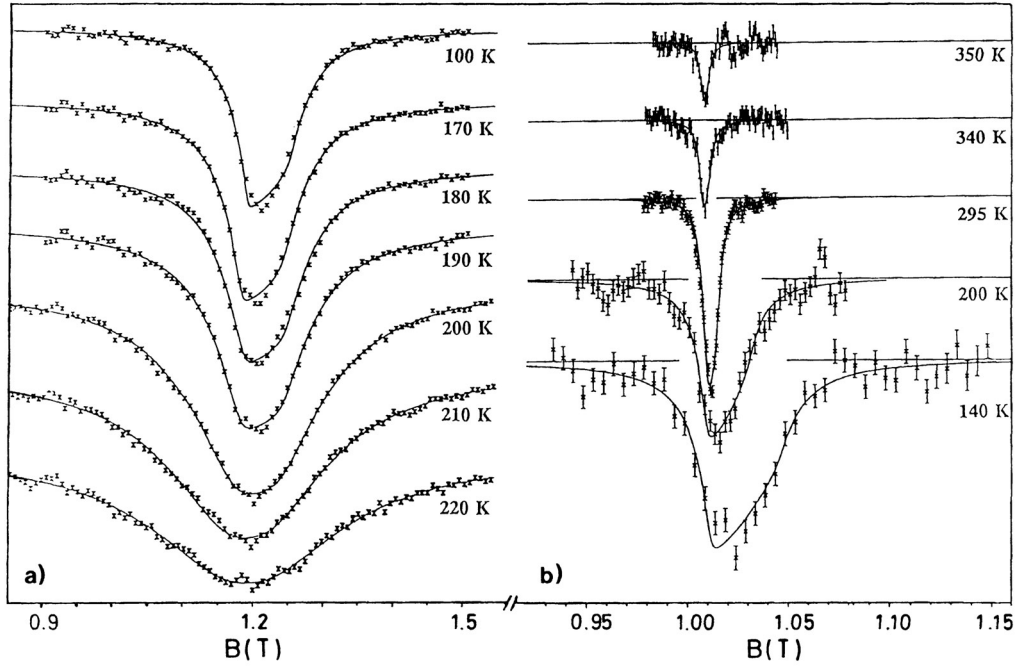
Figure 3.6: *ALC-μSR spectra obtained of polycrystalline C_{60} (a) and C_{70} (b). The opposite trends of the line widths with temperature demonstrate two fundamentally different types of dynamics despite the similarity of the two fullerenes. This figure is taken from Ref. [9], with permission from Elsevier Science. For both samples at low temperatures the characteristic powder pattern is observed. Because the minima are located at a field below the peak center, on can conclude $D_{\perp}^{\mu} <0$, see text.*

illustrative example of this are experiments done on muonated radicals of C_{60} and C_{70} [9]. For both fullerenes, an intense asymmetric resonance, accredited to the $\Delta M = 1$ transition, has been observed. The change in the form of this resonance, as a function of temperature is, however, markedly different as is illustrated in Fig 3.6. In C_{60} the resonance broadens with increasing temperature, whereas in C_{70} it continuously narrows. The results obtained for C_{70} have been analyzed in terms of a pseudo-static model in which the narrowing with increasing temperature is ascribed to a smaller effective anisotropy. The broadening observed for C_{60} on increasing temperature was described well by a stochastic Liouville mechanism for spherical rotational diffusion. Lineshapes and the dependence on the characteristic timescale of the dynamics for various types of stochastic motions have been considered using Monte Carlo methods [10] showing a range of characteristic lineshape behaviours.

3.5.5 Relaxation in muonium and muonated radicals

In contrast to avoided level crossings which basically depend on a static or time averaged interaction which mixes the crossing levels, relaxation is due to transitions induced by fluctuations in the muon's magnetic environment. This can either be due to librations of groups atomic group within the molecule or vibrations and rotations of the entire molecule in its surrounding. The general and commonly used model to describe these fluctuations

is based on random jumps between two values. The correlation function can be shown to exhibit exponential decay with time, where the exponent reflects the typical time scale of the fluctuations, usually indicated as the correlation time τ_c. Transferring the correlation function to the frequency domain results in a Lorentzian shaped spectral density function $J(\omega_{ij})$. On the other hand the intensity of the relaxation is proportional to the transition probabilities of the fluctuating perturbation inducing the transition $|M_{ij}|^2 = |\langle\psi_i|\hat{H}_1|\psi_j\rangle|^2$. Combining these two results in a common formulation of time-dependent perturbation theory:

$$\lambda_z(B,\tau) \propto |M_{ij}|^2 J(\omega_{ij}) = |M_{ij}|^2 \tau_c/(1 + \omega_{ij}^2 \tau_c^2) \tag{3.33}$$

Here $J(\omega_{ij})$ exhibits a maximum whenever the transition frequency ω_{ij} matches the correlation time of the system, *i.e.* $\omega_{ij}\tau_c = 1$. This is similar to the "T$_1$ minima" in NMR, and provides an invaluable calibration for the absolute value of the fluctuation rate $1/\tau_c$. Notice that the relaxation rate is proportional to the fluctuation rate in the slow fluctuation regime but inversely proportional above it (*i.e.* compared to the transition frequency). While running an experiment two parameters can be changed. First of all the magnetic field which influences both $|M_{ij}|^2$ and ω_{ij}. Furthermore, because molecular dynamics are driven by thermal energy, the temperature of the system will set the fluctuation rate $1/\tau_c$. For the latter an Arrhenius law is commonly used to obtain an activation energy and an attempt frequency of the motion.

As mentioned earlier, the reorientation of the radical induces transitions in the Breit-Rabi diagram. The transition probabilities $|M_{12}|^2$ induced by a fluctuating dipolar contribution on a static isotropic hyperfine energy level scheme are given in Fig 3.5. In the lower part of the figure, the development of the relaxation rate itself is indicated. From both Fig 3.5 and Eq. 3.33 one can see that λ_Z peaks whenever the transition frequency approaches to zero. This situation occurs at zero field, when a singlet and a triplet state are formed. More remarkably, this happens at a crossing as well. So near a level crossing, one could expect an increase of the relaxation rate centered on the level crossing [11].

$$\star \quad \star$$
$$\star$$

Bibliography

[1] R. Kubo and T. Toyabe, *Magentic Resonance and Relaxation* p.810 Adam North-holland, Amsterdam 1967

[2] R.S. Hayano, Y,J. Uemura, J. Imazato, N. Nishida, T. Yamazaki and R. Kubo, Phys. Rev. B **20** (1979) 850

[3] P. Dalmas de Réotier and A. Yaouanc, J. Phys.: Condens. Matter **9** (1992) 4533

[4] A. Abragam, *The principles of nuclear magnetism*, Oxford university press, Oxford

[5] C.P. Slichter, *Principles of Magnetic Resonance*, Springer-Verlag, Berlin

[6] A. Schenck, *Muon spin spectroscopy, Principles and applications in solid state physics* Adam Hilger Ltd, Bristol 1985

[7] F.L. Pratt, Phil. Mag. Letters, **75**, 371 (1997)

[8] E. Roduner, Hyperfine Interact. **65** (1990) 857

[9] E. Roduner, KJ. Prassides, R.M. Macrae, I.M. Thomas, C. Niedermayer, U. Binninger, C. Bernhard, A. Hofer and I.D. Reid, Chem. Phys. **192** (1995) 231

[10] P.L.W. Tregenna-Piggott, E. Roduner and S. Santos, Chem. Phys. **203** (1996) 317

[11] S.F.J. Cox and D.S. Sivia, Appl. Magn. Reson. **12** (1997) 213

Chapter 4

Li mobility in the battery cathode material $\mathrm{Li}_x[\mathrm{Mn}_{1.96}\mathrm{Li}_{0.04}]\mathrm{O}_4$

Abstract

The battery cathode materials $\mathrm{Li}_x[\mathrm{Mn}_{1.96}\mathrm{Li}_{0.04}]\mathrm{O}_4$ with $x{=}1$ and 0.2 were studied by μSR. Both materials have a magnetic transition below $T_M \simeq 25$ K. At high temperature, above $T{=}230$ K, a large decrease of the width of the static field distribution at the muon site is found for $\mathrm{Li}[\mathrm{Mn}_{1.96}\mathrm{Li}_{0.04}]\mathrm{O}_4$, providing proof of the onset of the mobility of Li^+ ions in the microsecond time range. On the other hand in $\mathrm{Li}_{0.2}[\mathrm{Mn}_{1.96}\mathrm{Li}_{0.04}]\mathrm{O}_4$ the onset of the Li^+ ion mobility occurs only for $T >300$ K, *i.e.*, just above room temperature.

4.1   Introduction

The use of all kinds of portable consumer electronics, ranging from cameras and personal audio to electronic notebooks and cellular phones, has increased the demands and specifications on the batteries used to operate them. Future applications in *e.g.* electrical vehicles, storage of solar cell electricity and load-leveling of power plants will only tighten these specifications for a more efficient use. The most obvious specification is the weight of the battery, because they are commonly used in portable devices. To limit the weight, attention has been focused on battery materials with a high-energy density. Other performance specifications concern the nominal voltage, the temperature range of operation and the number of recharge-cycles that can be performed before the battery wears out. In this respect Li-ion batteries are very promising compared to other existing battery systems. Apart from the performance specifications, there is also a demand for materials which are kind to the environment. This requirement encourages alternatives for the heavy metals in common rechargable batteries such as *e.g.* NiCd, because these are the main source of pollution. In addition, one would prefer all-solid-state batteries, both to improve performance and prevent leakage. Again, some Li-ion batteries seem to meet these specifications nicely and have been commercialized recently [1, 2]. The cathode materials used in these batteries are $LiNiO_2$ or $LiCoO_2$. Another promising candidate for cathode material is $LiMn_2O_4$ [3]. The rechargeable capacity of $LiMn_2O_4$ is comparable to that of $LiCoO_2$. However, $LiMn_2O_4$ is easier to prepare and less expensive than both $LiNiO_2$ or $LiCoO_2$. Therefore the overall cost of the battery would be reduced if $LiMn_2O_4$ were used as cathode material. In all these Li-ion batteries the Li^+-ions take care of the charge transport, as will be explained below. For this reason one is interested in the mobility and dynamics of the Li-ions in the battery materials. This chapter reports on a μSR study on the Li^+ mobility in the cathode material $Li_x[Mn_{1.96}Li_{0.04}]O_4$.

4.2   Li-ion batteries

All Li-ion batteries are based on the same concept of the transport of Li^+ ions, between the anode through an electrolyte to the cathode. A battery is recharged by an external voltage causing a flow of Li^+ ions to the anode, where they intercalate and are stored for later use. The backflow of Li^+ ions between the anode and the cathode generates the
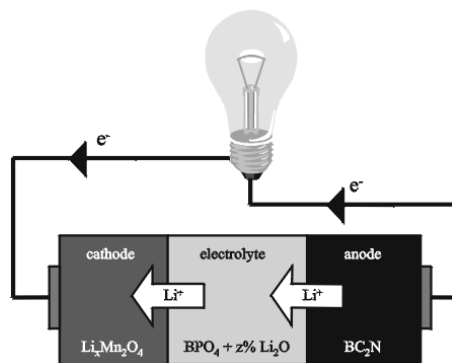

Figure 4.1: *Principle of a battery based on the cathode material $Li_x[Mn_{1.96}Li_{0.04}]O_4$ working as a power supply. The Li^+ ions diffuse from the anode to the cathode.*
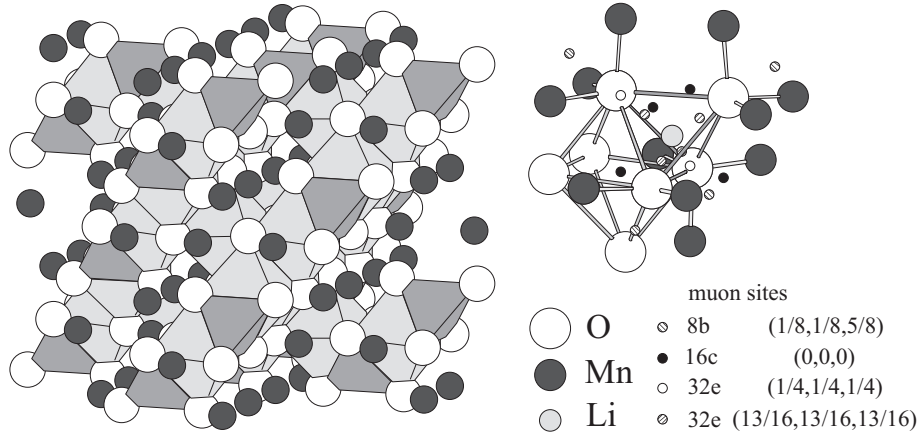
Figure 4.2: *On the left the spinel structure of $LiMn_2O_4$, with the dark tetrahedra connecting the oxygen and centered around the Li atoms (not visible here). The grey octahedra enclose the 16c site. On the right a cut out is shown which focusses on the Li and 16c sites within the tetrahedral and octahedral surrounding oxygen. Furthermore some possible muon sites are indicated in their local surrounding (see Table 4.2).*

power of the battery. This only occurs if a connection is established between the anode and the cathode to conduct the electrons, because these are not able to travel through the electrolyte. This is illustrated in Fig. 4.1 were the flow of the Li^+ ions induces a voltage difference between the anode and the cathode of the battery when it is used as a power supply. Batteries can be made by stacking thin separate foils of cathode, electrolyte, anode and insulating material. These can be wound several times on copper core to increase the effective area, and afterwards compacted to improve the interfacial contact between the different cell components (see *e.g.* Ref. [4]).

4.3 The battery cathode material $\mathbf{Li}_x[\mathbf{Mn}_{2-y}\mathbf{Li}_y]\mathbf{O}_4$

Here we will focus on the cathode material $Li_xMn_2O_4$, which in combination with boron-phosphate as an intermediate solid electrolyte and carbon or B_2CN as anode forms an excellent solid state rechargeable battery. Materials of the composition $Li_x[Mn_{2-y}Li_y]O_4$ have a cubic spinel structure ($MgAl_2O_4$ structure; space group $Fd\bar{3}m$). In this structure the Mn-ions occupy the $16d$ octahedral sites and the Li-ions occupy the $8a$ tetrahedral sites in a cubic closed-packed lattice of O-ions. The spinel structure of $LiMn_2O_4$ is illustrated in Fig. 4.2.

Batteries with a cathode of $Li_xMn_2O_4$ operate between the $x = 0.2$ ('charged') and $x = 1$ ('empty') states. Here x refers to the occupation probability of the regular Li $8a$ sites. In $LiMn_2O_4$ ($x = 1$) equal amounts of Mn^{3+} and Mn^{4+} ions are present. This compound is a hopping electronic conductor in which electrons move between adjacent Mn sites. It undergoes at ~ 290 K a structural phase transition attributed either to a partial charge ordering or a cubic-tetragonal structural phase transition driven by a cooperative Jahn-Teller distortion mechanism around the Mn^{3+} cation sites [5, 6]. That transition renders the material unsuitable as cathode because of a poor cycling performance. Li substitution on the Mn site gives rise to an increase in Mn^{4+} concentration and subsequently a decrease in Mn^{3+} concentration. This leads to an increased stability of the cubic spinel

structure as shown by a recent powder neutron diffraction study, which did not detect for $Li[Mn_{1.96}Li_{0.04}]O_4$ any structural phase transition from room temperature down to 4.2 K [7]. The thermal variation of the lattice parameter is far less than 1% in this temperature range. The absence of this transition makes the compound more suitable as a cathode. On the other hand, for an efficient operation of the cathode the amount of Li substitution, i.e. the amount of Mn^{4+} ions, should not be too large. Optimal battery prototypes work with $0.04 \leq y \leq 0.06$.

Optimizing the cathode material $Li_x[Mn_{2-y}Li_y]O_4$ would be highly desirable. This purpose can only be reached if the Li^+ ion mobility for different x and y values is known, and up to now there is only very limited information on that matter. The linewidth of the ^6Li and ^7Li nuclear magnetic resonance (NMR) spectra exhibits a probable motional narrowing above ~ 230 K for $LiMn_2O_4$, indicating that the Li^+ ions might diffuse at high temperature [8]. The work presented in this chapter contains a detailed investigation of the Li^+ ion behaviour by the zero-field muon spin relaxation (μSR) technique for $x = 1$ and $x = 0.2$ with $y = 0.04$.

4.4 Preparation and characterization $Li_x[Mn_{2-y}Li_y]O_4$

The samples were synthesized by mixing manganese acetate tetrahydrate $(Mn(CH_3COO)_2.4H_2O)$ and an appropriate amount of lithium hydroxide monohydrate $(LiOH.H_2O)$ [9]. Calcination was performed at 650 °C. $Li_{0.2}[Mn_{1.96}Li_{0.04}]O_4$ was prepared from $Li[Mn_{1.96}Li_{0.04}]O_4$ using concentrated sulphuric acid. All samples were prepared at the Laboratory of Applied Inorganic Chemistry at the Delft University of Technology.

Neutron diffraction showed that the materials have the expected spinel structure with lattice parameters $a = 8.23$ and 8.05 Å at room temperature for $Li[Mn_{1.96}Li_{0.04}]O_4$ and $Li_{0.2}[Mn_{1.96}Li_{0.04}]O_4$, respectively [10]. The size of the grains is ~ 25 μm as shown from scanning electron microscopy. Flame atomic adsorption spectroscopy indicated that the amount of elements present in the samples is correct. Furthermore, the powders were analysed by the Jaeger and Vetter titration method in order to determine the Mn valency [11]. It was found that the Mn valencies are 3.55 and 3.96 for $x = 1$ and $x = 0.2$, respectively. These values are in the expected range.

The μSR measurements on both compounds were performed at both the EMU and MuSR spectrometers of the ISIS facility located at the Rutherford Appleton Laboratory in England. Measurements below 400 K were done on a closed cycle cryostat (CCR); for higher temperatures a furnace was used. The powder samples were ground and pressed into 1 cm diameter and 1.5 mm high pellets with a 4 ton load. For use in the CCR, these pellets were glued onto silver plates to cover the full beam spot of 3 cm diameter. In the furnace a 2.5 cm diameter titanium cup shaped sample holder with a window of titanium foil was used. Here silver and titanium are used as sample holder material because both have a very low and only slightly temperature dependent depolarization.

4.5 Experimental Results

For both $Li[Mn_{1.96}Li_{0.04}]O_4$ and $Li_{0.2}[Mn_{1.96}Li_{0.04}]O_4$, a number of μSR spectra were recorded in a longitudinal set up over a range of temperatures. Fig. 4.3 shows the spectra of $Li[Mn_{1.96}Li_{0.04}]O_4$ at 35 K and 100 K. Apart from the fact that at low temperatures

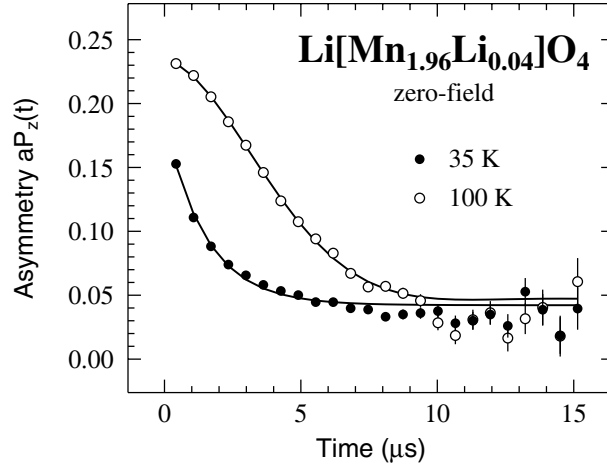Figure 4.3: *μSR spectra of Li[Mn$_{1.96}$Li$_{0.04}$]O$_4$ measured in zero-field at 35 K and 100 K. At 35 K the fluctuations of Mn magnetic moments dominate, resulting in an exponential (i.e. linear at small times) depolarization. Whereas around 100 K this contribution is small compared to the depolarization induced by the nuclear moments, for which the dynamical Kubo-Toyabe depolarization function, gives a more or less Gaussian depolarization at small times.*

the initial asymmetry is lower and the depolarization is stronger, one can also see that the shapes of the spectra are quite different. Whereas the 35 K spectrum can be fitted nicely by a simple exponential, at 100 K the spectrum starts off more or less Gaussian. This difference can be attributed to two different origins of depolarization dominating the low and the higher temperature regimes.

Below 50 K, the signals of the samples are well fitted with a single exponential function $\exp\left(-\lambda_Z t\right)$ characterized with a relaxation rate λ_Z. This function describes the magnetic fluctuations of the electronic moments on the manganese. Because these fluctuations are fast compared to the muon lifetime τ_μ, one can use the motional narrowing limit, resulting in a simple exponential decay of the polarization (see Eq. 3.13).

At temperatures above 100 K, the depolarization is mainly due to the field distribution induced by the nuclear magnetic moments at the muon site. It is described by a dynamical Kubo-Toyabe function $P_{\mathrm{KT}}(\Delta, \nu, t)$ where Δ^2 is the variance of the field distribution (of nuclear origin) at the muon site and ν the correlation frequency, or alternatively the muon hopping rate (Refs. [12, 13]).

Although in a given temperature regime, one depolarization process dominates over the other, and *vice versa*, both are present over the whole temperature range. This is illustrated in Fig. 4.4. Here at zero-field and 270 K, the depolarization is due to the field distribution of the nuclear moments. However, when a external field of 10 mT is applied, which is large compared to the nuclear fields at the muon site, this static component is completely quenched *i.e.* $P_{\mathrm{KT}}(\Delta, \nu, t) = 1$, see section 3.2, and a slow depolarization due to electronic fluctuations is left.

Because both depolarization processes are uncorrelated, the total muon spin depolarization function is given by their product. The model which fits the depolarization over the whole experimental temperature range is now given by the sum of two components:

$$aP_Z(t) = a_{\mathrm{s}} P_{\mathrm{KT}}(\Delta, \nu, t) \exp\left(-\lambda_Z t\right) + a_{\mathrm{bg}}. \tag{4.1}$$
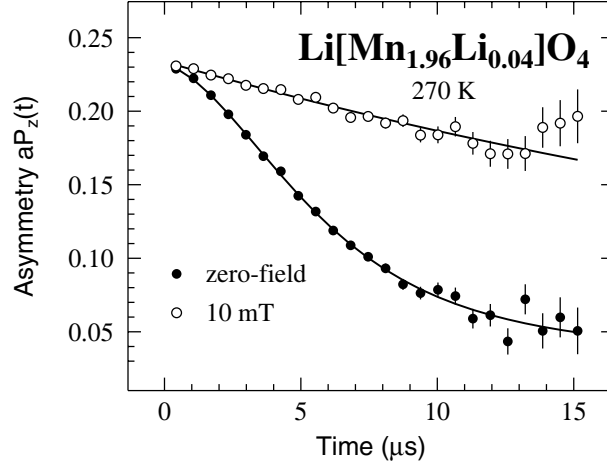
Figure 4.4: *Comparison of μSR spectra of Li[Mn$_{1.96}$Li$_{0.04}$]O$_4$ measured at zero-field and 10 mT at 270 K. The small field quenches the nuclear contribution to the depolarization, leaving only the small electronic depolarization*

The first component accounts for the muons implanted in the sample and the second component describes the muons stopped in the silver sample holder and cryostat or furnace walls. As expected, this latter component is time independent with an associated asymmetry a_{bg}. a_s is the asymmetry associated with the sample and a the total asymmetry.

First the results on the electronic fluctuations will be presented. At temperatures below 50 K the nuclear contribution could be neglected, *i.e.* $P_{KT}(\Delta, \nu, t) = 1$, resulting in a single exponential fit. In order to reliably measure λ_Z above 100 K, experiments have been performed with longitudinal magnetic fields sufficiently large, *i.e.* above 10 mT, to quench the nuclear depolarization. The results for both the initial asymmetry a_s and the damping rate λ_Z are shown in Fig. 4.5.

On cooling towards the ordering temperature T_M, the fluctuations of the electronic moments slow down, and start to depolarize the muon spins more efficiently. This is observed in Fig. 4.5, where λ_Z starts to increase below 50 K and exhibits a maximum at 25 K, which is taken as the ordering temperature T_M. At $\sim$ 50 K a_s gradually starts to decrease and drops below T_M which again points to a magnetic phase transition at that temperature. The absence of an oscillating component of the muon signal below T_M means that the spontaneous magnetic field at the muon site is too large to be detected at ISIS, or the magnetic field distribution is extremely wide. One would expect the initial asymmetry to drop from a_s in the paramagnetic state to $a_s/3$ in the ordered (section 3.2). In this case, however, the drop seems to be even larger. This is an indication that the spin lattice relaxation rate must be important here.

No sharp magnetic Bragg reflections have been observed by neutron diffraction in Li[Mn$_{1.96}$Li$_{0.04}$]O$_4$ [7]. In contrast, neutron diffraction in Li$_{0.2}$[Mn$_{1.96}$Li$_{0.04}$]O$_4$ shows a doubling of the cubic unit cell, indicating long range antiferromagnetic ordering. Therefore, combining the μSR and neutron results we infer that magnetic correlations develop at low temperature in both compounds.

Although the low temperature data are interesting for magnetic ordering, it does not give any direct insight on the mobility of the Li-ions. Therefore, from this point we will focus on the high temperature data, in which the depolarization is dominated by the
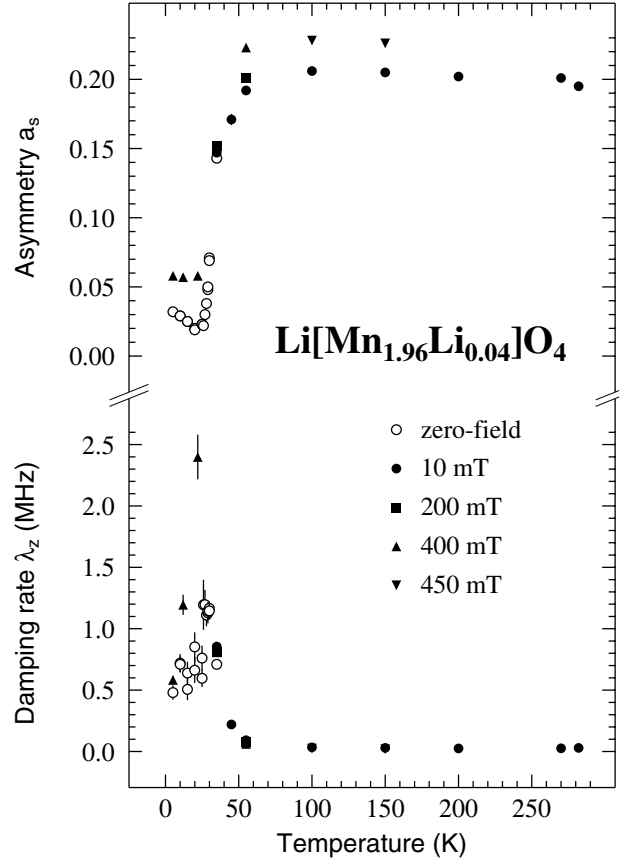
Figure 4.5: *Initial asymmetry and the damping rate due to fluctuations of the electronic spins on the Mn-ions in Li[Mn$_{1.96}$Li$_{0.04}$]O$_4$. The loss of initial asymmetry and the maximum in the damping rate at 25 K indicate magnetic ordering*
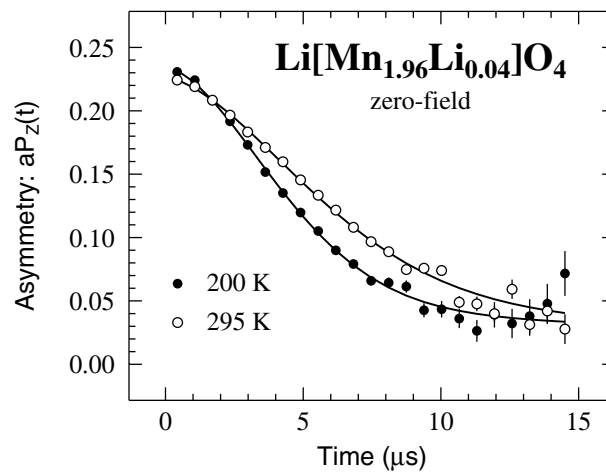
Figure 4.6: *μSR spectra of Li[Mn$_{1.96}$Li$_{0.04}$]O$_4$ measured in zero field at 200 K and 295 K. The solid lines are fits as described in the text.*

field distribution induced by the nuclear moments. In Fig. 4.6 μSR spectra recorded for Li[Mn$_{1.96}$Li$_{0.04}$]O$_4$ at 200 K and 295 K in zero field are compared. At 200 K a stronger
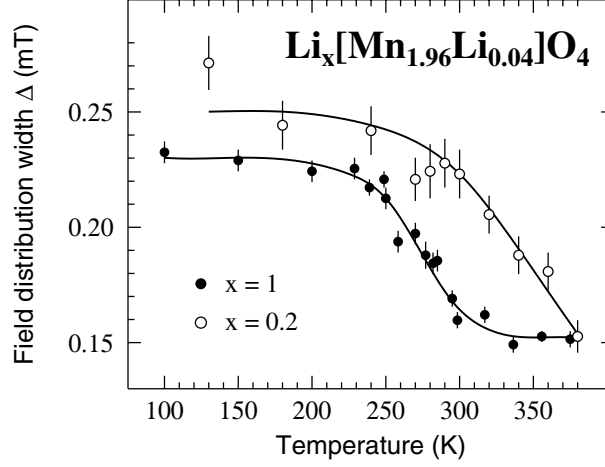
Figure 4.7: *Kubo-Toyabe linewidth Δ measured up to 380 K for $Li[Mn_{1.96}Li_{0.04}]O_4$ and $Li_{0.2}[Mn_{1.96}Li_{0.04}]O_4$. Whereas Δ drops between 230 K and 300 K for $Li[Mn_{1.96}Li_{0.04}]O_4$, for $Li_{0.2}[Mn_{1.96}Li_{0.04}]O_4$ it starts to be temperature dependent only above $\sim$ 300 K. The solid lines serve as a guide to the eyes.*

depolarization than at 295 K is observed. This is confirmed by the values of the field width Δ extracted from the fit of the spectra as shown in Fig. 4.7. A drop of Δ as large as $\sim 35\%$ is detected between 230 K and 300 K for $Li[Mn_{1.96}Li_{0.04}]O_4$. As seen in Fig. 4.7, for $Li_{0.2}[Mn_{1.96}Li_{0.04}]O_4$ the drop of Δ is even larger but only starts at $\sim$ 300 K. Remarkably, at low temperature in the plateau region, Δ is only slightly larger for $Li_{0.2}[Mn_{1.96}Li_{0.04}]O_4$ than for $Li[Mn_{1.96}Li_{0.04}]O_4$.

The thermal dependence of Δ can not be due to a muon diffusion effect. In fact the muon is quasi static for both compounds in the whole temperature range investigated. This is shown qualitatively by the parabolic shape of the spectra at small times (see Fig. 4.6) and confirmed quantitatively by the results of the fits which show that ν is roughly temperature independent with a value of about 0.1(1) MHz and 0.6 (1) MHz for the $x = 1$ and $x = 0.2$ compounds, respectively. Therefore the mean time of residence of the muon in an interstitial site is larger or approximately equal to the muon lifetime.

Additionally, some measurements for the two compounds have been performed up to 600 K in vacuum. In Fig. 4.8 we compare two spectra recorded at 300 K on $Li[Mn_{1.96}Li_{0.04}]O_4$. One spectrum was taken before heating above 300 K. The other spectrum was recorded after measurements done up to 600 K. Although the sample was expected to be stable, the spectra are clearly different. Our results indicate that for $Li[Mn_{1.96}Li_{0.04}]O_4$ some structural changes take place above 380 K, possibly related to loss of oxygen from the structure. In $Li_{0.2}[Mn_{1.96}Li_{0.04}]O_4$ a similar irreversible behaviour was observed. This is not surprising since for this sample specific heat measurements indicates that part of the material starts to dissociate at $\sim$ 490 K [14]. In conclusion, our results indicate that for $Li[Mn_{1.96}Li_{0.04}]O_4$ a structural change takes place above 380 K.
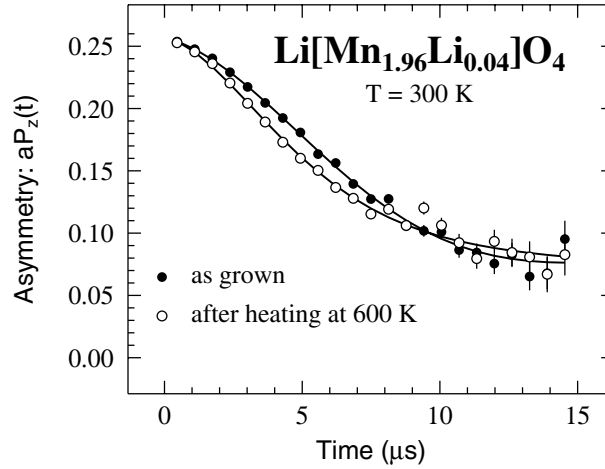
Figure 4.8: *Comparison of μSR spectra of Li[Mn$_{1.96}$Li$_{0.04}$]O$_4$ measured in zero field at 300 K. The solid lines are fits as described in the main text. The spectra presented in Figs. 4.6 and 4.8 were recorded with different experimental setups. This explains the slightly different a_s and a_bg values.*

4.6   Discussion and conclusions

The nuclear depolarization is induced by the field distribution at the muon site which is composed from the contributions of the Mn and Li nuclear magnetic moments. Since the measured depolarization is typical of a static field distribution, the Mn and Li ions are static. Therefore, the decrease of Δ at high temperature for Li[Mn$_{1.96}$Li$_{0.04}$]O$_4$ and Li$_{0.2}$[Mn$_{1.96}$Li$_{0.04}$]O$_4$ can only be understood if we suppose that some of the Li$^+$ ions no longer contribute to the depolarization. This means that, as the temperature is raised, some of the Li$^+$ ions diffuse, and their contribution is then motionally narrowed.

Table 4.1: *Isotopes, abundancies and gyromagnetic ratios for all elements in Li[Mn$_{1.96}$Li$_{0.04}$]O$_4$. The gyromagnetic ratios were determined with $\gamma_j = \mu\mu_N/I_j\hbar$. The values for μ and I_j were taken from the CRC Handbook of Chemistry and Physics [15].*

isotope	abundancy %	spin I_j $\hbar$	gyromagnetic ratio γ_j Mrad s^{-1}T^{-1}
^{6}Li	7.43	1	39.369
^{7}Li	92.57	3/2	103.963
^{17}O	.04	5/2	36.278
^{55}Mn	100	5/2	66.305

For a given muon site Δ can be computed if the configuration of the surrounding isotopes is known. It is expressed as a lattice sum over the atoms which carry a nuclear magnetic moment [13]. For powder samples, as in the present case, the result depends only

on the distance between the muon and the atoms and the value of the nuclear moments:

$$\Delta_{KT}^2 = \frac{2}{3} \sum_j \left(\frac{\mu_0}{4\pi} \frac{\hbar}{r_j^3} \right)^2 \sum_{\alpha=1}^{\nu(j)} P_j(\alpha) \gamma_{j,\alpha}^2 I_{j,\alpha}(I_{j,\alpha}+1) \tag{4.2}$$

Here, the sum is taken over all nuclei, with their corresponding abundance $P_j(\alpha)$, spin $I_{j,\alpha}$, gyromagnetic ratio $\gamma_{j,\alpha}$, located at a distance r_j from the muon site. The effect of the electric field gradient on the nuclear moments has been neglected. This gradient reduces the associated depolarization rate by $\sim 15\%$ at most. The required constants for the relevant elements are given in Table 4.1. Table 4.2 lists the computed Δ values for eight possible muon sites in $LiMn_2O_4$ for both with and without the Li contribution. Clearly, the Li contribution to Δ is small except for the $16c$ and $32e$ sites. The possibility of muon localization at the Li regular site has been included, because NMR and neutron diffraction data allow an analysis with ~ 5 % of vacant Li sites [10]. Furthermore, it needs to be mentioned that for the $32e$ $(\frac{13}{16}, \frac{13}{16}, \frac{13}{16})$ muon site, which could correspond to an oxygen muon bond (see further on in the text), the nearest Li-site was presumed vacant.

One major property of Δ has to be explained: relative to its low temperature value, its high temperature value is strongly reduced for both compounds. Inspection of the results listed in Table 4.2 shows that it can not be understood if the muon located at a unique type of site. On the other hand, as discussed below, the Δ behaviour can be explained qualitatively if we suppose that the muon localizes in more than one type of site. For this discussion it is important to note that the muon spectra have an approximately Gaussian shape as seen in Fig. 4.6. Therefore it is a good approximation to write $\Delta^2 = \sum_i p_i \Delta_i^2$ where p_i is the relative muon occupancy of site i.

Let us first consider the $Li[Mn_{1.96}Li_{0.04}]O_4$ case. At low temperature the value of Δ can be explained, if we suppose that the muon is mostly in site $8a$ (i.e. at a Li vacancy) with a small probability to be in another site, as for instance 10% in site $16c$ (see column 3 of Table 4.2). The high temperature value is understood with the same muon sites if the Li contribution is motionally narrowed (see column 4 of Table 4.2), i.e. if the contribution of the Li^+ ions to the field distribution at the muon site vanishes due to fast diffusion of these ions with a mean time of residence smaller than ~ 0.1 μs.

Now the value of Δ measured for $Li_{0.2}[Mn_{1.96}Li_{0.04}]O_4$ at low temperature will be considered. First note that taking into account the 2.5 % measured lattice contraction of the $x=0.2$ compound compared to the $x=1$ compound [10], the Δ_i values are derived by increasing the values given in Table 4.2 by 7.7 %, because Δ is inversely proportional to the cubic power of r_j. We stress that the Li^+ ions taken out of the $Li[Mn_{1.96}Li_{0.04}]O_4$ crystal structure to get the $Li_{0.2}[Mn_{1.96}Li_{0.04}]O_4$ compound are from the regular Li $8a$ site. Since the comparison between the values given at columns 3 and 4 of Table 4.2 for that site shows that the Li nuclear moments have a very little effect on Δ_i, it can be concluded that, at low temperature, the muon occupies the same sites for $Li_{0.2}[Mn_{1.96}Li_{0.04}]O_4$ and $Li[Mn_{1.96}Li_{0.04}]O_4$ with approximately the same probabilities.

Again, the decrease of the width of the field distribution at high temperature for $Li_{0.2}[Mn_{1.96}Li_{0.04}]O_4$ is understood invoking the motional narrowing of the Li contribution. But the difference observed for $\Delta(T)$ for the two compounds indicates that the Li^+ ion diffusion starts only above room temperature for the $x = 0.2$ compound. In addition, it is much more progressive than for the $x = 1$ compound since Δ for $x = 0.2$ is larger than for $x = 1$ below 380 K.

Table 4.2: *Results of the computation of Δ_i for different sites i in $LiMn_2O_4$. The sites are labeled using the Wyckoff notation (column 1) and their coordinates are given at column 2 (origin at center ($\bar{3}$m), space group $Fd\bar{3}m$). The Δ_i values with and without the Li contribution are listed in columns 3 and 4, respectively. The effect of a possible electric field gradient acting on the Mn and Li sites and an eventual contraction or expansion of the lattice around the muon are neglected. The 8a site is the regular Li site. The other sites are interstitial.*

Wyckoff	μ-site coordinates	calculated Δ_i values in mT with Li	without Li
8a	$(\frac{1}{8},\frac{1}{8},\frac{1}{8})$	0.178	0.158
8b	$(\frac{1}{8},\frac{1}{8},\frac{5}{8})$	0.609	0.601
16c	$(0,0,0)$	0.462	0.188
32e	$(\frac{1}{4},\frac{1}{4},\frac{1}{4})$	0.467	0.351
32e	$(\frac{13}{16},\frac{13}{16},\frac{13}{16})$	0.221	0.200
48f	$(\frac{1}{8},\frac{1}{8},\frac{3}{8})$	0.492	0.439
48f	$(\frac{1}{8},\frac{1}{4},\frac{5}{8})$	0.801	0.793
96g	$(0,\frac{7}{8},\frac{1}{8})$	0.613	0.578

Recently, new ^{7}Li NMR experiments were performed for $Li[Mn_{1.96}Li_{0.04}]O_4$ [16]. Three different Li signals were found. The most intense arises from Li on the regular 8a site. The two weaker signals are due to Li on Mn sites and to interstitial sites, most likely the 16c sites. This is consistent with our interpretation of the μSR results. The preliminary analysis shows that Li$^+$ ions are mobile below room temperature, in agreement with the μSR data.

Local mobility of Li$^+$ ions on a picosecond time scale was detected in Li_2MnCl_4 by inelastic neutron scattering [17]. As mentioned above, the μSR technique is sensitive to a much longer time scale (≥ 0.1 μs) and this suggests that a Li$^+$ long range diffusing motion is detected in the μSR experiment [17].

In contrast to the Li$^+$ ion behaviour, the muon is quasi-static in the whole temperature range investigated. Although this can be understood if the diffusing particle passes through a bottle neck in the transition state , it is not obvious that such a model applies [18]. Another option, the possibility for the muon to form a 1 Å oxygen-muon bond as found in other oxides, has also been investigated [19]. This could explain the quasi-static muon. The best qualified oxygen muon site would be the 32e ($\frac{13}{16}, \frac{13}{16}, \frac{13}{16}$) site, situated at 1 Å from the oxygen as required (see Fig 4.2). Besides that, it is at a maximum distance to the nearest Mn atoms, which dominate the depolarization at high temperatures. Although the low temperature value is not inconsistent with the measured field inhomogeneity, the high temperature limit drop of only 9% is not compatible with the measured 0.15 mT.

So far the muon was considered quasi-static, because a small magnetic field quenched the depolarization, and the parabolic shape at the start of the spectra. The strong collision approximation, which defines the dynamical Kubo Toyabe function used, predicts an

exponential depolarization if the correlation frequency ν_c exceeds the field distribution. Nevertheless, in a study on Li_2O, Lord *et al.* assumed a Gaussian lineshape for a muon hopping rapidly between a small number of sites [20]. For this compound a model is used in which the motion of the muon is restricted to a limited number of sites surrounding a Li vacancy. The field experienced by the muon in this scheme will be correlated, due to the very similar environment for each site, and the relatively large probability of the muon to return to sites visited earlier. This is in conflict with the assumption of a sequence of uncorrelated fields used in the strong collision approximation. Lord *et al.* argue that, provided the hop rate is sufficiently high enabling it to revisit a site several times, the muon will experience an effective field which is a vector average of all individual field contributions. Field distributions $\langle\Delta_i\rangle$ were calculated by randomly choosing orientations of near neighbor spins and calculating the local field. Afterwards a Monte Carlo technique was used to average over a large number of possible spin configurations.

The effective Gaussian lineshape is still under discussion. To settle this an extensive Monte Carlo simulation monitoring the muon spin for an ensemble of muons will be needed, and this is beyond the scope of this thesis. In advance of this result and to test this option, computations similar as those on Li_2O have been performed.

Table 4.3: *Results for computation of $\langle\Delta_i\rangle$ for different sites i in $LiMn_2O_4$. The sites considered are situated on or within the tetrahedra of oxygen enclosing the Li, see Fig. 4.2. The positions within this tetrahedron are described in column 2. Motional narrowing was considered by averaging over a given number of identical sites either on the same oxygen atom, or within the same tetrahedron. Calculated $\langle\Delta_i\rangle$ values with and without the Li contribution are listed in columns 4 and 5, respectively. Here the 8a Li position in the center of the relevant tetrahedron is assumed to be vacant. The effect of a possible electric field gradient acting on the Mn and Li sites, and an eventual contraction or expansion of the lattice around the muon, are neglected.*

	μ-site	number of sites in average	calculated $\langle\Delta_i\rangle$ values in mT with Li	without Li
a	on line connecting	1	0.262	0.244
	oxygen on tetrahedron	3	0.238	0.220
	at 1 Å of oxygen	12	0.189	0.170
b	on the center of the	1	0.231	0.207
	line connecting	3	0.196	0.174
	two oxygen atoms	6	0.183	0.161
c	on the center of the	1	0.193	0.167
	face of a tetrahedron	4	0.172	0.156
d	at 1 Å of oxygen	1	0.221	0.200
	directed towards Li vacancy	4	0.178	0.165

In order for calculated field distributions, Δ_i, to correspond with the experimentally observed values, it proved necessary to maximize the distance to magnetic moments on

both the Li and Mn nuclei. This complies with a muon positioned at a vacant Li site. Other relatively distant muon sites lie within the tetrahedron defined by the oxygen atoms surrounding a vacant Li $8a$ site. A few positions are described in Table 4.3, in addition to the pair with a possible 1 Å oxygen bond mentioned earlier. For the calculation of $\langle \Delta_i \rangle$, the number of sites visited by the muon is related either by a common neighbor oxygen atom or equivalent sites within the tetrahedron. The number of sites is given in the third column. $\langle \Delta_i \rangle$ was calculated both with and without the Li contribution. The picture of a dynamic muon allows two options to explain the experimental data: Either the muon increases its mobility above 230 K by enlarging the number of optional sites, or the muon hopping remains restricted to the same limited number of sites and Li diffusion starts above this temperature. From Table 4.3 is can be concluded that neither of these options is able to satisfactorily explain the experimentally observed 0.23 mT and 0.15 mT levels for low and high temperature, respectively.

Altogether one can conclude that the most probable origin of the drop in depolarization rate above 230 K is the onset of Li$^+$ diffusion. In this picture the muons are quasi-static and distributed over the $8a$ and $16c$ sites. Furthermore Li$^+$ diffusion on a microsecond time scale starts in Li[Mn$_{1.96}$Li$_{0.04}$]O$_4$ at 230 K and for Li$_{0.2}$[Mn$_{1.96}$Li$_{0.04}$]O$_4$ at 300 K , i.e. just above room temperature.

$$\star \quad \star \quad \star$$

Bibliography

[1] J.R. Dahn, U. Von Stacken and R. Fong, The Electrochemical Society Extended Abstract, Vol 90-2, (Seattle, WA, October 14-19, 1990)

[2] T. Nagaura. 4th Intern. Rechargeable Battery Seminar, Deerfield Beach, Florida (1990)

[3] T. Ohzuku, M. Kitagawa and T. Hira, J. Electrochem. Soc, **137**, 769 (1990).

[4] M.J.G. Jak, *Dynamic Compaction of Li-ion Battery Components and Batteries,*Thesis, Delft University of technology (1999)

[5] J. Rodríguez-Carvajal, G. Roussse, C. Masquelier and M. Hervieu, Phys. Rev. Lett. **81**, 4660 (1998).

[6] V. Massarotti, D. Capsoni, M. Bini, G. Chiodelli, C.B. Azzoni, M.C. Mozzati and A. Paleari, J. of Sol. State Chem. **131**, 94 (1997).

[7] V.W.J. Verhoeven, F.M. Mulder, and I.M. de Schepper,Physica B **276-278**, 950 (2000).

[8] Y.J. Lee, F. Wang and C.P. Grey, J. Am. Chem. Soc. **120**, 12601 (1998).

[9] H. Berg, O. Bergström, T. Gustafsson, E.M. Kelder and J.O. Thomas, J. Power Sources **68**, 24 (1997).

[10] V.W.J. Verhoeven, private communication.

[11] E.M. Kelder, M.J.G. Jak, J. Schoonman, M.T. Hardgrave and S.Y. de Andersen, J. Power Sources, **68** 590 (1999).

[12] P. Dalmas de Réotier and A. Yaouanc, J. Phys.: Condens. Matter **9**, 9113 (1997).

[13] E.B. Karlsson, *Solid State Phenomena as Seen by Muons, Protons and Excited Nuclei*, (Clarendon Press, Oxford, 1995).

[14] O. Schilling and J.R. Dahn, J. Electrochem. Soc. **145**, 569 (1998).

[15] *CRC Handbook of Chemistry and Physics*, edited R.C. Weast, M.J. Astle and W.H. Beyer, (CRC Press Inc., Florida, 1984)

[16] V.W.J. Verhoeven, I.M. de Schepper, G. Nachtegaal, A.P.M. Kentgens, E.M. Kelder, J. Schoonman, and F. Mulder, Phys. Rev. Lett. **86** 4314 (2001)

[17] G.A. Eckstein, G. Eckhold, W. Schmidt, H.J. Steiner and H.D. Lutz, Solid State Ionics **111**, 283 (1998).

[18] E. Roduner in *Muon Science*, edited S.L. Lee, S.H. Kilcoyne and R. Cywinski, (Institute of Physics, London, 1999) pp 173-209.

[19] C. Boekema, A.B. Denison and K.J. Rüegg, Hyperfine Interact. **36**, 111 (1983).

[20] J.S. Lord, S.P. Cottrell and W.G. Williams, J. Phys.: Condens. Matter **10** 7975 (1998)

Chapter 5

Dynamics of ferrocene and ferrocene in KY zeolite

Abstract

Avoided Level Crossing (ALC) and Longitudinal Field (LF) μSR measurements are reported in a study on the reorientational dynamics of polycrystalline ferrocene and ferrocene in a KY zeolite host framework. Multiple ALC peaks and two contributions in the LF-μSR data for both systems, are rationalized with a model involving three radical adducts, two to the cyclopentadienyl ring and the other to the metal. The shift of an ALC and relaxation peak with increasing temperature, is assigned to the metal adduct and described by a model involving spin-orbit coupling. The temperature dependence of the relaxation of these radicals give their activation energies. Differences between the activation energies for the species radicals involved, indicates that the site of muon addition to the molecule influences the molecular dynamics, and provides an insight into the host-guest interactions in ferrocene in zeolite.

5.1 Introduction

The reorientational dynamics of molecules in the voids of zeolite host frameworks has attracted considerable attention over the last few years. The motivation stems from the desire to gain insight in the catalytic properties of zeolites, which depend strongly on the interaction of reactants with the internal surface. These interactions govern the mobility within the zeolite framework.

This study will focus on the dynamics of ferrocene molecules encapsulated in the supercages of KY zeolite. First we will briefly mention the origin of the study as well as the introduction of the individual components and the studies on dynamics done so far. Thereafter we will introduce our intentions for the use of μSR in this study, supported by some previously published μSR experiments.

The interest for ferrocene in zeolite, originated from a search for ways to deposit catalytically active metal atoms in the supercages of zeolites. One way to achieve this could be by vapor phase insertion of volatile organometallics, such as ferrocene, followed by thermal removal of the ligands. In this context the reorientational dynamics of ferrocene in Y-zeolites have been successfully studied by NMR, Mössbauer spectroscopy and neutron scattering methods. The initiated μSR study on this model system offered an opportunity to contribute to the efforts and at the same time explore the possibilities of the μSR techniques involved.

First the two separate materials will be introduced in order to visualize the encapsulated molecule and its plausible dynamics in the supercage.
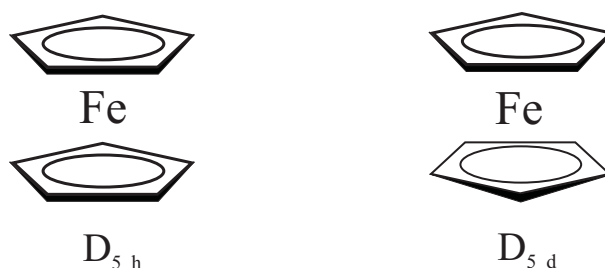
Figure 5.1: *The ferrocene molecule consisting of an iron atom sandwiched in between two parallel cyclopentadienyl rings. Both the eclipsed D_{5h} and staggered D_{5d} configurations are shown.*

Ferrocene, or Fecp$_2$ for short, consists of an iron atom which is sandwiched in between two parallel cyclopentadienyl rings (cp). The rings are made of five carbon atoms (cp=C$_5$H$_5$) with an aromatic bonding and are slightly negatively charged. The iron in the middle, on the other hand is somewhat positive. The rings can be oriented in either the pentagonal antiprism structure (D_{5d}) in which the rings are staggered or a pentagonal prism structure (D_{5h}) in which they are eclipsed. An illustration of the molecule is given in Fig. 5.1. The dimensions of the ferrocene molecule are set by the diameter of the ring and the distance between the rings, 2.3 Å and 3.3 Å respectively.

Zeolites are crystalline alominosilicates with three-dimensional open framework structures built of SiO$_4$ and AlO$_4$ tetrahedra which are interconnected by the oxygen atoms. They have many applications in chemistry, owing to their favorable properties of their open microporous structures, generally consisting of three dimensional interconnected channel systems and cavities. This gives an enormous effective surface, typically hun-

Figure 5.2: *Framework structure of synthetic Y-zeolite. The structure is built from hexagonal prisms and truncated octahedra (left). The supercage in the center hosts the ferrocene molecule. For KY-zeolite the K^+ cations are located at the four SII positions that form a tetrahedron markin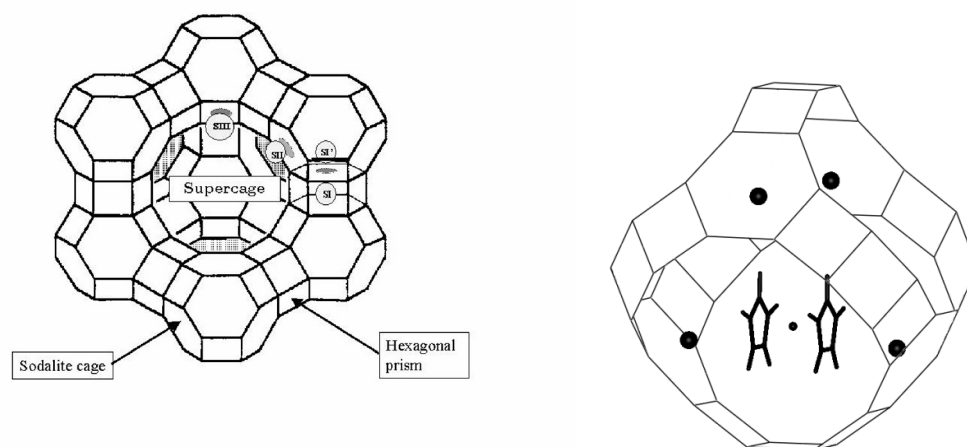g the boundaries of the supercage (right). Recent X-ray and neutron diffraction data locate the ferrocene molecule just above the line joining two neighboring cations [2].*

dred square meters per gram, which is a main advantage in catalytic use. Zeolites are extensively used in petrochemical industry for catalytic cracking of hydrocarbons. On the other hand they are used in detergents for their ion-exchange properties and as molecular sieves due to the confining geometry of their pores. Fig. 5.2 illustrates the structure of the Y-zeolite under study here. Indicated are the supercage and the positions of the K^+ cations that form a tetrahedron marking the boundaries of the cage. The supercage has approximately a spherical shape with a diameter of 11.8 Å, and a circular entrance of 7.4 Å. These sizes make the supercage accessible for up to two ferrocene molecules. The position of a single ferrocene molecule within the supercage was recently determined from neutron scattering and is illustrated in Fig. 5.2.

Several techniques have been applied to study the dynamics of the ferrocene in the supercage. NMR experiments have shown that at low temperatures $Fecp_2$ adsorbs to the zeolite lattice, in such a way that its motional freedom is restricted to rapid rotation of the rings. At increased temperatures reduced NMR lineshapes, suggest that the molecules undergo some kind of isotropic motion [1]. With Mössbauer spectroscopy a decrease of the recoilless fraction was observed. This indicates motion of the iron atom, and suggests that the isotropic dynamics at least involves some translational processes [1]. From recent neutron scattering data combined with X-ray powder diffraction, Kemner *et. al* were able to determine the position of the ferrocene [2]. It is located just above the line joining two neighboring cations, as shown in Fig 5.2. From additional quasielastic neutron scattering experiments, they conclude a 5-fold jump reorientation of the cyclopentadienyl rings around the symmetry axis of the ferrocene molecule. All these techniques have their own characteristic time scales, with NMR at the slow end (msec) and neutrons (ps) at the fast end of the spectrum. μSR is sensitive for an intermediate time window, and as such could give additional insight on the nature of the dynamics. The information available

from other techniques will allow a comparison. Indications that μSR on such a system is feasible stem from several publications on muon monitored molecular dynamics. Some of these experiments even involved molecular motion in zeolite cages, as will be considered below.

5.2   Studies on dynamics of muonated radicals

For molecular dynamics studies with μSR the muon is used as a spin label. Upon implantation of the muon, muonated free radicals are formed by addition of muonium to isolated conjugated double or triple bonds of organic molecules. Because the muon initiates radical formation, it is an unique tool to study dynamics of these transient short-lived radicals, which are potential intermediates in catalysis. In some cases, the radical differs only slightly from the initial molecule, and thus unless there is a specific chemical interaction due to the unpaired electron, one would expect very similar dynamic behaviour for both.

In order to study the reorientational dynamics of molecules, avoided level crossing μSR (ALC) has been used on a number of occasions. A very illustrative experiment on the potential of ALC was performed on the fullerenes C_{60} and C_{70}, by Roduner and coworkers [3]. The evolution of the resonance lineshapes with temperature is clearly different for both materials (see Fig. 3.6). Supported by Monte Carlo simulations, the lineshapes could be succesfully modeled with two different types of dynamics. For C_{60} a spherical rotional diffusion was obtained, whereas for C_{70} the axis of rotation wobbles over a limited angle.

Similar studies have been performed on surface-adsorbed free cyclohexadienyl radicals. This radical is formed by addition of muonium to benzene: $C_6H_6 + Mu \rightarrow C_6H_6Mu$ Experiments have been with these radicals adsorbed on several different surfaces. The isotopic spectra for cyclohexadienly radicals adsorbed on SiO_2 were explained by translational diffusion around the 7 nm grain [4, 5]. Subsequently more extensive experiments have been reported on muonated cyclohexadienyl radicals in NaZSM-5 zeolite, with various loadings of benzene molecules per unit cell [6, 7]. From the ALC lineshape a fast uniaxial rotation about the axis perpendicular to the molecular plane was concluded. Superimposed on this a two-site jump motion between two orientations was deduced. The high reorientational mobility suggest that the radicals occupy sites at the channel intersections forming the zeolite structure.

Reviewing the above results, and projecting those on the ferrocene in KY zeolite system under study here, one can recognize a few similarities. First of all, the experiments on molecules in zeolites have been performed successfully. The zeolite environment did not obscure detection of the molecular dynamics. Thus assuming that a muonated cyclopentadienyl radical is formed for ferrocene in KY, one might expect to observe a related signal.

Next, benzene and the cyclopentadienyl ring are both aromatic compounds with a very similar planar shape. NMR and neutron scattering on ferrocene in KY, indicate rapid rotation of the ferrocene rings about the 5-fold axis. A similar fast uniaxial rotation about the axis perpendicular to the molecular plane is observed for benzene. This uniaxial rotation results in a very typical asymmetric line shape as is illustrated in Fig. 3.6. Such a typical ALC line shape could be expected for uniaxial rotation of the ferrocene molecule as well.

Finally the orientational randomization observed with NMR and Mössbauer, could

be due to several types of motion. The ferrocene molecular axis might jump between tetrahedral orientations interconnecting the K^+ cations, see Fig 5.2. On the other hand, the interaction with the cations might be weak, which could result in a more isotropic rotational diffusion. This situation is very similar to the μSR experiments on C_{60} and C_{70}, for which one was able to distinguish the different types of motion from the development of the line shape with increasing temperature. Tregenna-Piggott *et al.* have published a large number of spectral simulations for various types of stochastic motion [8]. Among those is the isotropic rotational diffusion, but also reorientational jumps about a tetrahedral angle. If the motion of the molecule fits the right time scale, examination of the line shape could give valuable information on the geometry of the molecular dynamics.

After considering the similarities with *e.g.* encapsulated benzene, one has to recognize the differences of ferrocene in KY zeolite as well. The most obvious distinction is the iron atom incorporated in the molecule. So far investigations have concentrated on simple molecules of high symmetry, such as benzene and fullerenes. This limits the number of muonated radical species and reduces the complexity. The central iron atom in ferrocene decreases the molecular symmetry and results in a possibility for multiple inequivalent sites for muonium addition. Furthermore the metallic center will influence the electronic properties of the cyclopentadienyl rings. These differences will prove to have a profound effect on the μSR data and interpretation.

Recently, Jayasooriya and coworker reported on longitudinal field μSR on organometallic compounds [9]. These materials compose of a single metal atom surrounded by tricarbonyl and cyclohexadienyl ligands. Interest in these materials stems from catalytic properties and the influence of ring dynamics on the stereometry of the polymers formed. The ring dynamics fall within the 10^{-7} to 10^{-9} s time window, which is accessible for μSR. These LF-μSR measurements already indicate multiple radical species. Arrhenius plots of the reorientation rates give activation energies which are in good agreement with QENS data. Additional work was done on the classic metallocene compound ferrocene [10]. The common interest in muonated ferrocene radicals, has led to a productive collaboration which enabled comparison of polycrystalline ferrocene and ferrocene in KY zeolite. The experimental results and discussion on both compounds are described in the next sections.

5.3   Sample preparation

The samples were made at the Schuit Institute of Catalysis, at the Eindhoven University of Technology, where a variety of equipment for sample preparation is available. The synthetic faujasite type zeolite NaY was obtained from Akzo Nobel Chemicals. The sodium ions were replaced by potassium through ion-exchange. The unit cell composition for the resulting zeolite in dehydrated notation is $K_{55}(AlO_2)_{55}(SiO_2)_{137}$. Dehydration was carried out by a staged and gradual heating to 723 K under a dynamic vacuum, as is described by Overweg [11]. Ampoules of dehydrated sample material were flame-sealed under vacuum and stored until use. The vapor phase insertion of $Fe(C_5H_5)_2$ in the KY zeolite was done under nitrogen atmosphere in a glovebox. Dehydrated zeolite powder and freshly sublimed $Fe(C_5H_5)_2$ were combined quantitatively in a mortar mixed by crushing and vacuum sealed at 373 K. When exposed to air, the ferrocene in the zeolite cages oxidizes into ferricinium, this is in contrast to crystalline ferrocene, which is air stable. For this reason the ferrocene in KY zeolite sample was measured and stored under inert

gas or in vacuum.

5.4   Experimental

MuSR experiments on both crystalline ferrocene and ferrocene in KY zeolite, have been performed at muon facilities at ISIS and PSI. They can be divided into high and low magnetic fields. High field measurements were performed on the ALC spectrometer at PSI. For these experiments the time integrated set-up was used. In these measurements time evolution of the muon polarization is lost, and is exchanged for a higher counting rate. This high counting rate enables field scans over a 0.1-5.0 T field range with field steps of about 0.01 T within a reasonable time. The ALC spectrometer is located at the πE3 area. The muons on this beamline are produced in flight, which makes the polarization of the muon beam sensitive to the position of the beam on the production target. During a field scan, this position can abruptly change, and to overcome this problem the field scans were subdivided into overlapping scans.

Samples were mounted under glove-box conditions in a copper sample holder consisting of a 5 mm deep sample space and a kapton window closed with an indium air-tight seal. Since the beamspot is relatively large at this beamline, the sample needs to cover an area with a 55 mm diameter. Measurements have been done on crystalline ferrocene and ferrocene in KY zeolite. Furthermore, ALC spectra were taken for KY zeolite at various temperatures, in order to separate effects due to the zeolite.

Time differential relaxation data were taken at both the EMU and MuSR spectrometer at ISIS. An aluminium sample holder was used with a 35 mm diameter, a similar kapton window and a silver plate to mask the uncovered aluminium. Measurements were done on about 5 g of crystalline ferrocene, KY zeolite and ferrocene in KY zeolite. In order to compare both compounds, similar experiments will be presented successively.

5.5   Experimental results
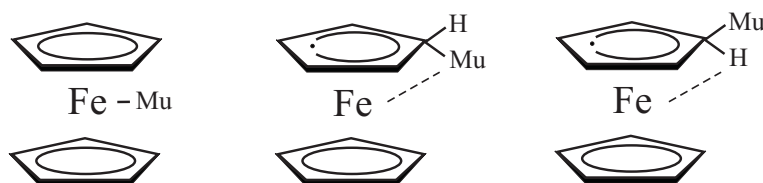
Figure 5.3: *The muonium can add to the ferrocene in three different ways. Two adducts with muonium bonded to the cyclopentadienyl ring and one with muonium bonded to the iron atom.*

As was mentioned above, the reduced symmetry of ferrocene, compared to molecules such as benzene, allows for the formation of multiple radical species. For ferrocene this leaves three possible modes of muonium addition: Two adducts with muonium bonded to the cyclopentadienyl ring and one with muonium bonded to the iron. These radicals are needed to rationalize the data presented. The similar bonding of two cyclopentadienyl adducts, could obscure a separated observation. The data will first be presented

with assignments to the appropriate radicals, and this will be followed by the theoretical treatments that justify these assignments.

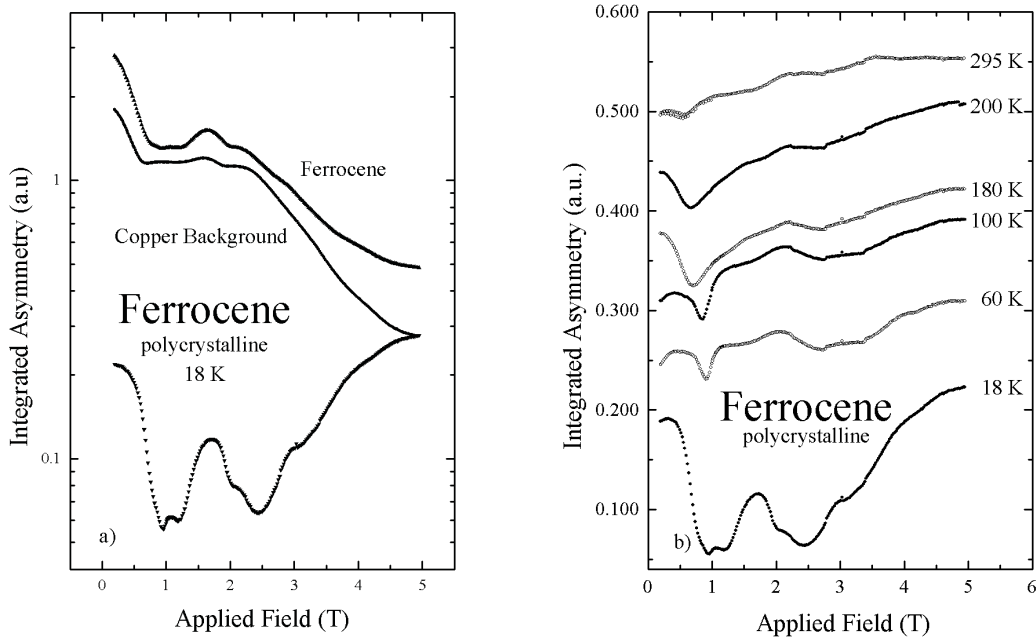### 5.5.1   Time-integrated ALC results

Figure 5.4: *Time integrated ALC measurements on polycrystalline ferrocene. Raw ALC spectra of both ferrocene and a copper background are shown (a) together with a corrected spectrum. Spectra at several temperatures are shown in (b). Measurements have been performed by G.M. Aston and G.A. Hopkins.*

Just like other μSR techniques, ALC-μSR monitors the muon polarization via the asymmetric distribution of emitted decay positrons over the forward and backward detectors. In contrast to ordinary μSR relaxation, avoided level crossings can be observed over a range from a few mT up to several Teslas. Because both muons and the emitted positrons are positively charged particles, their trajectory will be influenced by the applied field. For this reason the measured asymmetry will become field dependent even in the absence of a sample. To overcome this experimental problem, background measurements are subtracted from the raw data. The procedure to obtain a clean ALC spectrum is indicated in Fig. 5.4a. The upper spectra illustrates the field dependence of the asymmetry for both polycrystalline ferrocene and the brass sample holder at 18 K. One clearly observes a decreasing tendency for the asymmetry for both spectra, due to spectrometer properties. After this subtraction, the lower corrected ALC spectrum is obtained, and from now on these will be referred to as ALC spectra. Notice that the vertical axis is in log scale, and the effect of an ALC is relatively small.

From the spectrum at 18 K, one can distinguish two features each composed of two and three overlapping peaks, respectively. The peaks are located at 0.99, 1.2, 2.0, 2.50
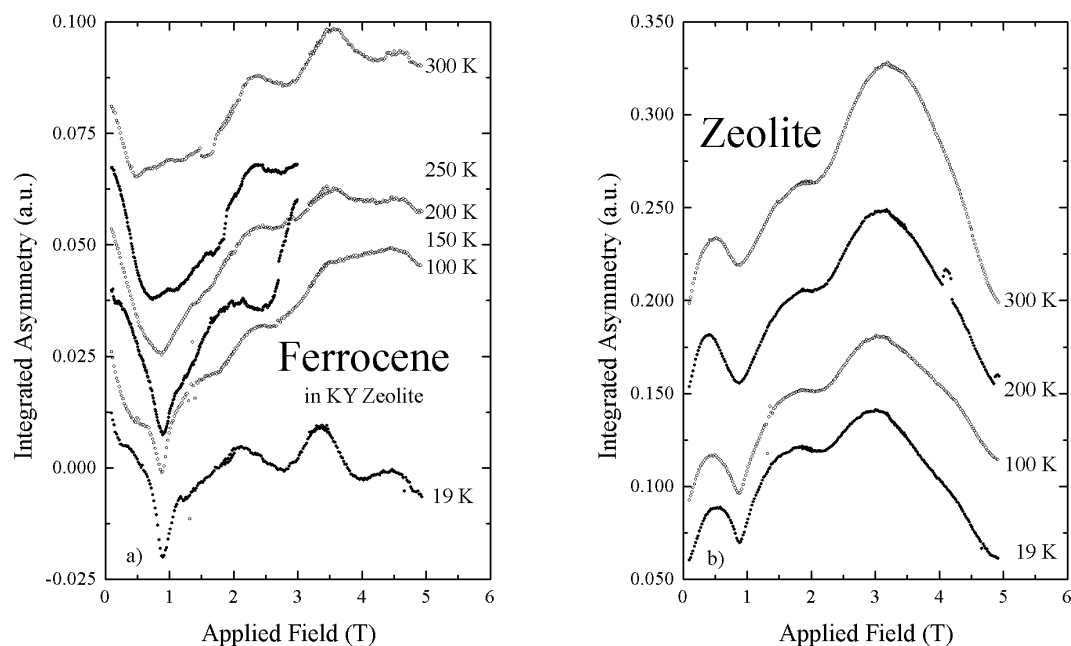
Figure 5.5: *Time integrated ALC spectra for both ferrocene in KY zeolite (a) and for pure KY zeolite (b). The pure KY zeolite raw spectra were used as background correction for the ferrocene in zeolite spectra.*

and 3.15 T respectively. Fig. 5.4b shows similar spectra for ferrocene over a range of temperatures. With increasing temperature four out of five ALC's seem to disappear either by broadening or loss in intensity. The fifth relatively narrow ALC starting at 0.99 T, however remains. At higher temperatures it broadens slightly and seems also to lose intensity. Furthermore, it should be noticed that the peak position moves towards 0.57 T with increasing temperature. Its anomalous behaviour compared to the other peaks, suggests that the process causing it might fall into another category and/or it could be due to a muon adduct to a different site within the ferrocene. For the moment the ALC peaks will be assigned to muon adducts to the cyclopentadienyl ring and metal atom, for the disappearing and remaining peaks, respectively. In the discussion, we will go into more details.

As for polycrystalline ferrocene, the ferrocene in KY zeolite raw spectra need to be corrected for background. In this case however, one is only interested in the properties of ferrocene in the zeolite cage, and less in the background signal of possible muon sites elsewhere in the zeolite. For this reason, both spectrometer properties and background contributions were compensated for by subtracting spectra measured on pure dehydrated KY zeolite. These background spectra, after correction for spectrometer properties with an empty copper sample-holder, turned out to be temperature dependent. Therefore spectra were recorded at temperatures corresponding to the ferrocene in KY sample. Both ALC spectra for ferrocene in KY zeolite and pure KY zeolite for selected temperatures are shown in Fig.5.5a and b, respectively. Again, as was observed in Fecp$_2$, multiple peaks are observed in the low temperature spectra of ferrocene in KY zeolite. However,

the number of peaks is less obvious from the spectra, probably due to broadening or increased overlap. Furthermore, although the spectra seem to be of poorer quality and exhibit a less consistent dependence on temperature, the peaks at high fields seem to persist up to room temperature. This is probably due to some anisotropy, which is not averaged out by thermally excited molecular motion.

More striking however, is the ALC peak at low field. Compared to Fecp$_2$ data it is much more dominant, supporting the assumption of a different muon adduct. With increasing temperature the peak broadens. A closer look at the spectra, suggests that this behaviour could be ascribed to another peak at the side of the peak assigned to the metal-adduct (possibility of this being due to the zeolite host itself cannot be ruled out) moving towards higher fields and broadening, a behaviour similar to those of the ring adduct peaks of pure ferrocene.

A closer look at the pure zeolite spectra fixes the attention on a peak at approximately the same position as the metal adduct. This could suggest that if the zeolite data were not properly scaled, zeolite related effects could still enter the ferrocene in KY spectra. To counter this argument, it should be noted that asymmetry is not a quantity proportional to measuring time or muon flux, but is defined as a relative difference between count(rates) of forward and backward detectors. The fact that an increased number of muon sites in the ferrocene KY sample dilutes the KY zeolite muon site contribution, however remains.

Summarizing, it can be said that for both polycrystalline ferrocene and ferrocene in KY zeolite, spectra with related peaks have been observed. The broader peaks, for now assigned to a muon ring adduct, fade with increasing temperature in Fecp$_2$ which suggest a motional averaging of an anisotropic interaction. For ferrocene KY, geometrical barriers might hinder this motion, leaving part of the anisotropy intact. Additionally a prominent peak at low field was observed in both samples, which moves towards lower field on increasing temperature only in the case of the pure ferrocene. The sharp peak observed with ferrocene in KY zeolite may be due to incomplete subtraction of the zeolite background. The anomalous ALC is assigned to an adduct to the centered metal atom.

5.5.2 Relaxation versus field data

Time differential or relaxation data have been taken on all samples, for both varying applied magnetic field and over a range of temperatures. Although the most popular method to investigate radical species is transverse field μSR (TF-μSR), this is often restricted to single crystals or systems with sufficient motion to average out anisotropic interactions. Because both asymmetry and relaxation can give valuable information on the number and approximate hyperfine interactions of the muon species involved, LF-μSR offers an alternative way of study. Fig. 5.6a presents both the asymmetry and the relaxation rate λ_Z. Polycrystallie ferrocene data at low field could be fitted satisfactorily with a single exponential contribution. However, above 70 mT a second exponential contribution was needed. This component might also be present at lower field, but its relaxation rate probably exceeds the time resolution of the spectrometer. Although in principle the response on a single muon site would be a superposition of exponential terms, in practice their relaxation rates are dominated by only one of them [12]. Therefore, our observation implies the participation of at least two distinct chemical species. This supports the observation of the metal and ring adduct in the ALC data. In order to distinguish between both contributions in the ferrocene relaxation data, the slow relaxing component will be referred to
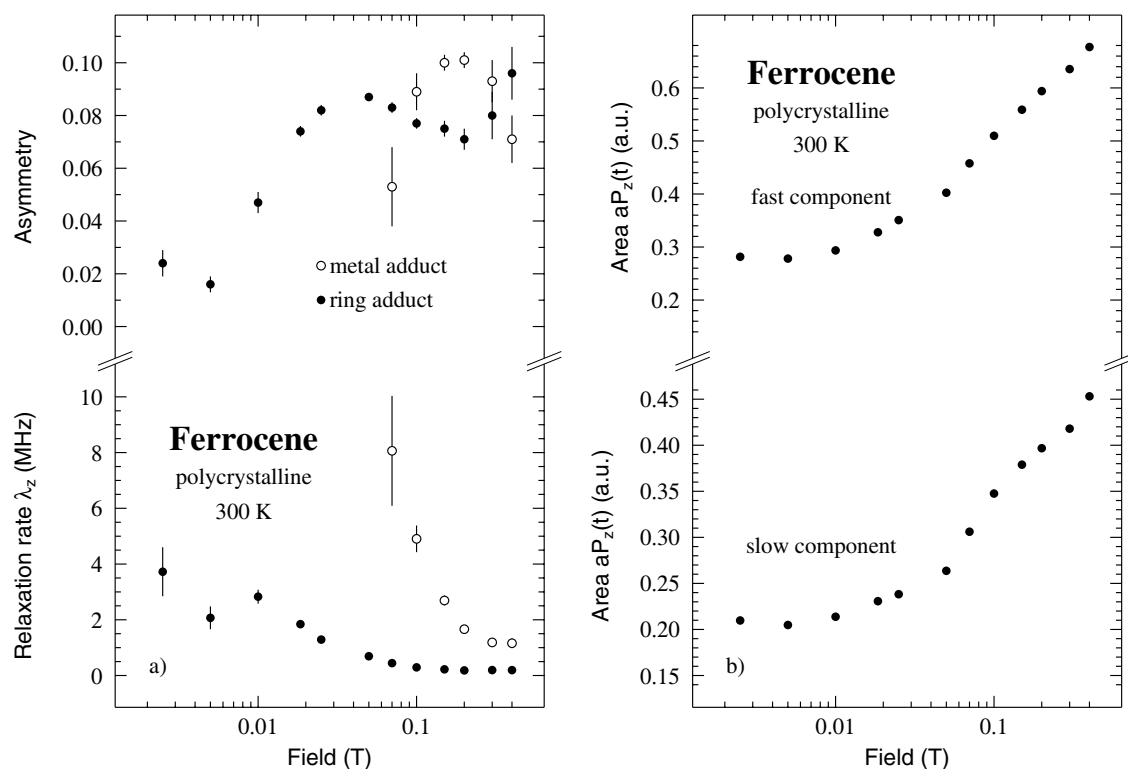
Figure 5.6: *The field dependence of both asymmetry and relaxation rate in polycrystalline ferrocene (a). The data have been analyzed with two exponentials, attributed to a metal and a ring adduct. Integrated asymmetries show an anomaly around 50 mT, which is more pronounced if time of integration is increased(b). This could be related to an ALC peak at low fields.*

Figure 5.7: *The field dependence of the relaxation rate in polycrystalline ferrocene for several temperatures. The lines are guides to the eyes. One can see the maximum relaxation moving towards higher field with increasing temperature.*

as the ring and the fast relaxing component as the metal adduct. These assignments will be justified later in the text. The ring adduct in Fig Fig. 5.6a repolarizes around 18 mT,
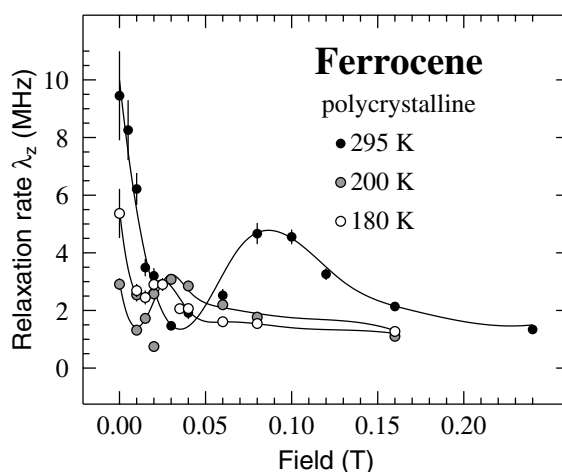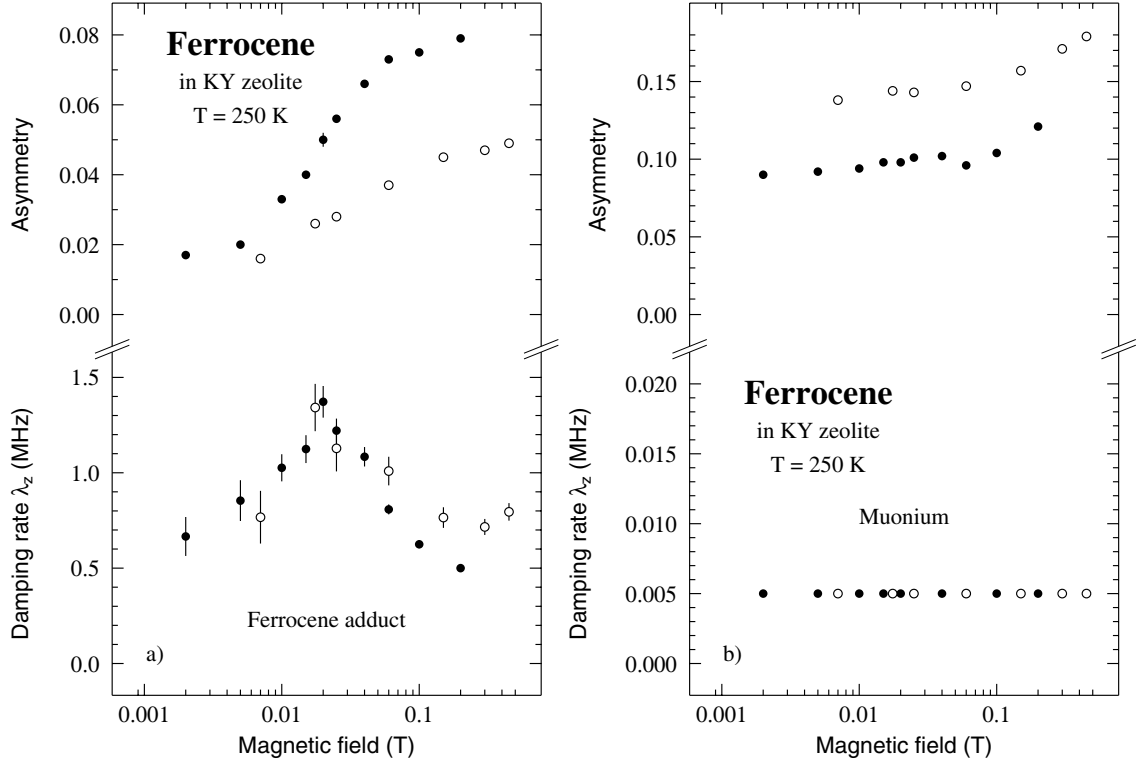
Figure 5.8: *Field dependence of both asymmetry and relaxation rate for ferrocene in KY zeolite at T=250 K. The data have been analyzed with two exponentials. One is attributed to a ferrocene adduct (a), whereas the other is probably due to muonium enclosed in the Y-zeolite (b). The same sample has been measured on two different cycles separated in time, indicated with the open and solid symbols. The general tendencies of the asymmetry are similar but need rescaling, probably due to a loss of ferrocene from the KY-zeolite framework.*

which corresponds well with the repolarization field of muonated benzene [4]. The rapid increase of particularly the metal adduct relaxation rate around 100 mT, could be due to enhanced relaxation at a low field level crossing. The integrated asymmetry, resembling time integrated spectra, was determined and is plotted in Fig. 5.6b. The upper and lower graph labeled slow and fast component, refer to the time of integration, 2.4 and 6.4 μs respectively. Although it is situated right at the slope of the repolarization curve, an anomaly is observed. For long integration times it is more pronounced, and seems to be centered at a field slightly below the maximum relaxation of the metal adduct.

On the other hand, time differential relaxation data taken at several temperatures using the ALC spectrometer at PSI, show a temperature dependence of the relaxation peak, see Fig 5.7. In contrast to the iron adduct ALC presented previously, the relaxation peak moves towards higher fields with increasing temperature.

Relaxation data on ferrocene in zeolite were also fitted with two exponential components, see Fig. 5.8a and b. Data have been collected during two cycles well separated in time. Both are included in Fig. 5.8 indicated with solid and open symbols, respectively. The open symbols refer to the last series. The general tendency of both series are similar. The differences seems to be due to some relative redistribution of muons over both components. This might be due to aging of the sample material, by which part of the

ferrocene has escaped from the zeolite.

In contrast to the $Fecp_2$, the relaxation rate of the dominant component (*i.e.* the component with the larger asymmetry) was very low and shows very little if any temperature dependence. For this reason it has been fixed to an average value during the fitting procedure. This component repolarizes above 100 mT. The limited strength of the magnets prevented full repolarization from being observed. However, a repolarization field above 100 mT is to be expected. This is far higher than values commonly observed for muonated radical species, but is relatively close to the repolarization field of isotropic muonium (150 mT, see section 3.5.2). Formation of muonium in the zeolite structure is not surprising, because apart from the supercages filled with ferrocene molecules, a large number of smaller empty cages is still accessible to muonium. Interaction of these isolated muonium species with the zeolite structure or its cations can not be excluded.

The second component repolarizes at approximately the same value as the ring adduct in the $Fecp_2$. The relatively low asymmetry of this component makes it impossible to subdivide into a ring and metal adduct. This may be an indication that only a ring adduct is formed in the encapsulated state. This observation is supported by temperature scans presented in the next section. The relaxation is roughly peaked around 20 mT. This might be caused by the summation of contributions from both muon species, or an ALC related enhanced relaxation of either one of them. Integrated spectra similar to those made for $Fecp_2$ are frustrated by the large contribution from muonium.
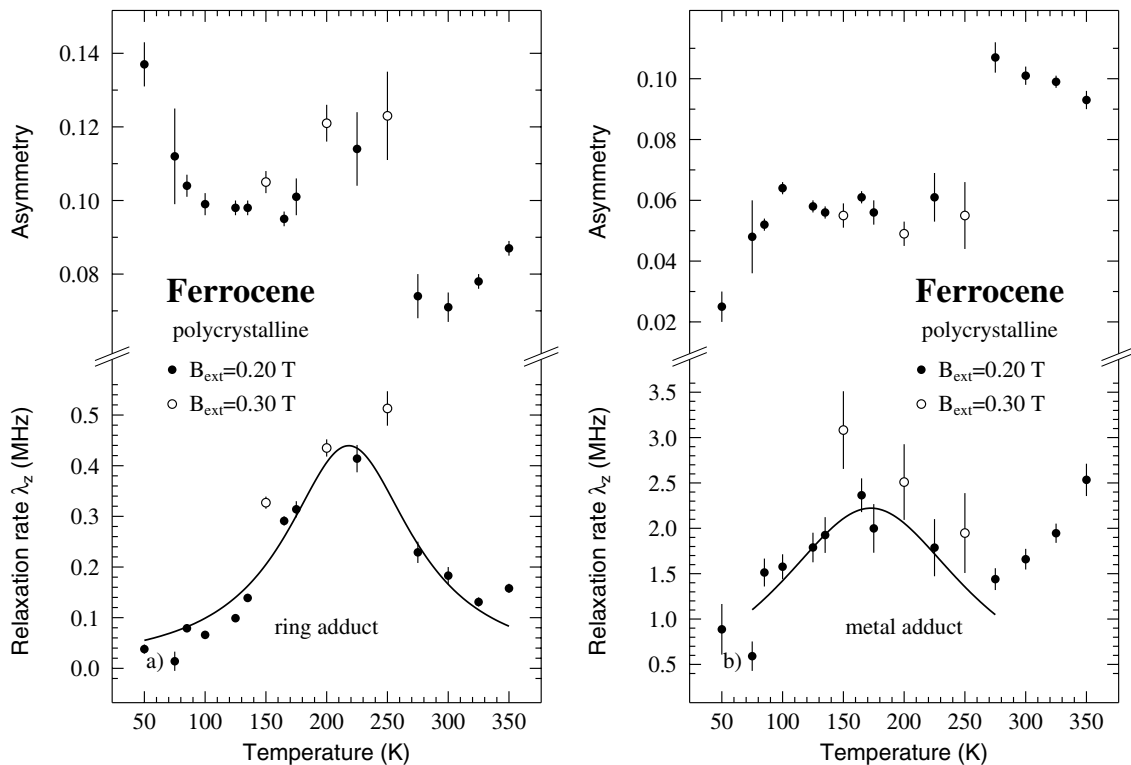

Figure 5.9: *Temperature dependence of both the asymmetry and the relaxation rate in polycrystalline ferrocene in an external field of 0.2 and 0.3 T. Again the data have been analyzed with two contributions. One assigned to a ring adduct (a) and the other other assigned to a metal adduct (b). The solid lines in both figures guide the eyes.*

5.5.3 Relaxation versus temperature data

Information on molecular dynamics is obtainable from a study of the variation of the muon spin relaxation rate with temperature. Reorientations depolarize the muons by causing anisotropic or dipolar terms in the electron-hyperfine interaction to fluctuate. Peaks in the relaxation rate λ_Z (analogous to T_1 minima in NMR) occur when the reorientation rate matches the frequency ω_{ij} of the dominant transition between the coupled muon-electron spin states. Because molecular dynamics can be activated thermally, temperature scans were made for all samples to extract activation energies related to the different relaxing components and compare them with those obtained by other experimental techniques. Fig. 5.9 illustrates the relaxation maxima for both the ring and metal adducts in Fecp$_2$. The relatively high field was used to decouple the muon spin hyperfine fields, resulting in pure Zeeman states. In the corresponding asymmetries a decrease and an increase for the ring and metal adduct respectively is observed around 250 K. The step size is approximately of the same magnitude. This feature could be explained if one assumes a redistribution over both muon sites caused by a change in the chemical potential for either of the two sites.

Results for ferrocene in KY are shown in Fig. 5.10 and 5.11 in 20 mT and 100 mT, respectively. Again the main contribution to the asymmetry is due to muonium. The relaxation of the ferrocene adduct at 20 mT, clearly shows an asymmetric peak. This supports the previous argument that both metal and ring adducts are included in this component. At this field the asymmetry for the muonium contribution seems constant and decreases for the ferrocene adduct with increasing temperature. For 100 mT however, the muonium asymmetry does depend on temperature and the asymmetry of the ferrocene now increases. Because the temperatures ranges are equal and chemical changes are unlikely to depend on magnetic field another explanation is needed here. An explanation could be given by an in-between avoided level crossing. In the previous chapter evidence was presented for an ALC moving with temperature. A more elaborate model for this will be presented in the discussion below. If the applied magnetic fields used here lay on either side of such an ALC, a scan over temperatures moving the ALC would change the observed asymmetries. The observed increase at high and decrease at low magnetic field would imply the ALC to be moving from high towards low field with increasing temperature. This picture is consistent with the ALC observed in the time-integrated ALC data taken at PSI. If Fecp$_2$ would behave similarly, then this behaviour would be in conflict with the field dependence of the ALC related relaxation rate presented in Fig. 5.9.

5.6 Discussion

5.6.1 Discussion on time integrated ALC data

The initial aim of our study was to obtain additional information on the dynamics of ferrocene in the 'supercages' of KY zeolite using several μSR techniques. ALC-μSR has proven to be a very sensitive tool to study radical reorientation dynamics on a critical time scale of the inverse hyperfine anisotropy, which is typically in the order of 50 ns. Tregenna-Piggott *et al.* [8], published a large number of spectral simulations for various types of stochastic motion. Here a few will be introduced which could model the motion of the ferrocene molecule in its cage.
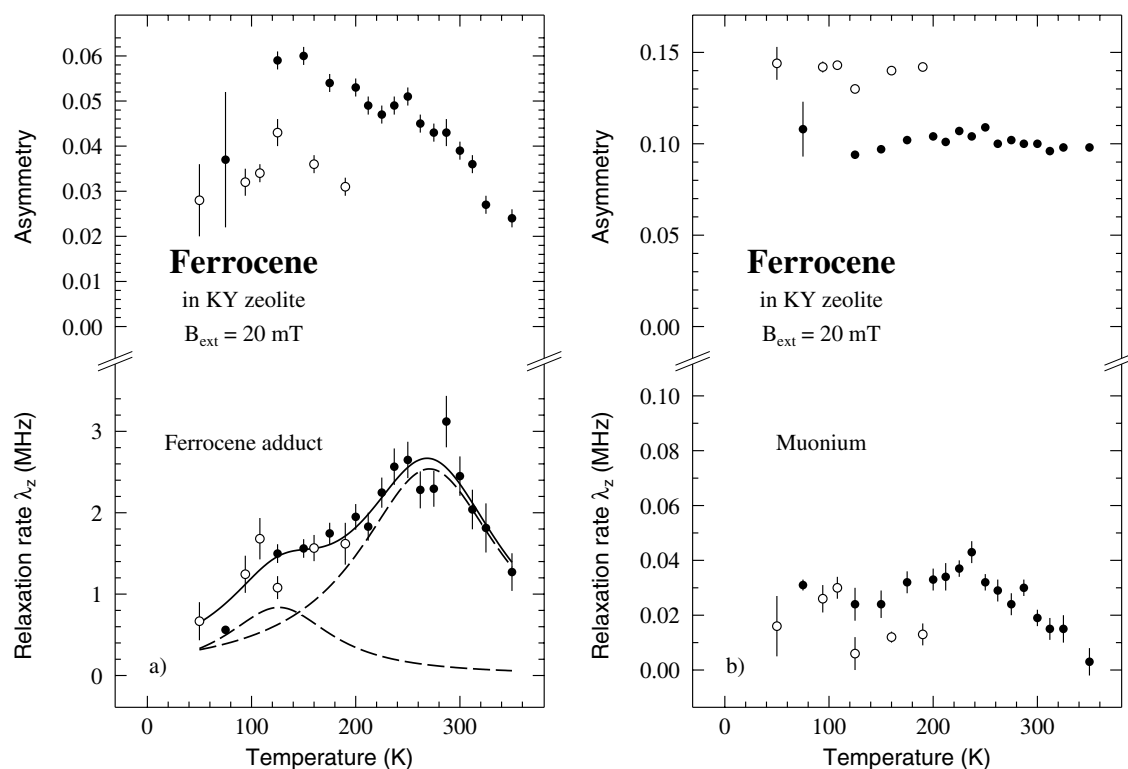
Figure 5.10: *Temperature dependence of both the asymmetry and the relaxation rate for ferrocene in KY zeolite in an external field of 0.02 T. Illustrated are the ferrocene adduct (a), and a contribution due to muonium enclosed in the Y-zeolite (b). The same sample has been measured on two different cycles separated in time, indicated with the open and solid symbols. The general tendencies of the asymmetry are similar but need rescaling, probably due to a loss of ferrocene from the KY-zeolite. The asymmetric peak, marked by the solid line and composed of the two dotted Lorentzians, indicates that relaxation due to both a ring and a metal adduct are included. However, relaxation due to only one component cannot be ruled out based on this figure, because the data below 120 K is limited and scattered.*

The first of all, the random reorientational jump motions, which was successfully used to describe the dynamics of C_{60} [3]. Here the radical is subjected to reorientational jump motions, for which each orientation has the same probability and successive orientations are assumed to be uncorrelated. Secondly, reorientational jumps about a tetrahedral angle. In this case the radical axis will jump between orientations interconnecting the four corners of a tetrahedron. This might well represent the ferrocene dynamics since the encapsulated molecule is surrounded by a tetrahedron of nearest K^+ cations, which are likely to interact with its cyclopentadenyl rings. A similar type of motion referred to as 'preferential orientational motion' wobbles the molecular axis within a finite cone of a preferred orientation. One could imagine this to be a model applicable in case one of the rings is strongly bound to a cation, whereas the other is only restricted in orientation.

All these simulations assume a powder sample and start in the static limit where the time scale of the dynamics is slow compared to the inverse hyperfine anisotropy, resulting in a characteristic asymmetric peak.

Unfortunately the shape of the ALC's observed in both the examined compounds
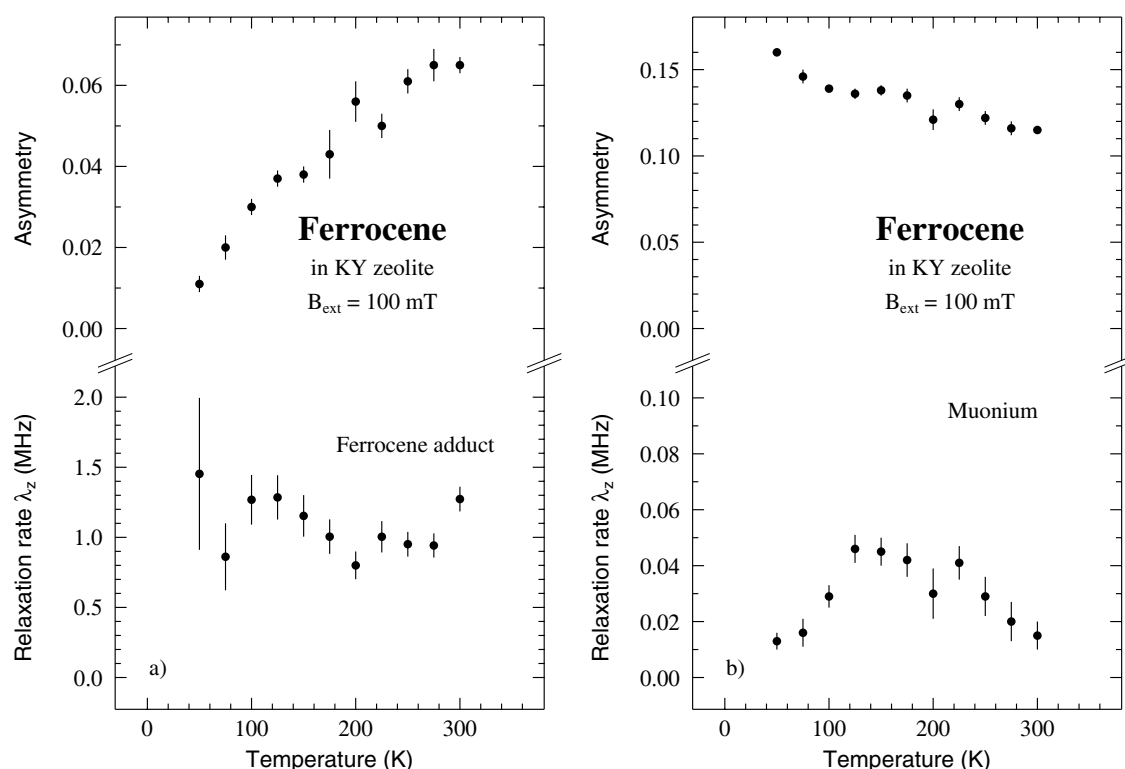
Figure 5.11: *Temperature dependence of both the asymmetry and the relaxation rate for ferrocene in KY zeolite in an external field of 0.1 T. Contributions due to a ferrocene adduct (a) and enclosed muonium (b) are shown.*

lack a characteristic shape. Particularly those assigned to the ring adduct are broad and overlap heavily, and their precise development with temperature is obscured. The metal adduct ALC's in both compounds does show a gradual development with temperature. On the other hand, they do not appear to match either of the simulated spectra. For this reason the ALC line shapes, with our present understanding, can not provide information on the geometry of the reorientational diffusion of the ferrocene in the zeolite.

The thermal development of the ALC spectra shows another interesting feature. For both polycrystalline and zeolite encapsulated ferrocene, the most prominent peak, previously assigned to the metal adduct, moves towards lower fields when temperature is raised. This behaviour suggests a decrease of a main isotropic interaction. Furthermore, low field relaxation data for several temperatures, presented in Fig 5.7, reveal a relaxation peak shifting to lower fields for increased temperatures. In section 3.5.5 it was shown that optima in the relaxation could be related to level crossings. In the next section a model will be presented, which attributes both observations to specific characteristics of the metal adduct.

5.6.2 Spin-orbit coupling for the muon-metal adduct.

The anomalous thermal behaviour of the ALC peak in both compounds and the shift of the relaxation maximum, indicate that these are probably related to an interaction other than those commonly observed in organic compounds. One way to improve agreement
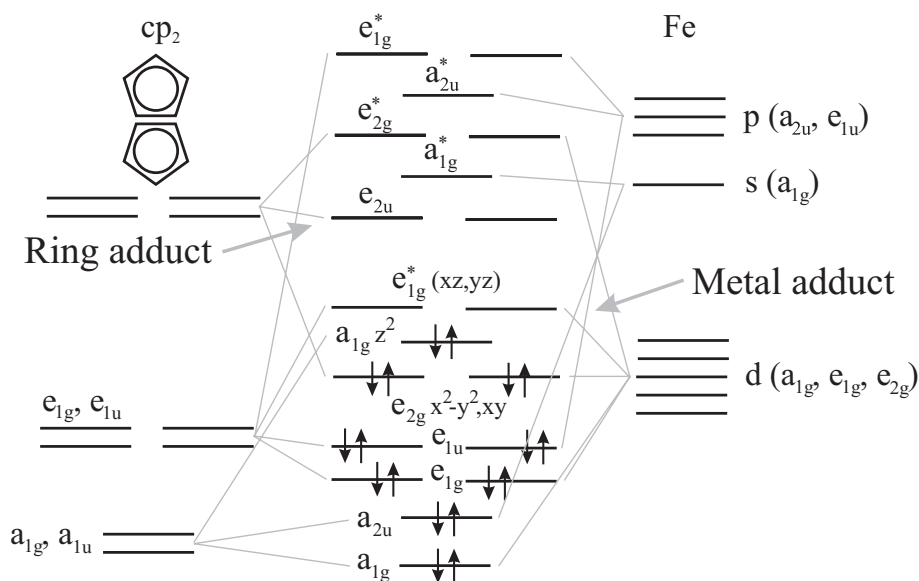
Figure 5.12: *Bonding in ferrocene - approximate molecular orbit (MO) diagram. This diagram was taken from Ref [18]. The ordering of the lowest unoccupied molecular orbital (LUMO) is not clearly established. To explain the differences in activation energy parameters, the unpaired electron is assigned to the non-boding e_{2u} and to the anti-bonding e_{1g} orbitals for the ring and metal adduct, respectively.*

between model and experiment would be by introducing axial anisotropic components to the coupling. However, these would be introduced arbitrarily, without any obvious relation to the physics of the system. It would be preferable if these properties could be related to the presence of the metal atom.

The presence of a muon adduct to the metal allows for some additional interactions. First of all, the spin-orbit coupling. A model including spin-orbit coupling was developed by R. Grinter *et al.* This is presented below and combined with the observations for ferrocene in zeolite.

Spin-orbit interaction gives rise to a splitting of states with muon spin parallel and antiparallel to the effective magnetic moment induced by the orbital motion of the electron. Whenever an electron can occupy a set of degenerate orbitals that permit circulation about the nucleus, this interaction is possible. For example, if an electron can occupy the d_{xz} and d_{yz} orbitals of a metal ion, it will circle the nucleus around the z-axis. The importance of the spin orbit coupling, *e.g.* compared with the Coulomb interaction, is that it increases with the atomic mass. For first row transition metal ions, such as the iron atom in ferrocene, the spin-orbit coupling is applicable, and will be introduced into the Hamiltonian.

Additionally, the anisotropic ligand electron density due to the cyclopentadienyl rings of the ferrocene perturbs the Hamiltonian. This ligand field contribution is taken into account in the molecular orbital diagram shown in Fig. 5.12 [18]. However, addition of the muon to the ferrocene molecule will undoubtedly change the electron density distribution and the symmetry. The precise changes could even depend on whether a ring- or metal-muon adduct is involved *vide infra*. The lowering of symmetry will lift the degeneracy of some of the levels. Whenever a ligand field leaves a level nondegenerate the orbital angular momentum of that state will be quenched. This quenching is brought into the

Hamiltonian by introducing the orbital quenching factor γ. Altogether the magnetic interactions are generated using the Hamiltonian:

$$\hat{\mathcal{H}} = \gamma\varsigma\hat{l}\cdot\hat{S} + A_\mu\hat{I}_\mu\cdot\hat{S} + \left(\frac{1}{2}\gamma\hat{l}_z + \hat{S}_z\right)\nu_e - \hat{I}_{\mu z}\nu_\mu \tag{5.1}$$

Similar to Eq. 3.24, A_μ represents the isotropic hyperfine interaction and $\hat{S}$ and $\hat{I}$ the spin operators for both electron and muon, respectively. In addition ς is the spin-orbit coupling constant, $\hat{l}$ and $\hat{l}_z$ are the operators for the orbital angular momentum of the unpaired electron and its z-component. γ allows for the fact that this electronic orbital angular momentum may be partially quenched; $0 \leq \gamma \leq 1$.

The abundance of interactions constitutes a serious barrier to any interpretation of the data, and requires a number of simplifications and assumptions to be made. First of all it is assumed that the molecular orbital description for metallocenes shown in Fig. 5.12 is applicable. Here the muonium introduces an unpaired electron in a pair of orbitals designated e_{1g}^*. This pair is derived from the $3d$ atomic orbital with m_l values of ± 1. Under conditions of high axial symmetry these can be expected to retain their angular momentum and degeneracy. However, addition of the muon could lift the degeneracy. To allow for this ligand field splitting, off-diagonal elements $\pm iV$, between $m_l=+1$ and -1, are introduced following Ammeter and Swalen [13]. This results in an energy difference between d_{xz} and d_{yz} of 2V.

Although spin-orbit coupling connects microstates with $m_l=0,\pm 1, \pm 2$, only two possible z-components of orbital angular momentum will be considered *i.e.* $m_l=\pm 1$. This assumption is acceptable if the energy difference between the mixing states is large, and can be considered as perturbation.

The remaining 8x8 Hamiltonian matrix including the parameters, A_μ, V, ς and γ, can not be diagonalized algebraically for $B \neq 0$. Extensive numerical attempts to produce an energy level scheme with crossings at 80 and 578 mT, led to the conclusion that the required ALC's could only be found with a very low value for the crystal field splitting V. If this is true, the off-diagonal matrix elements iV can be set to zero, provided that γ is not reduced to zero. The remaining off diagonal terms due to spin-orbit coupling A_μ, connect diagonal terms separated by $\gamma\varsigma$. For the iron atom ς is in the order of 10^7 MHz [14], comparing this with a free-atom muonium $A_\mu=4.5$ GHz, the latter one can be considered as perturbation.

Table 5.1: *Microstates, zero-field energy levels and their gradients. Eigenvectors are given in the basis* $|m_l, m_e, m_\mu\rangle$.

	Microstate	Energy at B=0	Gradient
1	$\left|-1,+\frac{1}{2},+\frac{1}{2}\right\rangle$	$-\frac{1}{2}\gamma\varsigma + \frac{1}{4}A_\mu$	$+\frac{1}{2}B\left[(1-\gamma)\nu_e - \nu_\mu\right]$
2	$\left|+1,-\frac{1}{2},-\frac{1}{2}\right\rangle$	$-\frac{1}{2}\gamma\varsigma + \frac{1}{4}A_\mu$	$-\frac{1}{2}B\left[(1-\gamma)\nu_e - \nu_\mu\right]$
3	$\left|-1,+\frac{1}{2},-\frac{1}{2}\right\rangle$	$-\frac{1}{2}\gamma\varsigma - \frac{1}{4}A_\mu$	$+\frac{1}{2}B\left[(1-\gamma)\nu_e + \nu_\mu\right]$
4	$\left|+1,-\frac{1}{2},+\frac{1}{2}\right\rangle$	$-\frac{1}{2}\gamma\varsigma - \frac{1}{4}A_\mu$	$-\frac{1}{2}B\left[(1-\gamma)\nu_e + \nu_\mu\right]$

With the above arguments, the Hamiltonian, has been reduced to a diagonalized matrix. At zero field the energy levels from 4 degenerate pairs, an upper and a lower set of two pairs at $\pm 1/2\gamma\varsigma$. Unless γ is particularly small, the data can be interpreted by
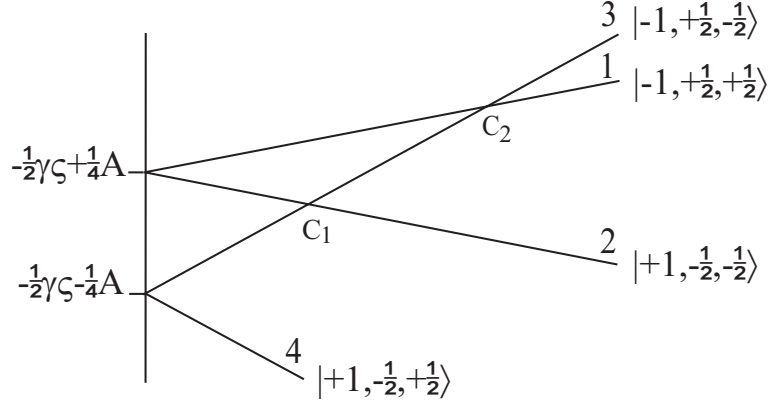
Figure 5.13: *Energy level diagram for the lower four microstates. Two crossings are shown, indicated C_1 and C_2 respectively. The C_1 crossing at lower field is probably a real crossing, with no static term mixing both states. A fluctuating perturbation, however, can induce relaxation as was shown in section 3.5.5. The crossing at C_2, is interpreted as the one observed in the ALC spectra. The static interaction mixing both states could be of dipolar origin.*

Table 5.2: *Development of the isotropic hyperfine interaction A_μ and γ with temperature, for both polycrystalline ferrocene and ferrocene in KY zeolite. These two parameters have been obtained from the shift of the metal adduct relaxation peak B_{C1} shown in Fig 5.7 and ALC peak position B_{C2} in Fig 5.4 and 5.5.*

	T (K)	B_{C1} (mT)	B_{C2} (mT)	γ	A_μ (MHz)
Ferrocene	166	10	995	0.52	270
	180	20	675	0.84	183
	200	30	629	0.90	171
	295	80	578	0.97	157
Ferrocene in	150	-	917	-	248
KY zeolite	200	-	844	-	228
	250	20	697	0.83	189
	300	-	459	-	124

only the lower group of four energy levels. The positions of the avoided level crossings (ALC) can now be estimated by the zero field energy levels and their gradients. Both of these values for the different microstates are given in Table 5.1. In Fig. 5.13 the related crossing diagram is shown. The value for γ was taken such that $|(1 - \gamma)\nu_e| > |\nu_\mu|$.

From both the zero field values and the gradients, the positions of the crossings can now be calculated. For the intersection of the energy level 2 and 3, indicated as C_1, one finds $A_\mu = 2B_{C1}(1 - \gamma)\nu_e$. The second crossing between 1 and 3, C_2, is positioned at $A_\mu = -2B_{C2}\nu_\mu$. The crossing at low fields, is linked to the relaxation peak moving with temperature presented in Fig 5.7. This suggests that it is a real crossing with the relaxation induced by some fluctuating perturbation. The crossing C_2, however, is an ALC, and attributed to the metal ALC observed in time integrated spectra for both
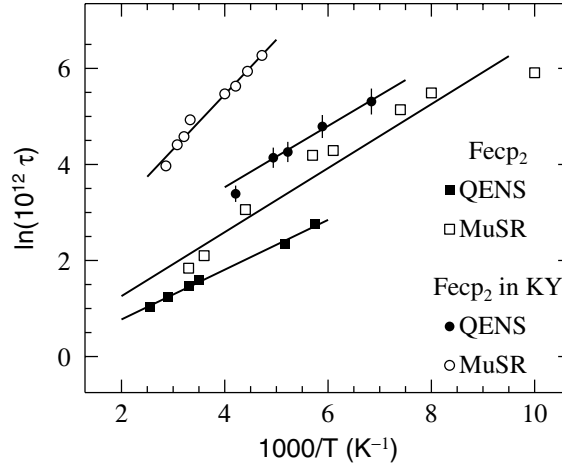
Figure 5.14: *Arrhenius plots for polycrystalline ferrocene and ferrocene in KY zeolite, for both QENS and MuSR. MuSR data represent the muon-ring adduct. The solid lines are fits with Arrhenius law. The deduced parameters are given in Table 5.3.*

compounds. The position of both the experimental relaxation peak and the metal ALC for several temperatures, are listed in Table. 5.2 as B_{C1} and B_{C2} respectively. The resulting orbital quenching factor γ and hyperfine interaction A_μ accompany them.

It is noted that, at higher temperatures, the value of γ is close to one. This indicates that the orbital angular momentum is largely unquenched, and even at 166 K the value of $\gamma\varsigma$ would still be of the order of 10^6 MHz. This is quite consistent with our earlier conclusion that the crystal field splitting, V, is small. Any lifting of the $m_l = \pm 1$ degeneracy would be expected to have a strongly quenching effect on the associated angular momentum. It also justifies the assumption made above that γ was not so small as to reduce $\gamma\varsigma$ to a value smaller than $|V|$. Clearly, these assumptions may be less appropriate at lower temperatures.

5.6.3 Time differential relaxation data

Both the metal and the ring adduct are incorporated into the ferrocene molecule. Consequently, the adduct will participate in all the molecular librations, vibrations and rotations. Since the muon adduct is relatively light and small compared to the whole molecule, it will hardly influence the molecules moment of inertia. Therefore one expects it to give a negligible perturbation to the dynamics the whole molecule. As was previously introduced in section 3.5.5, the relaxation rate λ_z of the muon spin is given by:

$$\lambda_z = \frac{|M_{ij}|^2 \tau_c}{1 + \tau_c^2 \omega_{ij}^2} \tag{5.2}$$

Since the motional correlation time τ in the system can be thermally activated, λ_z itself depends on temperature. The observed maximum of λ_z corresponds to a T_1 minimum in NMR, where a dominant transition frequency ω_{ij} is matched by a motional process ($\tau_c \omega_{ij} = 1$) and the relaxation mechanism finds its maximal efficiency. The temperature dependences for both compounds were introduced by Fig. 5.9,5.10 and 5.11. From those

motional correlation times τ_c have been extracted via their connection with λ:

$$\tau = \frac{\lambda_{max} \pm \sqrt{\lambda_{max}^2 - \lambda^2}}{\omega_{ij}\lambda} \quad \begin{cases} T \leq T_{max} : + \\ T \geq T_{max} : - \end{cases} \tag{5.3}$$

In this formula the temperature, corresponding to the maximum relaxation λ_{max}, divides the correlation time τ_c in a slow and fast regime compared to the transition frequency ω_{ij}. This transition frequency depends on the energy levels determined by the static Hamiltonian and the character of the induced perturbation, either isotropic or anisotropic. For our purpose we have used the $\langle 2| \leftrightarrow |4\rangle$ transition induced by an isotropic perturbation of the isotropic hyperfine coupling. Combining this with the expressions in Table 3.1, one finds $\omega_{ij} = 2\pi A_\mu \sqrt{1 + (\nu_e + \nu_\mu)^2/A_\mu^2}$. Because the repolarisation curve of the ring adduct in polycrystalline ferrocene resembles that of benzene, and also the ring structures are very similar, the static hyperfine interaction, A_μ was taken 514.6 MHz similar to that observed for benzene [4]. Obviously this similarity does not apply for the metal adduct. This hinders a proper determination of τ. The thermal activation of the molecular dynamics and its related correlation time τ can be written as an Arrhenius law:

$$\tau_c = \tau_\infty \exp \frac{E_a}{k_B T} \tag{5.4}$$

In Fig. 5.14 the correlation time versus temperature for the ring adducts in both polycrystalline ferrocene and ferrocene in zeolite are shown. These are accompanied with QENS data by Gardner *et al.* [16] and Kemner *et al.* [17], respectively.

The derived activation energy E_a and attempt times τ_∞ are given in Table 5.3 for several techniques and muon adducts. The activation parameters for the ring adduct in polycrystalline ferrocene are in close agreement with those from literature, and is clear evidence that the same type of dynamic process is measured in all the techniques. With QENS this was assigned to the rotation of the ferrocene rings. This confirms that the adduct is to be assigned to the ring. The activation energy for the metal adduct is smaller by approximately a factor of two. Additionally, activation energy of the ring adduct of ferrocene is higher than that from QENS on the same compound.

Assuming the underlying dynamic process for both adducts to be the same, these peculiarities of the MuSR data need explanation. For this a closer look to the molecular orbital diagram for ferrocene given in Fig. 5.12 is useful [18]. It should be noted that although this MO diagram is qualitatively generally accepted, the details in the MO diagram such as the energetic separation or even the sequence of the molecular orbitals can vary depending on the quantum-mechanical method used. Addition of muonium introduces an unpaired electron in the lowest unoccupied molecular orbital (LUMO). If such an addition would have negligible influence, this electron would be accommodated in the e_{1g}^* level. Obviously the muon will perturb the system and will lower the symmetry of the molecule to C_s. Although it is hard to tell how this will effect the MO diagram quantitatively, it will lift the degeneracy of some of the levels and could even invert some of the levels. Any detailed information on this could only be found by computer simulation such as density function theory (DFT), which is out of the scope of this thesis. In order to explain the data qualitatively, we consider the order of the lowest two unoccupied MO e_{1g}^* and e_{2u}, to depend on the muon addition site within the ferrocene.

For the polycrystalline ferrocene, E_a matches the corresponding values for NMR and QENS very well. This would suggest that the addition of the muon does not perturb the

Table 5.3: *Parameters of Arrhenius law fits for a number of different experimental techniques. Presented are activation energy E_a and pre-exponential factor τ_∞ for both polycrystalline ferrocene and ferrocene in KY zeolite. MuSR results are assigned to their corresponding muon adduct.*

	E_a kJmol^{-1}	τ_∞ ps	adduct
Ferrocene:			
NMR[15]	5.4 (5)	3.2	
QENS[16]	4.4 (5)	0.8	
MuSR[10] 200 mT	2.3	4.5	metal
	5.4	1.0	ring
Ferrocene in KY zeolite			
QENS[17]	5.96	1.63	
MuSR 20 mT	3.3 (3)	11 (3)	metal
	9.7 (7)	2.2 (7)	ring
100 mT	2.0(6)	6.6(7)	metal
KY zeolite	12(1)	0.8(5)	muonium

bonding between the rings and the metal atom. Looking at the MO diagram, this could be explained if the unpaired electron introduced by the muon-ring adduct occupies the non-bonding e_{2u} level within the rings. In contrast the metal-adduct puts its electron in the anti-bonding e_{1g}^*, resulting in a reduced activation energy for ring rotation.

Although this explains the difference between both muon adducts, it can not explain the difference between QENS and MuSR for the ring adduct in ferrocene in KY zeolite. Neutron and X-ray diffraction, on this compound have shown that the ferrocene molecule is positioned in between two K$^+$ cations [2]. The metal atom is directed towards the center of the super cage, and the rings interact with the K$^+$ cations, see Fig 5.2. For ferrocene this does not hinder the ring rotation very much. However, for the muonated radical the electronic properties will have been changed as discussed above, and this could influence the bonding of the rings to the cations. Similar experiments on benzene in NaY zeolite, have shown a difference between hyperfine couplings for both muon and proton of the CHMu methylene group in its two different orientations [19]. The muon is either on the opposite side of the benzene ring from the cation, or on the same side. These results suggest a non-planar equilibrium geometry due to strong interaction of the π electron density with the Na cation. *Ab initio* molecular orbital methods confirm these differences between the orientations [20]. A similar picture might apply to the ring adduct for the ferrocene in zeolite. A stronger interaction with the cations will hinder rotations of the ring, and increase the activation energy. The dynamics of the ring for the iron adduct, however, do not seem to be influenced.

5.7   Conclusions

The ALC spectra observed were rather broad and did not show any temperature dependence corresponding with the simulated spectra for several plausible dynamical processes. This excluded a direct proof of on the specific characteristic geometry of the molecular motion in the KY zeolite supercage.

In fact the ALC spectra were rather complex with a series of ALC peaks. The shifting of the peak position, however, could successfully be described by a model including a spin-orbit coupling interaction for the metal adduct. Although a number of assumptions were needed in order to reduce the complexity of the problem, the trend of the obtained orbital quenching factor γ agrees with an increase of the local symmetry due to rotation of the ferrocene rings.

From MuSR relaxation experiments activation parameters have been obtained, which for the ring adduct in polycrystalline ferrocene corresponds well with those obtained by other techniques. Although the moment of inertia is hardly changed by addition of the muon, the effects of addition on the electronic properties is far more important. The differences in activation energies for the two radical species give a good indication for this influence. Postulated differences in lowest unoccupied molecular orbital, based on a well established energy level diagram, have been used to rationalize these observations. Furthermore, the interaction with the zeolite cage seems to be enhanced by muon addition.

Bibliography

[1] A.R. Overweg, H. Koller, J.W. de Haan, L.J.M. van de Ven, A.M. van der Kraan and R.A. van Santen, J. Phys. Chem. B **103** (1999) 4298

[2] E. Kemner, A.,R. Overweg, L. van Eijck, A.N. Fitch, E. Suard, I.M. de Schepper and G.J. Kearley, submitted

[3] E. Roduner, KJ. Prassides, R.M. Macrae, I.M. Thomas, C. Niedermayer, U. Binninger, C. Bernhard, A. Hofer and I.D. Reid, Chem. Phys. **192** (1995) 231

[4] I.D. Reid, T. Azuma and E. Roduner, Nature **345** (1990) 328

[5] E. Roduner, Hyperfine Interact. **65** (1990) 857

[6] M. Stolmár, E. Roduner, H. Dilger, U. Himmer, M Shelley and I.D. Reid, Hyperfine Interact. **106** (1997) 51

[7] E. Roduner, M Stolmár, H. Dilger and I.D. Reid, J. Phys. Chem. A **102** (1998) 7591

[8] P.L.W. Tregenna-Piggott, E. Roduner and S. Santos, Chem. Phys. **203** (1996) 317

[9] U.A. Jayasooriya, J.A. Stride, G.M. Aston, G.A. Hopkins, S.F.J. Cox, S.P. Cottrel and C.A. Scott, Hyperfine Interact. **106** (1997) 27

[10] U.A. Jayasooriya, G.M. Aston and J.A. Stride, Appl. Magn. Reson. **13** (1997) 165

[11] A.R. Overweg, *The Preparation, Modification and Characterization of some Molecular sieve materials*, thesis 1998, Eindhoven University of Technology

[12] S.F.J. Cox and D.S. Sivia, Hyperfine Interact. **87** (1994) 971

[13] J.H. Ammeter and J.D. Swalen, J. Chem. Phys. **72** (1997) 678

[14] J.S. Griffith, *The theory of the transition metal ions*, Cambridge University Press 1971

[15] A. Kubo, R. Ikeda and D. Nakamura, J. Chem. Soc. Farad. Trans. **82** (1986) 1543

[16] A.B. Gardner, J. Howard and T.C. Waddington, Chem. Phys. **57** (1981) 453

[17] E. Kemner, I.M de Schepper, A.J.M. Schmets, H. Grimm, A.R. Overweg and R.A. van Santen, J. Phys. Chem. B **104** (2000) 1560

[18] N. Fey, J. Chem. Techno. Biotechnol **74** (1999) 852

[19] D.G. Fleming, M. Shelley, D.J. Arseneau, M. Senba, J.J. Pan, S.R. Kreitzman and E. Roduner, Physica B **289-290** (2000) 603

[20] B. Webster and R.M. Macrae, Physica B **289-290** (2000) 598 (1995) 222

Chapter 6

μSR on monodisperse Pd nano-clusters

Abstract

The interest for mono disperse nano-clusters, stems from the opportunity to study surface and size effects at an intermediate stage between atomic and metallic behaviour. Quantum size theory predicts a small 1 μ_B moment on half of the particles. Susceptibility and specific heat analysis assume a 0.2 T internal field. A μSR study on $Pd_{55}[PPh_3]_{12}O_{30}$ and $Pd_{561}Phen^*_{36}O_{200}$ show a depolarization which could be explained with dipolar moments of $\sim$1 μ_B. The muon data do not give any indication for either an odd/even nor a quantum size effect. The internal 0.2 T field is unlikely to be of dipolar origin and is probably due to a super-exchange interaction via the two ligand shells involved.

6.1   Introduction

The continuous quest for structures of ever smaller size certainly represents one of the most fascinating scientific developments of the last decades. Investigation of nanometer-scale objects such as dots, fullerenes, nanotubes and nano-particles are nowadays at the forefront of material research, thanks to advances in synthesis of artificial structures. The miniaturization of metal particles to the nano-size regime, fits in this line of research. The interest in these materials ranges from favorable catalytic properties, to possible applications in solar cells and information storage media. Another fascinating study these metal nano-particles offer, is the more fundamental question of how atomic characteristics develop into the properties of bulk metal. The clusters are viewed upon as a transition between atomic and bulk, a regime which is commonly referred to as mesoscopic. One of the most appealing features is the correlation between the particle size and electronic behaviour [1]. Although the first theoretical prediction of unusual electronic and magnetic properties due to size effects already appeared in the early sixties [2], convincing evidence for these effects on the thermodynamic properties of the nano-particles was not found until 1996. The main reason for this was the broad particle size distribution of samples available at that time. Size distributions over 10% could not be avoided and completely masked the effects expected. Recent advances in the field of inorganic, coordination and metalorganic chemistry have enabled the production of stoichiometric identical clusters, which are monodisperse, *i.e.* have the same size, in quantities large enough to meet the needs of experimental techniques (10-500 mg). In the next section, these clusters will be introduced, as well as the size effects of interest and the way these have been measured so far. This will at the end, give the objectives of the µSR experiments. The rest of this chapter will be dedicated to the µSR data, the analysis and discussion of the results.

6.2   Magic number clusters

There is a huge number of nano-particles available nowadays, ranging from more or less molecular clusters with one or a few metal atoms up to particles with over a thousand atoms. These bigger particles, usually have a relatively large size distribution and are commonly referred to as 'colloids'. As our interest is mainly in the size and surface effects of clusters with a metallic core, at least a group (cluster) of interconnected metallic atoms is needed, with preferably a well defined number of atoms and shape. Nowadays these clusters can be produced with atom numbers ranging ten to a few hundred. Both colloids and clusters are synthesized in a very similar way: a salt or a complex of the corresponding metal is dissolved in an appropriate solvent and is reduced to the zero valent state. If the metal cations are reduced to metal atoms, they tend to coalesce quickly into larger arrangements resulting in crystalline metallic precipitates. In order to obtain clusters or colloids, ligand molecules are used that strongly coordinate to the atoms at the particle surface and stop the growth [1]. In the case of well defined cluster sizes, another aspect of importance is the preferred formation of "full-shell" clusters. The synthesis of these full-shell clusters is a laborious task which is *e.g.* sensitive to concentration, ligand and geometry.

    The study of surface and size effects has mainly been focused on a special class of these clusters, the "magic number clusters", as synthesized in recent years by G. Schmid
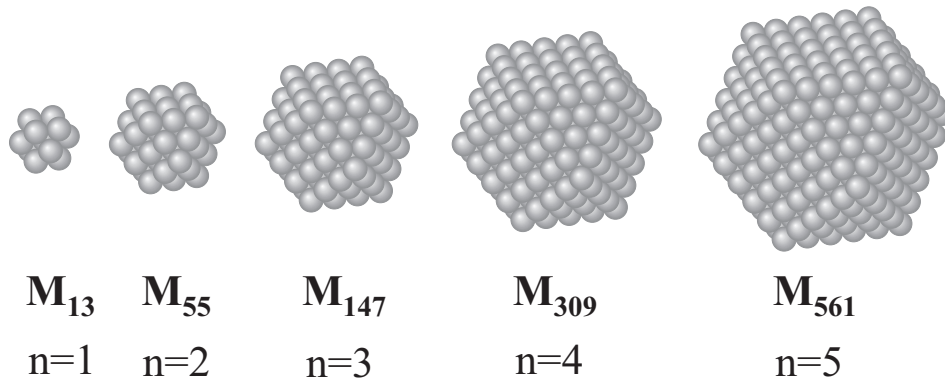
Figure 6.1: *The 'magic number' clusters, obtained be surrounding a single metal atom progressively by shells of atoms of its kind. Here* M_i *indicates the number of atoms, and* n *the number of shells.*

and coworkers [3]. In these clusters the metal cores are composed of a central metal atom, progressively surrounded by a number of successive full shells of atoms of its kind in a *f.c.c.* packing. This results in clusters with 13, 55, 147, 309, 561 *etc.* atoms per particle, referred to as 'magic' numbers, because each corresponds to 1, 2, 3, 4, 5 *etc.* completed shells. The metallic cores of the first few clusters are illustrated in Fig 6.1, together with an indication of the number of metal atoms M and the number of shell n. So far Schmid *et al.* have been able to synthesize series of Pt, Au and Pd clusters of varying sizes, namely Au2, Pt2, Pt4, Pd2, Pd4, Pd5, Pd7 and Pd8, where the number refers to the number of shells. Different ligations are used for the different cluster sizes and metals. Some cluster sizes however can be synthesized with different ligation, giving the opportunity to study the effect of the ligands on the particle properties as well. In the next section a brief outline on surface and size effect studies on these clusters done so far will be given. Additionally a suggestion of the possible complementary information μSR could provide is presented.

6.3 Size and surface effects in magic number clusters

6.3.1 Theory of the Quantum Size Effect

In bulk metal, the energy spectrum of the conduction electrons can be described as a (pseudo) continuum of states around the Fermi energy E_F [4, 5], commonly known as the band model. A single atom, on the other hand, has only discrete electronic levels. This quantization effect is caused by the spatial confinement of the electrons to the atom. A nano-particle is an intermediate between these two extremes. The conduction electrons are assumed to be confined to the particle, again giving rise to a discrete spectrum of energies. However, the distance between the levels is expected to become smaller with increasing particle size. In the bulk limit the thermal energy becomes comparable with the level spacing, which ends up in a band model. The presence of these quantum gaps results in dramatic effects in *e.g.* thermodynamic properties of the nano-particles. The effects associated with the discrete energy levels due to the small particle size are called quantum size effects (QSE).

In practice, even for clusters of the same size, different level spacings will occur, *e.g.*
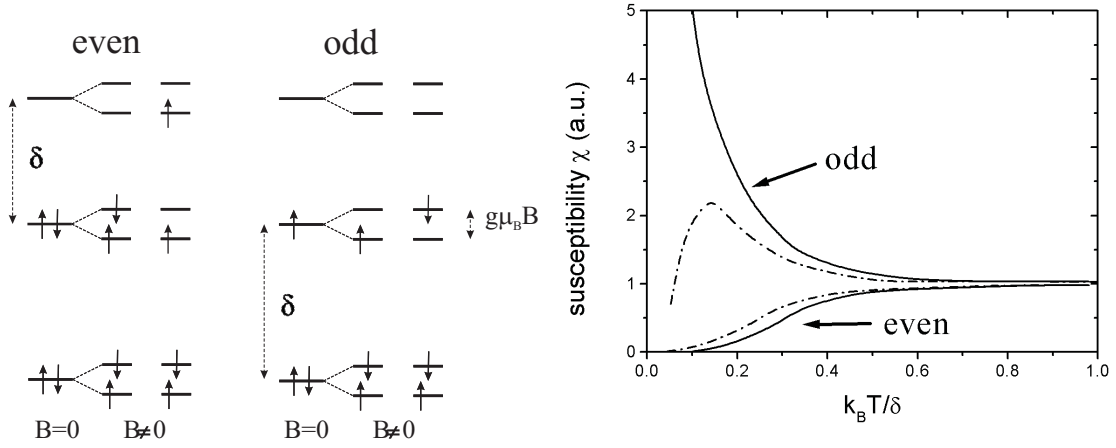
Figure 6.2: *Odd and even behaviour. On the left, energy-level diagrams for odd and even number of electrons are given. The diagrams show degenerate levels, degeneracy lifted by a magnetic field and the first excited state. On the right, the solid line give simulated susceptibility data for both odd and even. The dotted line represents the influence of a $\mu_B B/\delta = 0.1$ internal magnetic field. All energies are normalized with respect to the average energy level spacing δ. For combined odd and even particles samples, a weighed sum of both contributions is needed. The figures have been taken from Ref. [8, 10].*

due to the large surface to volume ratio which makes these levels extremely sensitive to surface imperfections and perturbations. Kubo recognized that measurements on a large number of clusters would reflect the physical properties of an ensemble of particles [2]. Therefore, Kubo proposed a random distribution of energy levels, with an average level spacing δ_{qs} and a probability to find an energy gap. However, the Poisson distribution Kubo used, still leaves a highly degenerate state around E_F. For a better description, perturbations in the order of the level spacing need to be incorporated resulting in a very complex Hamiltonian. To overcome this problem Gor'kov and Eliashberg have introduced a statistical treatment of the levels employing random matrix theory [6]. Random matrix theory is used in nuclear physics to solve similar problems, but is out of the scope of this work. Nevertheless, it needs to be mentioned that symmetry properties of the Hamiltonian influence the distribution function of the levels, lifting degeneracy, and effecting the actual temperature dependence of thermodynamic properties at low temperature.

For a qualitative understanding, however, a simple description with an average level spacing δ_{qs} will be sufficient for our purpose here. An estimate of δ_{qs} can be made by the inverse of the density of states at the Fermi level $\rho(E_F)$ multiplied by two, to correct for spin degeneracy. With $\rho(E_F) = 3N/2E_F$ this results in $\delta_{qs} = 4E_F/3N$ [4]. A better approximation for δ_{qs} is based on the experimental linear coefficient of specific heat of bulk metal γ at low temperatures [7]:

$$\delta_{qs} = \frac{2\pi^2 R}{3} \frac{k_B}{N\gamma} \tag{6.1}$$

with R the gas constant and N the number of atoms. In Table 6.1, the theoretical average level spacings δ_{qs} are given for a series of magic number palladium clusters.

Another important aspect of these small particles is the relatively large energy needed to add or remove an elementary charge from a cluster [2]. The charging energy is propor-

Table 6.1: *Both theoretical values for the average level spacing δ_{qs} according to Eq. 6.1 and corresponding experimental results for susceptibility δ_χ and specific heat δ_{c_v}, for a series of palladium clusters. The number of atoms per cluster is indicated. For calculation of δ_{qs}, $\gamma=9.42$ mJmol^{-1}K^{-2} was taken [4]. Experimental values were taken from Volokitin and Sinzig [7, 8]*

	N_{atoms}	δ_{qs}(K)	δ_χ(K)	δ_{c_v}(K)
Pd2	55	106	-	-
Pd5	561	10	11(2)	12(1)
Pd7	1415	4	5(1)	4.5(1)
Pd8	2057	2.8	1(1)	3.0(2)

tional to the inverse of the cluster size, and for nano-particles exceeds the thermal energy. It suppresses charge fluctuations and keeps the number of electrons per particle strictly fixed, requiring averaging over a canonical ensemble to determine the thermodynamic properties [9].

This gives rise to different behaviour of clusters with an odd or even number of electrons. As illustrated in Fig. 6.2 the low energy excitations $T \ll \delta/k_B$ of a cluster with an odd number of electrons corresponds to a single free spin, giving the usual paramagnetic susceptibility inversely proportional to the temperature, diverging at $T=0$ K. On the other hand, in clusters with an even number of electrons, the spins are paired in the ground state and the first excitation is determined by the level spacing instead of the magnetic splitting energy, resulting in a zero or finite susceptibility at $T=0$ K.

6.3.2 Experimental evidence for QSE

Recently Volokitin *et al.* have presented susceptibility data for a series of Pd magic number clusters, with varying Pd-core sizes [10]. Instead of the common temperature independent Pauli susceptibility, the susceptibility increases sharply at size-dependent onset temperatures, and decreases again if T is lowered further. This paramagnetic behaviour had previously been attributed to impurities present in the starting material. However in their analysis they were able to quantitatively describe their data with a 50/50 mixture of odd and even electron particles. The average level spacing δ_{qs}, which depends on the cluster size, is the only free parameter in this QSE model. On analysis, the values δ_χ proofed to be in excellent agreement with the theoretical estimates for each Pd cluster size. Furthermore, the experimental values for δ both susceptibility δ_χ and similar specific heat experiments δ_{c_v} also agreed well, as is shown in Table 6.1.

The down turn of the susceptibility at low temperatures observed, is attributed to interactions between the spin of neighboring odd-electron particles, which will lift the spin degeneracy of the electron levels, thereby suppressing the susceptibility divergence. In order to describe the maxima within an extended QSE model, an internal field of about 0.2 T was needed as illustrated in Fig. 6.2. The magnetic interaction is assumed to be of dipolar origin, induced by the electron spin on the cluster. In addition a contribution due to super-exchange is possible. In super-exchange magnetic atoms with non-overlapping charge distributions interact because their corresponding wavefunctions both have overlap with the same non-magnetic particle. In a similar way the wavefunctions of neighboring cluster cores can experience a super-exchange via the ligand shells. This super-exchange
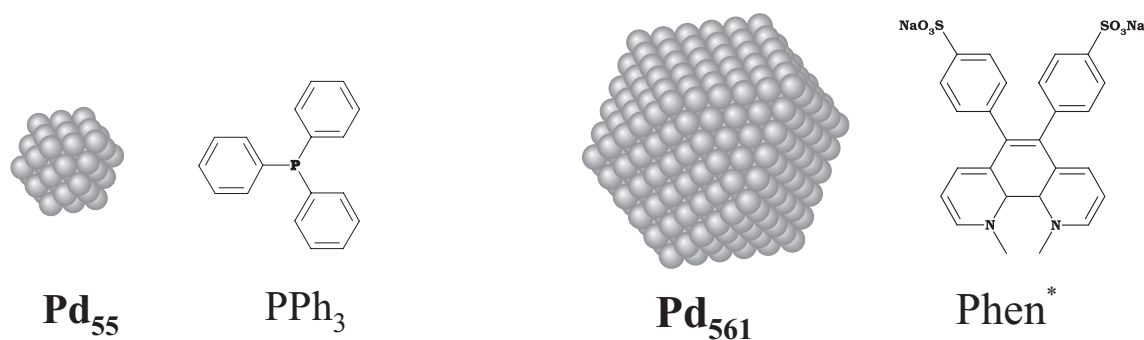
Figure 6.3: *The two palladium clusters used for μSR experiments From left to right: Pd2 metal core, accompanied by a triphenylphosphine PPh₃ ligand and Pd5 metal core together with a phenanthroline derivative Phen* ligand. The oxygen and ligated sites on the surface depends on the number of stabilizing molecules per cluster, the symmetry and geometry. Preferential sites are corner, centre and edge sites of triangular and square faces forming the surface [11, 12].*

involves two ligand shells and will therefore be quite weak.

So far, the influence of the ligands and adsorbed atoms at the surface of the cluster, which stabilize the particle, have been neglected. These are chemically bound to the atoms at the cluster surface, which will obviously have consequences for the electronic properties of the atoms at the surface, and possibly even throughout the whole particle. For QSE one assumes the conduction electrons to be delocalized over the cluster core, but confined to the particle. This means that the cluster core needs to be metallic. A Mössbauer study on the local charge densities in the Pt4 cluster showed that the effect of charge transfer between ligands and metal atoms, is restricted to the first layer of surface atoms only. The remaining inner metal atoms already show the same charge densities as bulk [11]. For Mössbauer experiments on these clusters, the metal atoms are divided in inner core and surface atoms. The surface atoms have a reduced coordination, and some are bonded to the stabilizing ligands. The ligated sites on the surface, are based on symmetry and geometrical considerations.

Up to now an explanation of the origin of an odd or even number of electrons has been avoided here. Palladium has ten $4d$-electrons per atom for its conduction band. So in principle each cluster could only have an even number of electrons. A few reasons can be given, such as a charge transfer between the cluster and its ligand shell. The most plausible reason, however, is the absorption of hydrogen in the clusters. The hydrogen adds an electron to the conduction band. This can go up to as far as 20 at%, and it has equal odd or even probability.

6.4   The two and five shell cluster compounds Pd2 and Pd5

In order to be able to compare our results with previous experimental data, and to study size dependent behaviour as observed with the μSR technique, two palladium 'magic number' clusters were used for the experiments. The two shell Pd2, $Pd_{55}[PPh_3]_{12}O_{30}$, consists of a 55 palladium atoms core, with triphenylphosphine (PPh₃) ligands stabilizing the

Table 6.2: *Parameters for of the Pd-cluster compounds*

label	ligand	metal core diameter (nm)	particle diameter (nm)	sample mass (mg)
Pd2	PPh$_3$	1.1	2.4	50
Pd5 #1	Phen*	2.1	3.8	400
Pd5 #2	Phen*	2.1	3.8	400

surface together with adsorbed oxygen atoms. Similarly, Pd5 with its chemical formula Pd$_{561}$Phen$^*_{36}$O$_{200}$, has a 5 shell palladium core, and the ligands are made of a phenanthroline derivative Phen* (Phen* = 4,7-C$_6$H$_4$SO$_3$Na substituted Phen). Both cuboctaedral metal cores together with the corresponding ligand molecule are shown in Fig. 6.3. One would have preferred clusters with identical ligands, in order to rule out effects due to ligation. However, the cluster size and its synthesis are partly controlled by the ligation. The cluster sizes used could only be produced with the above ligands. The clusters have been prepared by G. Schmid and coworker at Essen University. They were synthesized by hydrogen reduction of palladium(II)acetate in acetic acid solution with their respective ligand molecules. They are obtained in the form of a black powder. Both X-ray and HRTEM are routinely used to characterize the samples. X-ray confirm the *f.c.c.* structure of the palladium core, similar as in bulk. HRTEM corroborated the metal core sizes. Details on core size and particle size of the samples are given in Table 6.2. Particle sizes have been estimated with atoms-bond lengths, assuming a single ligand shell per particle. For Pd5 two samples, labeled #1 and #2, were available. The #2 sample contained an unquantified excess of ligand molecules.

6.5 Motivation for µSR experiments

After the introduction of both the quantum size effect and the cluster samples involved, motivation for launching a µSR study on these clusters seems required. Although aware that this is speculative especially since the cluster samples are complex compositions of the metallic and organic components, these are the first considerations upon starting a pilot study on such materials.

First of all the muon is a very sensitive tool to study small magnetic moments. Dipolar fields due to electronic moments as low as $10^{-4}\mu_B$ have been observed in CeRu$_2$ [13]. This property will be useful since QSE theory predicts one electron spin on the odd number electron clusters. This 1 μ_B magnetic moment is expected to be delocalized over the Pd-core of approximately ten to hundred atoms, reducing the effective dipole field in the core.

A second advantage of the muon, is that it acts as a local probe in the cluster, in contrast to susceptibility and specific heat, which measure bulk sample properties. For this reason one could expect to observe direct proof of a 50/50 odd even ratio in the cluster sample. Furthermore, the local probe could give supporting evidence that the observed paramagnetic behaviour is due to a quantum size effect on the clusters and not caused by a level of a few ppm of impurities in the starting materials.

The field dependence of the spectra might give information on the magnetic field or field distribution on the muon site. These would give an indication of the size of the

magnetic moments involved.

Most promising for a confirmation of QSE would be clear features in the temperature dependence of the spectra. Characteristic temperatures in the behaviour of the depolarization rate versus temperature, could indicate a slowing down of the magnetic spin fluctuations. Additionally one would expect characteristic temperatures to be determined by QSE as well. This implies specific temperatures which should differ by an order of magnitude between both cluster samples.

6.6   Experimental environment and set up

The Pd2 sample was measured at the general purpose spectrometer (GPS) at PSI. For this purpose the electrostatic kicker device MORE (see section 2.3.2) was installed. It extends the time window, enabling investigation of weakly oscillating/damped signals. The sample was mounted in a small containment($\varnothing$ 0.5 cm) of aluminized tape, spanned between the legs of a fork shaped sample holder. The sample holder construction allows for a optimal reduction of background, because muons are hardly stopped in the tape, and those that miss the sample could be vetoed with an electronic coincidence circuit. In this way we were able to measure the Pd2 sample with a weight as small as 50 mg. At the low temperature facility (LTF), such a set-up is not available. Thus measurements on Pd2 have only been performed above 1.6 K in a ^{4}He cryostat (Quantum design).

Both Pd5 samples have been measured at the MuSR and EMU spectrometers at ISIS. After a rough temperature scan both Pd5 samples were found to give identical μSR spectra and were combined (*i.e.* not mixed) in one sample holder to increase the sample surface. Note that for MuSR a 3 cm diameter beamspot requires rather large samples. The powder sample was in a 2.5 cm diameter silver plate sample holder, with a thin mylar foil window. To prevent settling and ensure thermal contact, the powder was pressed with a 4 ton load. In this way measurements with a reasonable signal to noise ratio could be done in both the closed cycle refrigerator (15-400 K) and the dilution refrigerator (40 mK-4.2 K).

Additional measurements were made on the ligand materials. Although a pure PPh$_3$ sample was available, Phen* sample was not, and measurements could only be done on a related pure Phenantroline (Phen = $C_{12}H_8N_2$) compound. Both compounds were pressed into a number of pellets which could cover the beam spot area.

Only recently a fly-past set-up in a flow cryostat (4-300 K) has become available on EMU. A flow cryostat provided with an extra window behind the sample and an extension of the vacuum beam tube, allow muons which missed the sample to travel along outside the range of the positron detectors. 1 cm diameter pellets were pressed out of both Pd5 samples and glued on a 1 mm thin silver sample holder. In a first attempt, a combined sample was used, in a way similar to previous measurements described above. The performance of the fly-past set-up proved that it could handle even smaller samples. This resulted in additional temperature scans on both sample #1 and #2 separately. So far only temperature scans have been performed with this low background set up.

6.7   μSR experimental results

The palladium nano-particles can be approximated as two components: the metal core and the shell composed of oxygen and ligands. As the quantum size effect of interest
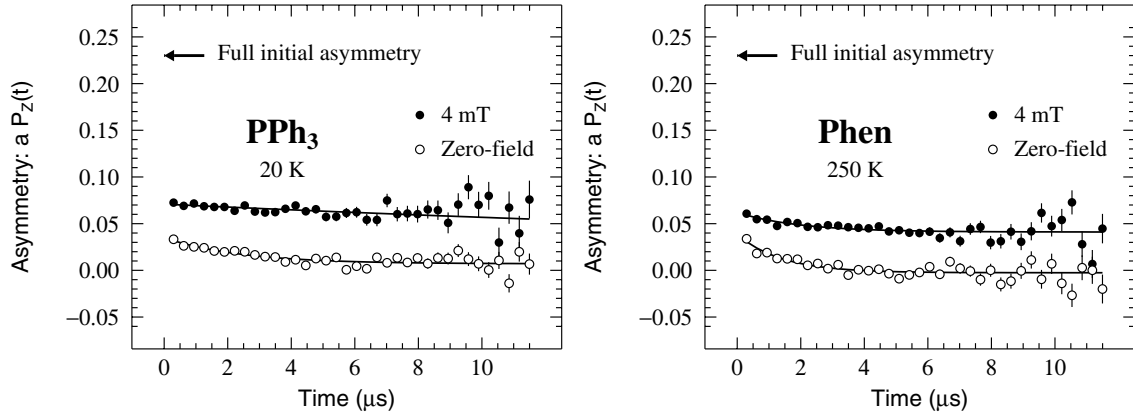
Figure 6.4: *Two µSR spectra recorded at 20 K for both ligand materials PPh$_3$ and Phen. The initial asymmetry is strongly reduced relative to the full value. An applied longitudinal field of 4 mT approximately doubles the initial asymmetry relative to the zero-field case. These spectra have been recorded at ISIS with a closed cycle cryostat on a large sample. This explains the extremely small value of a_{bg}.*

is related to the metal core, it was considered useful to measure the muon response of the ligands separately. Similar measurements on the oxygen part could not be done. This method might enable to distinguish ligand contributions to the spectra from those due to the metal core. First the ligand data will be presented and afterwards used for interpretation and analysis of the Pd cluster data.

6.7.1 Experimental results on the ligands

For both bare ligand compounds, spectra have been recorded at temperatures and magnetic fields overlapping those of the cluster compounds themselves, with the intention of comparing both sets of data. In Fig. 6.4 we present two spectra in zero field and 4 mT for PPh$_3$ at 20 K and Phen at 250 K, respectively. The initial asymmetry in zero-field is much smaller than the full initial asymmetry available measured *e.g.* for a simple metal compound. This indicates that a large part of the signal rapidly depolarizes. The remaining spectrum for both compounds could now be fitted satisfactorily with a simple exponential. For PPh$_3$, the initial asymmetry is temperature independent: $a_{li} \simeq 0.04$. The exponential damping rate, λ_{li}, is constant up to 70 K and then decreases slightly: from $\lambda_{li} \simeq 0.3$ MHz at 70 K to $\lambda_{li} \simeq 0.2$ MHz at 290 K. For Phen both the asymmetry and depolarization rate in zero-field spectra are temperature independent with $a_{li} \simeq 0.05$ and $\lambda_Z \simeq 0.8$ MHz. Hence the zero-field µSR response of the ligands is quite favorable since a_{li} is always small and the spectra are temperature independent in the whole temperature range for Phen and below 70 K for PPh$_3$.

As seen in Fig. 6.4 we observe an enhancement of a_{li} and a decrease of λ_{li} in a longitudinal field, *i.e.* for an external magnetic field applied along the initial muon beam polarization. Considering both ligands are organic molecules with aromatic rings, it is very likely a muonated radical will be formed upon implantation. Applying a magnetic field will result in a recovery of the asymmetry and decrease of depolarization as was explained in section 3.5.2. This is indeed observed, and is illustrated for PPh$_3$ at 20 K in Fig 6.5. For Phen 5 K data have been combined with 250 K spectra, because no
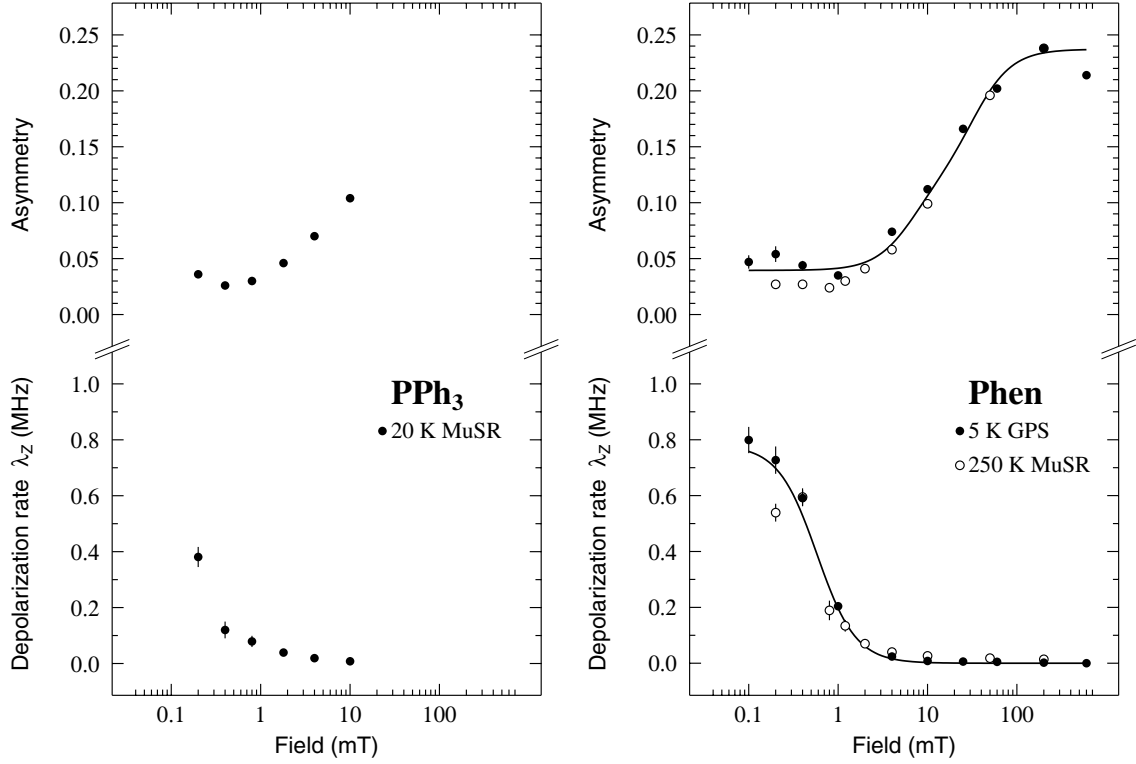
Figure 6.5: *Recovery of the asymmetry and decrease of the relaxation for PPh$_3$ and Phen over a field range. For Phen both GPS and MuSR data at 5 and 250 K have been combined. The solid line in the asymmetry represents a fit with an empirical function by Pratt [14], see text. The relaxation is fitted by a Lorentzian.*

temperature dependence was observed. The differences between both spectrometers were corrected by equating both aymmetries at 200 mT. Unfortunately, due to the limited beam time available, the field scan on PPh$_3$ was restricted to low fields. However, for the Phen cluster a complete scan was done, resulting in a typical repolarization curve.

The fact that the asymmetry at low fields is less than half (almost $\frac{1}{6}$th) of the high field value, indicates that the system has an anisotropic contribution. For a general orientation of the field with respect to the principal axis of the interaction and thus also for a powder sample, the repolarization curve needs to be computed numerically. Pratt has introduced an empirical model [14], assuming a hyperfine coupling of axial symmetry, see section 3.5.2. A fit with this model is shown in Fig. 6.5. The corresponding Eq. 3.28 extracts the values for the isotropic and anisotropic components of B_0=33(1) mT and B_1=7(1) mT, respectively. The development of the depolarization rate has been described by a Lorentzian.

Additionally, a 300 mT transverse field experiment on Phen ligand at 295 K was done to obtain information on the number of muon sites and their origin. Comparison with similar measurements on the cluster samples might give more insight on the character and the relative contribution of the ligands to the cluster sample. At high fields each radical is expected to give satellite peaks in the frequency spectrum on both sides of the diamagnetic frequency. In first order these satellite frequencies are given by: $\nu_\pm = |\nu_\mu \pm \frac{1}{2}A_\mu|$ [15]. So the number and position of the satellite peaks can reveal the number and origin of the
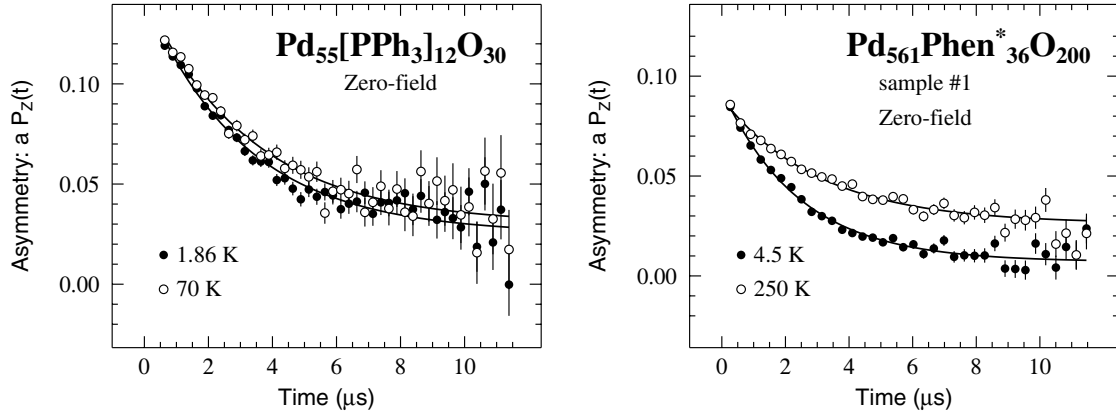
Figure 6.6: *Zero-field μSR spectra recorded at two temperatures for both $Pd_{55}[PPh_3]_{12}O_{30}$ and $Pd_{561}Phen^*_{36}O_{200}$. The solid lines are fits as explained in the main text. These comparisons shows that the μSR depolarization rate λ_Z is larger at the lower temperatures. The spectra for Pd2 have been recorded at GPS, and Pd5 at EMU, both in their characteristic "fly-past" mode.*

radical. However, the frequency spectra did not show any clear peaks. This is probably due to remaining anisotropy at these temperatures. Since these negative results make comparison with cluster data redundant, similar measurements on the latter have been ignored.

6.7.2 Experimental results on the Pd clusters

In Fig. 6.6, typical spectra recorded for both the Pd2 and Pd5 cluster samples are shown. In a first attempt they have been analyzed as a sum of two components:

$$aP_z(t) = a_{cl}P_{cl}(t) + a_{bg} \tag{6.2}$$

The first term $a_{cl}P_{cl}(t)$ describes the μSR signal from the cluster sample and the second accounts for the background, due to muons stopped in *e.g.* the cryostat walls and sample holder. The latter is virtually absent for the Pd5 spectra in the EMU with "fly past" set up. The asymmetry due to the sample a_{cl} is temperature independent and noticeably reduced, relative to its expected full value. However, this reduction is much less than the decrease observed with the ligand samples.

In zero-field, for all temperatures and for both compounds, the depolarization from the sample is well described by an exponential function, *i.e.* $P_{cl}(t) = \exp(-\lambda_z t)$, as is illustrated in Fig. 6.6. The depolarization rate versus temperature $\lambda_Z(T)$ is displayed in Fig. 6.7 for Pd2 and a Pd5 sample composed of samples #1 and #2. Because the fly-past mode appeared successful for smaller sample sizes, an additional measurement was done on the individual samples #1 and #2 during a subsequent experiment. The results are illustrated in Fig. 6.8. The temperature dependence of the individual Pd5 samples appear more scattered when compared to those of the combined sample. Additionally the level of depolarization has increased for both individual samples. Although the samples have been stored under argon gas during half a year between the two experiments, this could be related to some kind of aging of the samples. The depolarization rates for the #1 and
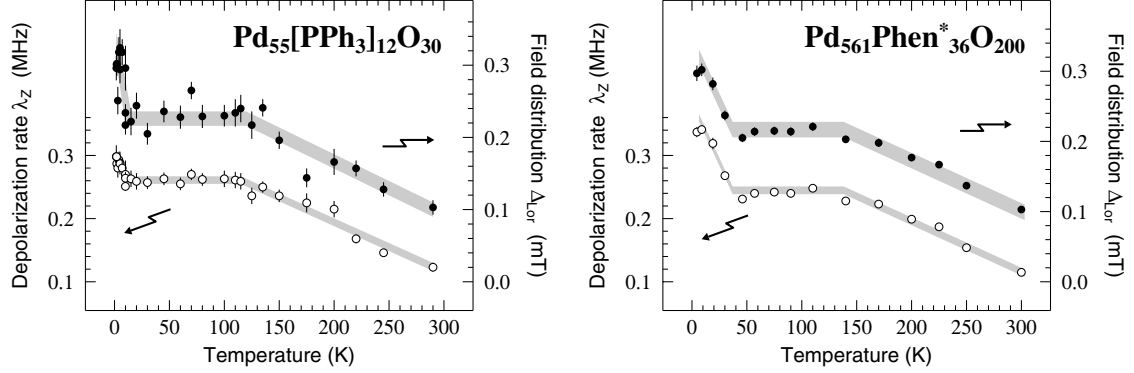
Figure 6.7: *Temperature dependence of the zero-field depolarization rate λ_Z and of the half-width at half maximum of the field distribution Δ_{Lor} for the $Pd_{55}[PPh_3]_{12}O_{30}$ and the combined $Pd_{561}Phen^*_{36}O_{200}$ cluster sample. The lowest temperatures are 1.8 K and 4.5 K, respectively. Pd2 data obtained at the GPS spectrometer and Pd5 at the EMU spectrometer both in their "fly-past" modes. The grey lines are guides to the eyes.*
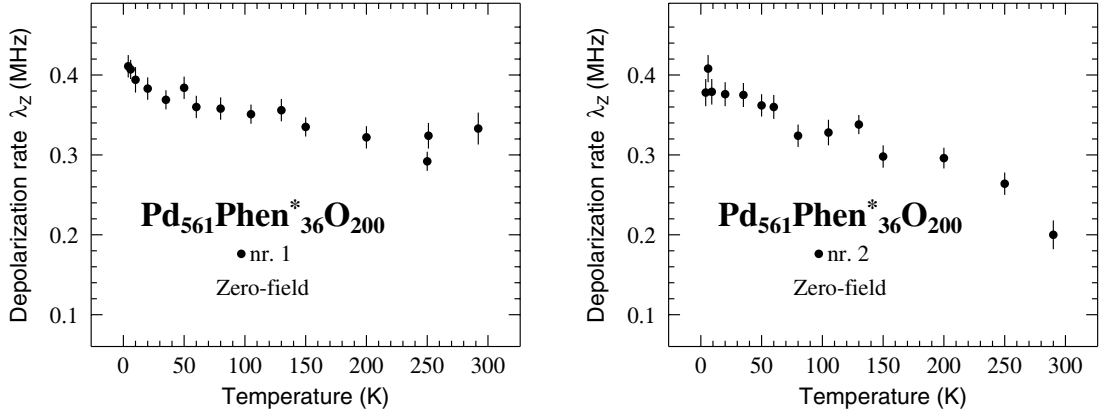

Figure 6.8: *Temperature dependence of the zero-field depolarization rate λ_Z for the individual $Pd_{561}Phen^*_{36}O_{200}$ cluster #1 and #2 on the left and right, respectively. Data have been recorded in the flow cryostat of the EMU spectrometer in "fly-past" mode.*

#2 samples are comparable up to 200 K. Above 200 K the rates clearly differ. This is probably due to the difference in the amount of ligand in the two samples.

The combined Pd5 and Pd2 samples seem to behave in a very similar way. For this reason from here on temperature behaviour of the latter two samples will be discussed. For both compounds $\lambda_Z(t)$ exhibits a plateau at intermediate temperatures, with comparable magnitudes 0.26 and 0.24 MHz. The plateau is characterized by two characteristic temperatures at low and high temperatures, which will be referred to as T_{low} and T_{high}. At T_{high} around 120 K, an approximately linear decrease of $\lambda_Z(T)$ begins which continues down to 0.12 MHz at 300 K.

Although for both compounds $\lambda_Z(T)$ increases with decreasing temperature, the onset temperature T_{low} is different for the two cluster samples. For Pd5 $\lambda_Z(T)$ starts to increase below 40 K, and due to its slightly curved shape, seems to saturate at 0.34 MHz. On the other hand, $\lambda_Z(T)$ in Pd2 only starts to increase below 14 K. It is hard to say whether it

has already saturated at 1.8 K.

From these observations, we have to conclude that in these μSR experiments no evidence for the quantum size effect is observed. For this one could have expected characteristic temperatures in the temperature developments of the depolarization rate. However, the theory predicts a smaller energy gap, and thus a lower characteristic temperature for the larger cluster and *vice versa*. Furthermore, the cluster sizes have been chosen such that these temperatures should differ by an order of magnitude between the clusters. This picture does not comply with either of the characteristic temperatures T_{low} and T_{high}. This leaves the discussion of the origin of the temperature development to the discussion section.
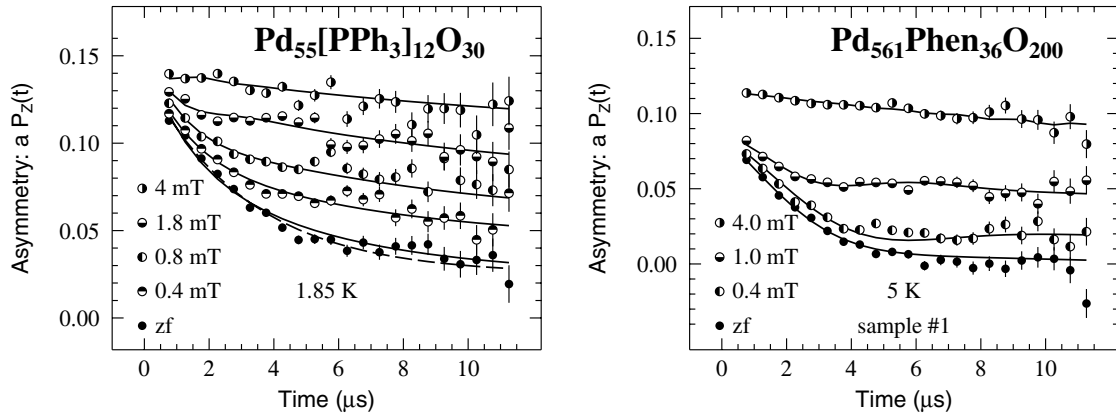

Figure 6.9: *Longitudinal field dependence of μSR spectra for the $Pd_{55}[PPh_3]_{12}O_{30}$ and $Pd_{561}Phen_{36}^*O_{200}$ at 1.85 K and 5 K, respectively. The solid lines are fits to Eq. 6.5. In this fit the field distribution Δ_{Lor} and the correlation frequency ν_c are allowed to vary with applied field. The dashed line is the result of the fit of the zero-field spectrum with an exponential depolarization function. These data prove that the observed depolarization is induced by a quasi-static field distribution. The spectra for Pd2 and Pd5 were taken at GPS.*

In order to gain more insight into the origin of the depolarization, static or dynamic, and the corresponding field distribution, additional longitudinal field measurements have been performed for the two compounds at selected temperatures: 1.8, 70 and 220 K for Pd2 and 5, 70 and 250 K for Pd5. The spectra corresponding to the field scan at 1.8 and 5 K for both compounds are illustrated in Fig. 6.9. The spectra for field scans at the remaining temperatures show a very similar quenching of the depolarization rate. This quenching with relatively small fields, suggests depolarization is induced by a quasi-static field distribution *i.e.* its fluctuation rate is smaller than 1 MHz. The field dependence of both the initial asymmetry and the depolarization rate for the two cluster samples are given in Fig. 6.10. It should be noted that λ_Z was obtained from a single exponential fit. However, for intermediate fields this model did not describe the spectra satisfactorily, and therefore for these fields the depolarization rate values have been omitted in this plot. In the same way as for the ligands the asymmetry has been fitted with the empirical Pratt function, resulting in isotropic and anisotropic components of 48 and 7 mT, respectively. To ensure a good fit, a constant level was added to the asymmetry of 0.07, which could be assigned to a contribution either due to the Pd core or to background. The dotted line in Fig. 6.10 represents a repolarization curve with a 0.2 T isotropic component. The
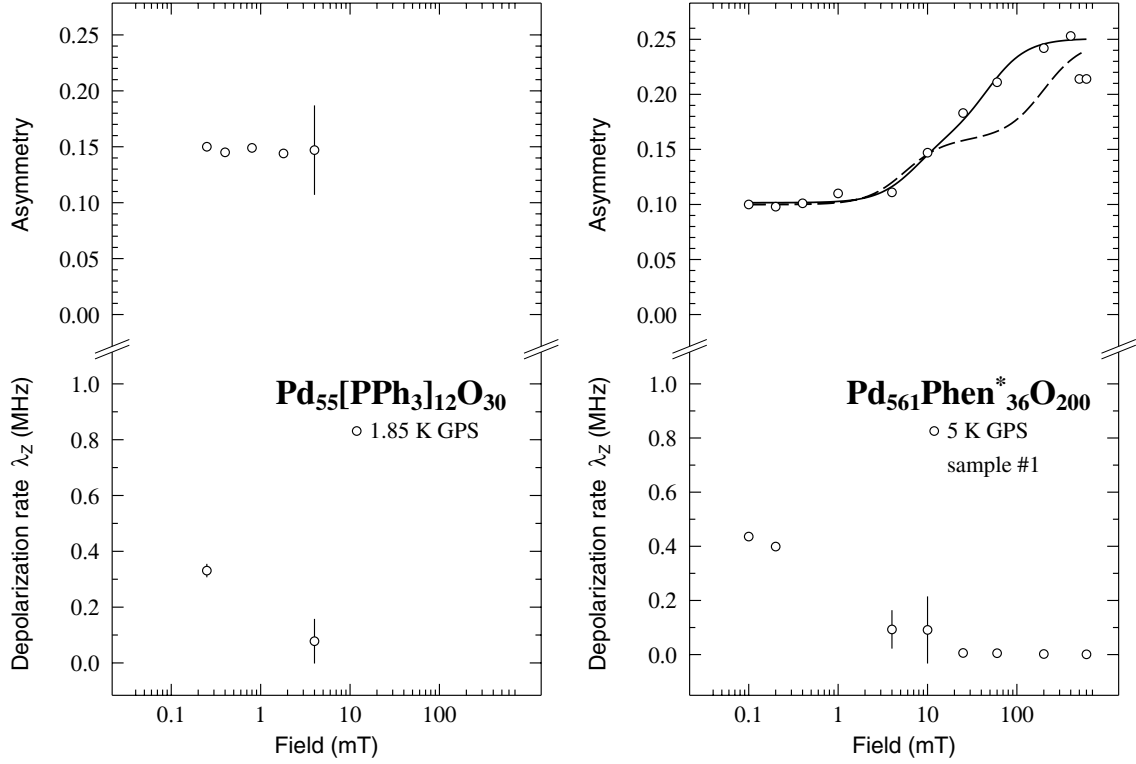
Figure 6.10: *Recovery of the asymmetry and decrease of the relaxation for $Pd_{55}[PPh_3]_{12}O_{30}$ and $Pd_{561}Phen^*_{36}O_{200}$ over a field range. The solid line in the asymmetry represents a fit with an empirical function by Pratt [14] resulting in a isotropic contribution of 48 mT. The dotted line represents a similar fit, with an isotropic contribution of 0.2 T. The latter clearly does not describe the data at higher field accurately, and gives additional proof that the predicted 0.2 T dipolar field is not observed.*

fact that the total repolarization only starts at a higher field as compared to the data, indicates that a predicted 0.2 T dipolar field is not present in the Pd5 sample. This does not rule out an 0.2 T super-exchange, because this involves the overlapping charge distributions of the delocalized electron and the ligand.

The most striking difference between the Pd cluster spectra and their ligand counterparts as illustrated in Fig. 6.4 and 6.9, is the gain in initial asymmetry for the Pd clusters. Clearly, the muons do sense the influence of the Pd-core. The local probe behaviour of the muon rules out the influence of impurities.

Regarding the comparison of the field dependence of the spectra for ligands and cluster sample, it can be stated that the behaviour above ≈10 mT, is very similar. For these fields, the spectra only slowly depolarize, and this can easily be fitted with a single exponential. However, as was mentioned previously, this simple model could not be used at intermediate fields. This anomaly is not observed in the ligand samples. However, this is not beyond dispute, due to their small asymmetry at these fields.

6.8   Data-Analysis

As was mentioned above, observation of the quantum size effects in the μSR results can be ruled out. Nevertheless the spectra do show both a clear temperature and magnetic field dependence. In order to understand the behaviour a closer look at the origin of the μSR signal is needed. Since μSR implants the muons in the sample, where they act as a local probe, analysis of the data requires some consideration of the possible muon sites within the sample. The sample is considered as two components; the Pd metal core and the ligand shell. The oxygen is neglected here, because no separate measurements could be done to obtain its contribution. First we will present the option of the muon in either of the components, afterwards a distribution over the Pd core and the ligands is considered.

6.8.1   Analysis for muons in the Pd-core

Palladium metal is extensively investigated as a model for gaseous hydrogen storage media, because considerable amounts of hydrogen can be reversibly absorbed and desorbed at interstitial sites. In fact the magic number clusters Pd2, Pd5 and Pd7 have been studied for this reason by Nützenadel *et al.* [16]. The adsorption energy for hydrogen on the surface is assumed to be approximately an order of magnitude higher than that for the bulk [17]. If the muon is considered to behave like a light proton, it would presumably reside interstitially and possibly near the surface of the Pd-core. Here some possible μSR responses will be considered, assuming that all the muons occupy interstitial Pd-sites.

If all the muons would reach the Pd core upon implantation, one could expect several contributions to the depolarization. First of all ^{105}Pd with a natural abundance of 22% and spin 5 half, carries a nuclear moment of 0.642 μ_N [18]. Field distributions due to these moments have been calculated with Eq. 4.2. For the most probable interstitial $(\frac{1}{2}, \frac{1}{2}, \frac{1}{2})$ site, this results in a depolarization rate λ_Z of 0.04 MHz. This is far below the depolarization rate as observed for the clusters, and thus one can conclude that it must originate elsewhere.

Although no evidence was found for quantum size effects in the temperature variation studies of the clusters, it does not rule out the possibility that a fraction of the clusters do carry a 1 μ_B magnetic moment due to a delocalized electron. How would this effect λ_Z? The induced field of 1 μ_B at 1 nm is 1.9 mT. Such a static field would induce a muon precession frequency of 0.25 MHz, which is well within the range of the spectrometers used. However, oscillations have not been observed over the whole temperature range.

On the other hand the depolarization might result from a field distribution induced by dipole fields due to the uncompensated electron spin. The depolarization function for such a distribution is well known in metallic compounds and was introduced in section 3.2 as the Kubo Toyabe function (KT). The typical spectral shape of this KT function, with a clear minimum and recovery to $\frac{1}{3}$ of the asymmetry does not correspond to the spectra observed. The more or less exponential shape of the zero field data suggests a fluctuating field distribution, represented by the dynamical Kubo Toyabe function as represented in section 3.3 in Fig. 3.3. The number of parameters in an exponential function is less than for the dynamical Kubo Toyabe (DKT) function. The main advantage of the latter however, is that it predicts the change of the spectrum upon applying a longitudinal magnetic field. From this, an estimate for the field distribution could be obtained. Before

going into the field dependence, we will first address the origin of the field distribution and estimate its magnitude.

Assuming that delocalized electrons are present, the muons will be distributed over odd and even electron clusters and over several different sites within a Pd-core as well. In more, detail two sources of μSR depolarization are possible: these originate from the magnetic density induced by neighboring nanoparticles Δ_1 or from the magnetic density within the particle in which the muon is implanted Δ_2. For computation of the latter source the internal magnetic field distribution for a delocalized electron would be needed. To our knowledge this has not been considered so far and is beyond the scope of this thesis. For the depolarization due to dipole moments on neighboring clusters, however, an upper limit can be given. For the calculation, basic magnetostatics theory tell us that the magnetic density can be taken as concentrated in the center of the nanoparticle. The depolarization occurs because of the random orientations of the electronic paramagnetic moments. We suppose that the nanoparticle in which the muon is implanted is surrounded by n nearest neighbor nanoparticles with uncompensated spins located at a mean distance $\bar{r}$. Each uncompensated electron carries a Bohr magneton μ_B. For a Gaussian field distribution, the root mean square (rms) of the distribution is given by $\Delta_1 = (\mu_0/4\pi)(\sqrt{2n}\mu_B/\bar{r}^3)$, where μ_0 is the permeability of vacuum [19]. If we suppose $n = 6$, corresponding to the hypothesis of half of the nanoparticles having a spin, and take the minimum value that $\bar{r}$ can reach corresponding to the diameter of the cluster d_s, as given in Table 6.2, we get an upper limit for Δ_1: 0.35 mT and 0.06 mT for Pd2 and Pd5, respectively.

The temperature dependence of the spectra have been fitted with a dynamical Kubo Toyabe function given by:

$$a_{cl}P_{cl}(t) = a_{Pd}P_{DKT}(\Delta_{Lor}, \nu, t) \tag{6.3}$$

where $P_{DKT}(\Delta_{Lor}, \nu, t)$ is the depolarization function for a dynamic Kubo Toyabe with a Lorentzian field distribution. Here a Lorentzian, as opposed to a Gaussian distribution was used, because this model described the spectra slightly better. This model is used in spin glass and dilute magnetic systems [21, 22]. Because the uncompensated electron is delocalized and only a 50 % of the clusters is supposed to carry this spin, this model might represent the physics better. $P_{DKT}(\Delta_{Lor}, \nu, t)$ is characterized by the half-width at half maximum of the field distribution, Δ_{Lor}, and the correlation frequency ν_c. The zero field data have been fitted with a temperature independent ν_c of 0.2(1) MHz. The results for Δ_{Lor} are added to Fig 6.7. It should be noticed that the fits did not perfectly describe the data. The value for Δ_{Lor} corresponds well with the upper limit calculated previously. It is remarkable that the field distribution is independent of the cluster size. This and the fact that the calculated upper limit for Δ_{Lor} only partly covers the observed distribution in Pd5, suggests that either the internal field distribution is of significant importance here, or the model used with the muon residing in the Pd-core is incorrect.

As was mentioned before, this dependence with field for the dynamical Kubo Toyabe function can be calculated numerically and compared with the experimental data. Several attempts to fit the data with Eq. 6.3 including the field dependence have been made. None of these described either the development of the asymmetry nor the depolarization rate, satisfactorily. This is probably due to the contribution of a rapidly depolarizing contribution. Such a contribution was observed in the pure ligand sample. Thus, the next section will focus on the expected results for all muons incorporated in the ligands.

6.8.2 Analysis for muons in the ligands

The clusters are covered with a ligand shell for stabilization. These ligands are organic molecules with aromatic rings, thus it is very likely a muonated radical will be formed upon implantation. This has been observed for the pure ligand data. The theory of muonated radicals is given in section 3.5, and depolarization for these is usually described by a simple exponential. For the cluster sample a loss of initial asymmetry comparable to that observed for the pure ligands is observed. This could indicate that the muon is indeed situated in the ligands. However, the initial asymmetries between these compounds differ by a factor of two. This could be due to the bond of the ligand with the Pd surface. It should be noted here however, that the ligands are relatively large and it is likely that between the muon site in the ligand and the Pd, there are several atom-bindings. This would probably reduce the effect of the attachment to the Pd. However, the radical created in the process of addition of muonium to the ligand, is distributed over several sites of the aromatic ring(s). Attachment to the Pd might pull the radical more towards the electronegative Pd and reduce interaction and reduce its anisotropy. Fits with an empirical function by Pratt [14] to $\lambda_Z(T)$ suggest that the isotropic part of the interaction would increase from 33 mT to 48 mT up on addition to the Pd. Although the general behaviour of the repolarization of the clusters match the ligands, the asymmetry difference at low field seems to be in contradiction with what is expected.

6.8.3 Analysis for muons distributed over ligands and Pd-core

So far it has been assumed that the muon is in either of the two components building the cluster. For the cluster samples, one could assume one of the two possible muon sites to be energetically favorable over the other. However, a distribution over both sites is also possible. Especially because the field dependence of the asymmetries for the clusters do show an enhancement at low field assignable to Pd, but a repolarizing behaviour very similar to the one found for the ligands.

Because neither a picture with all muons in the Pd core, nor one with all of them incorporated in the ligand shell appear to represent the observed data accurately, a distribution over both is assumed. A fraction of the muons binds to the ligands whereas the remaining ones reside in the Pd core. The aim of a proper analysis would be to unravel the fraction of both contributions to the signal and correct for the ligand part. In order to do so two options have been considered: discern on depolarization $P_Z(t)$, or on asymmetry a.

The zero field data of both the clusters and the ligands could be fitted in a first attempt with an exponential function. This already indicates that spectra for both compounds have a very similar shape. The exponent λ_Z can be considered to represent the slope at the start of the spectrum. Unfortunately the exponents of both compounds are of the same order of magnitude as well. This excludes the possibility to extract the fraction of the asymmetry due to the ligands from the Pd-cluster spectra.

The second option is to look at the asymmetry by splitting the spectra in two contributions. To do so, one has to assume that the fraction of muons implanted in the Pd-core would give full asymmetry. With this assumption, the reduction of the asymmetry as is observed for both ligands and clusters compounds, could be assigned completely to the ligands. Experiments on other metal compounds usually give the full asymmetry of the

spectrometer, supporting this hypothesis. The cluster asymmetry can now be written:

$$a_{cl} = a_{Pd} + a_{lig} = fa_f + p(1-f)a_f \qquad (6.4)$$

Here a_{cl}, a_{Pd} and a_{lig}, represent the initial asymmetry of the cluster, the Pd-core and the ligands respectively. a_f is the full asymmetry of the spectrometer and f, the percentage of muons stopped in the Pd-core. The fraction p, gives the visible part of the ligands contribution, and depends on the applied field (p=0.16-1.0). Since all other parameters are known from experiments, f was determined to be 0.33. This results in a fraction of asymmetry due to the Pd-core asymmetry of 0.75 for zero-field, reducing to 0.33 at 200 mT.

We have presumed the spectra to consist of a sum of two independent contributions. This also implies two independent depolarization functions $P_Z(t)$. The ligands could be described as a single exponential, which is common for muonated radicals. The contribution of the Pd-core, however, can take different shapes. According to the Quantum size theory the Pd-core with an odd number of electrons would carry one uncompensated delocalized spin. Now if the muon would, due to this electron, feel a unique field for all sites with in the Pd-core, an oscillation related to the local field would be expected (See section 3.2). No oscillations were observed in the experiments. This is not surprising, since the muon will apart from the moment on their specific Pd-cluster, also experience the dipole field of neighboring clusters. This will result in a distribution of fields. If on top of that these field fluctuate in time, the spectra should be modeled with a dynamical Kubo Toyabe depolarization (DKT) function (See Fig. 3.3). For fluctuation rates equal or greater than the width of the field distribution, this depolarization function can be approximated by an exponential. This exponential behaviour is observed in the experimental data. The number of parameters in an exponential function however is less than for the dynamical Kubo Toyabe function. The main advantage of the latter, however, is that it predicts the change of the spectrum upon applying a longitudinal field. From this an estimate for the field distribution could be given.

The complete model is now written:

$$a_{cl}P_{cl}(t) = a_{Pd}P_{DKT}(\Delta_{Lor}, \nu, t) + a_{lig}\exp(-\lambda_{li}t) \qquad (6.5)$$

where $P_{DKT}(\Delta_{Lor}, \nu, t)$ is the depolarization function for a dynamic Kubo Toyabe with a Lorentzian field distribution. $P_{DKT}(\Delta_{Lor}, \nu, t)$ is characterized by the half-width at half maximum of the field distribution, Δ_{Lor}, and the correlation frequency ν_c.

Combining the models of the predicted contributions to the asymmetry in Eq. 6.4 and their corresponding depolarization functions Eq. 6.5, should give nice fits on the field scan spectra. Several attempts were done, but proved unsuccessful. In the first place, the asymmetry predicted by the model did not correspond to those observed in the spectra, especially for fields over 0.4 mT. This is illustrated for Pd2 in Fig. 6.11. This could be due to the fact that the Pd-core does not contribute the full spectrometer asymmetry. Another option could be that the addition of the ligand to the Pd-core, has changed the repolarization behaviour of the muonated radical. Secondly, for the field scan one would assume that the field distribution and the correlation frequencies remain unaltered. However, for fits above 0.4 mT, ν_c needs to be reduced from 2(1) MHz, to approximately 0 MHz. Additional to the DKT fits, similar fits with a Gaussian field distribution have been performed. Fits with this model however, gave very similar problems and results.
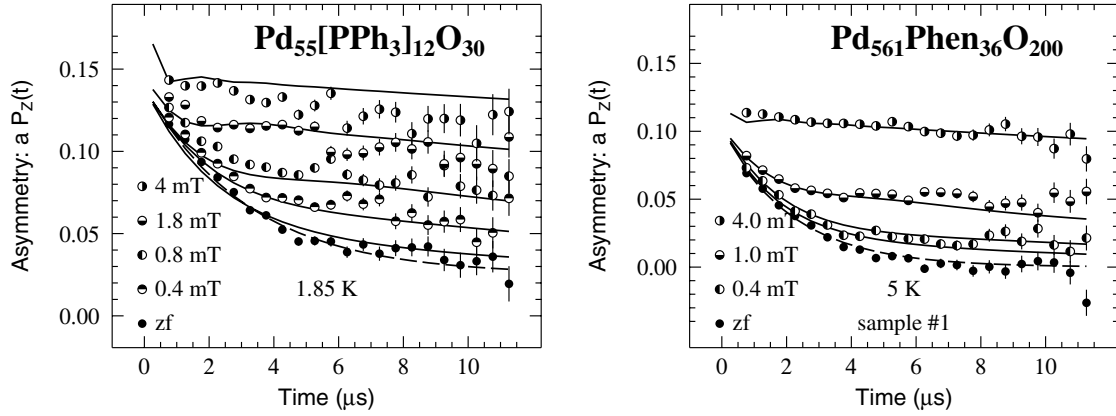
Figure 6.11: *Longitudinal field dependence of μSR spectra for the $Pd_{55}[PPh_3]_{12}O_{30}$ and $Pd_{561}Phen^*_{36}O_{200}$ #1 at 1.85 K and 5 K, respectively. The solid lines are fits to Eq. 6.5. The spectra were analyzed with contributions from the Pd core and the ligand shell. The contributed asymmetries for both were obtained from measurements on the ligand samples and Eq 6.5. The field distribution Δ_{Lor} and the correlation frequency ν_c were assumed to be independent of the applied field. The dashed line is the result of the fit of the zero-field spectrum with an exponential depolarization function. The spectra for Pd2 and Pd5 were taken at GPS.*

In the end the solid lines plotted in Fig. 6.9, represent fits with Eq. 6.5 neglecting the predicted asymmetries and the need for a constant ν_c. Although both asymmetry and ν_c change gradually with field, the data do not comply with our initial model, and introduces extra free parameters. The field dependence of the depolarization function, however, is obvious from the spectra. It changes drastically between zero and 4 mT. All fits thus far, supported a field distribution of 0.3(1) mT at low temperatures.

6.9 Discussion

The several attempts presented in the previous chapter have not been able to give a consistent picture on the site of the implanted muon within the cluster samples. The muons could reside in the Pd-core, at the Pd surface, in the ligands or distributed over these sites. This obviously complicates the interpretation of the data. Nevertheless the spectra do show a clear dependence on both temperature and magnetic field.

The magnetic field dependency was also used in an attempt to locate the muon. Assuming the muon resides interstitial in the Pd core, then the field dependence of the μSR depolarization shows that depolarization is induced by a quasi-static field distribution. Here quasi-static is related to the muon life time, and refers to fluctuation rates smaller than 1 MHz. This suggests that the muons do not move during the measurements. Magnetic field scans have been performed for both clusters at several temperatures. In all cases the depolarization shows very similar quenching behaviour, and it is thus concluded that no muon diffusion occurs in these samples over the whole investigated temperature range. This in contrast to indications for bulk Pd and elements such as Pt [20]. The muon could be pinned to an impurity. The most obvious imperfection here is the surface, which depending on the cluster contains 76% or 45% of the Pd atoms.

The spectra do not give any indication towards an odd/even distribution over the clusters. Such a distribution was to be expected, because the muon will either be situated in a cluster with or without an uncompensated electron. Analysis with a 50/50 distribution forced in the model, did not improve an understanding either. Dipole calculations for a 1 μ_B magnetic moment per every other cluster, do give results within the same range as those obtained from a fit with dynamical a Kubo Toyabe function. Nevertheless, these calculations do predict a difference between the two clusters, related to their size and thus the muon distance to the dipole. Such a difference between the clusters is not observed experimentally.

Furthermore, to understand the maxima observed for the susceptibility at low temperature, Volokitin *et al.* supposed that there is an internal field $B_{int} \simeq 0.2$ T acting on the small particles. The analysis of their specific heat data also suggests the existence of B_{int}. If such a field of such magnitude was present in the interstitial sites of a nanoparticle, we should have detected it either as a μSR Larmor precession frequency (corresponding to the average field) or a strongly depolarized signal (related to the second moment of the field). Such a field has not been observed in either of the cluster samples.

If the muon forms a muonated radical in the ligands, this could effect the interpretation. First of all, the odd/even effect will be less dominant, since the distance to a metal with or without a dipolar moment will be comparable. This is due to the fact that the ligands probably extend from the cluster surface and are relatively close to neighboring particles.

Theory for μSR on muons in inorganic crystalline materials compared to muonium or muonated radicals are presented separately in literature, and are also presented apart in chapter 3. The reason for this is the fact that in the latter, the relaxation is due to a dynamic induced perturbations. An estimate for the hyperfine interaction can be obtained from a repolarization curve. In Fig. 6.10 the repolarization of the initial asymmetry was fitted with a model by Pratt [14]. The results give an hyperfine interaction around 48 mT. One could well imagine that such an interaction with the muon initiated radical, obscures the smaller moment on the Pd core.

The proposed internal dipolar field of 0.2 T, however, should still be easily visible. Magnetic fields in the order of 1 mT, have been detected by a spin precession signal in organic molecular compounds [23]. Similar signals were not observed here. These observations cannot exclude a possible super-exchange, with interaction of the extended electron charge distribution via overlap with the non-magnetic ligand orbitals.

The observation which remains to be explained is the temperature dependence of the depolarization for both clusters. Analyses with either a single exponential or a dynamical Kubo Toyabe both result in a similar temperature dependence for the depolarization rate and the deduced magnetic distribution, respectively. Also the developments of the depolarization rate with temperature is very similar for both clusters. For both particles a plateau in $\lambda(T)$ is observed with a decrease above 100 K. An increase is found at the lower end of the temperature plateau at 14 and 50 K for Pd2 and Pd5 respectively.

The decrease above 100 K cannot be explained by muon diffusion, because magnetic field scans at these temperature quench the depolarization with fields as small as 4 mT. The decrease could be related to the decrease of the magnetic susceptibility of bulk and colloidal palladium. A maximum is observed around 100 K in the paramagnetic enhanced susceptibility. It should be noted however, that such a maximum is not observed in similar Pd-clusters, and the Stoner enhancement factor is found to reduce with increasing cluster

size [24].

The second characteristic temperatures are found at 14 K and 50 K, for Pd2 and Pd5 respectively. These can probably be explained with an increase of magnetic correlation between the nano-clusters. It is not clear why these correlations appear at a higher temperature for the larger clusters.

6.10 Conclusions

First of all, from the temperature scan on both clusters, one has to conclude that μSR data do not show any indication for a quantum size effect. The development with temperature for both clusters is actually very similar.

Attempts to fit the data, with models based on whether the muon is situated in either the Pd-core or form a muonated radical in the ligands, were inconclusive. It should be noted that the data did not give rise to an analysis with an odd/even distribution.

For both situations however, an indication for the local field or the hyperfine interaction at the muon site could be deduced. For the muon in the Pd-core, the quenching of the depolarization with an applied magnetic field, results in a magnetic field distribution of 0.3 mT. Although the odd/even distribution is not apparent from the raw spectra, a dipole calculation based on a 1 μ_B per every other cluster, gave comparable results.

In the case of a muonated radical in the ligands, analysis of the repolarization curve of the initial asymmetry gives a hyperfine interaction of approximately 48 mT.

A proposed 0.2 T internal field, based on susceptibility data on identical cluster, cannot be of dipolar origin. It could be due to super-exchange interaction via the two ligand shells involved.

A good explanation for the temperature dependence of the depolarization rate remains to be found. The increase at lower temperatures is probably related to an increase of magnetic correlation between the nano-clusters. At high temperatures the decrease might be related to a decrease of the susceptibility.

For further studies on these systems one should consider some favorable specifications for a candidate cluster. First of all, the cluster should have a well characterized magnetic moment. Preferably larger than 1 μ_B, and not related to QSE, in order to rule out any uncertainty on this matter. This might *e.g* be composed of a transition metal. The sample should order magnetically above 10 K, so a cryostat with fly-past can be used over the temperature range of interest. Furthermore, it should have identical or no ligands, in order to compare with the Pd-clusters. Such an ideal candidate sample would allow observation of the oscillation related to the magnetic order. Additionally, at higher temperature these oscillations will convert in a depolarization function. This study could give more insight in the muon site and/or a distribution over muon sites. In the light of these experiments it would then be interesting to re-examine the data presented in this chapter.

Bibliography

[1] L.J. de Jongh (ed) *Physics and Chemistry of Metal Cluster Compounds* (Klumer, New York, 1994).

[2] R. Kubo, J. Phys. Soc. Japan **17**, 975 (1962).

[3] G. Schmid (ed) *Clusters and Colloids. From theory to Applications* (VCH, Weinheim, 1994).

[4] C. Kittel *Introduction to Solid State Physics* (John Wiley & Sons, Inc., 1986)

[5] N.W. Ashcroft and N.D. Mermin *Solid State Physics* (Saunders College Publishing, 1976)

[6] L.P. Gor'kov and G.M. Éliashberg, Sov. Phys .JETP **21**, 940 (1965)

[7] Y.E. Volokitin, *Electrons and phonons in nanocluster materials*, Thesis, Leiden University (1997)

[8] J. Sinzig, *Magnetism of nanometer-sized Particles*, Thesis, Leiden University (1997)

[9] R. Denton, B. Mülschlegel and D.J. Scalapino, Phys. Rev. B **7**, 3589 (1973)

[10] Y. Volokitin, J. Sinzig, L.J. de Jongh, G. Schmid, M.N. Vargaftik, and I.I. Moiseev, Nature **384**, 621 (1996); see also N&V in the same journal, page 612.

[11] F.M. Mulder, T.A. Stegink, R.C. Thiel, L.J. de Jongh and G. Schmid, Nature **367**, 716 (1994)

[12] P.M. Paulus, A. Goossens, R.C. Thiel, A.M. van der Kraan ,G. Schmid and L.J. de Jongh, Phys. Rev. B, *to be published*

[13] A.D. Huxely, P. Dalmas de Réotier, A. Yaouanc, D. Caplan, M. Couach, P. Lejay, P.C.M Gubbens and A.M. Mulders, Phys Rev. **B54** R9666 (1996)

[14] F.L. Pratt, Phil. Mag. Letters, **75**, 371 (1997)

[15] S.L. Lee, S.H. Kilcoyne and R. Cywinsky, *Muon Science, Muons in Physics, Chemistry and Materials* , Oxford 1965

[16] C. Nützenadel, A. Züttel, D. Chartouni, G. Schmid and L. Schlapbach, Eur. Phys. J. D **8** 245 (2000)

[17] H. Conrad, G. Ertl and E.E. Latta, Surf. Sci **41**, 435 (1974)

[18] *CRC Handbook of Chemistry and Physics*, edited R.C. Weast, M.J. Astle and W.H. Beyer, (CRC Press Inc., Florida, 1984)

[19] E.B. Karlsson, *Solid State Phenomena as Seen by Muons, Protons and Excited Nuclei*, (Clarendon Press, Oxford, 1995).

[20] O .Hartmann, Hyperfine Interact. **64**, 641 (1990)

[21] R.E. Walstedt and L.R. Walker, Phys. Rev. B **9**, 4857 (1974).

[22] Y.J. Uemura, T. Yamazaki, D.R. Harshman, M Senba and E.J. Ansaldo, Phys. Rev. B **31**, 546 (1985).

[23] S.J. Blundell, A. Husmann, Th. Jestädt, F.L. Pratt, I.M. Marshall, B.W. Lovett, M. Kurmoo, T. Sugsano, W. Hayes Physica B **289-290**, 115 (2000).

[24] D.A. van Leeuwen, J.M. van Ruitenbeek, G. Schmid and L.J. de Jongh, Phys. Lett. A **170**, 325 (1992)

Chapter 7

General conclusions and future prospects

Up to a few years ago, muon spin rotation/relaxation was used as a complementary technique in the study of intermetallic magnetic materials within the Mössbauer group of the Interfacultaire Reactor Institute (IRI). Application of μSR, however, covers a wider range of scientific disciplines. A shift in scientific interest within the department away from metallic magnets, focused attention on possible alternative deployment of μSR. In an attempt to gain more insight into these applications and their possibilities to obtain unique and/or complementary information on properties of interest, some exploratory studies were made. This indicates the objectives and the relationship between these different compounds throughout this thesis.

In order to combine the exploration with relevant and scientifically interesting topics, the compounds studied here were selected from other research projects within the department. The materials were selected based on their known properties as measured by other experimental techniques and possible application of μSR as described in the literature. Although these new deployments of μSR are described in literature and are as such not innovative, here they have been used in relatively unexplored disciplines. Furthermore, these types of experiments have not been done before in the Netherlands, and thus contribute on this on a national level to the knowledge of and expertise on μSR.

7.1 μSR technique on the three compounds studied

In the previous three chapters, we have focused on the different compounds, their properties, our initial intentions, expectations and the information obtained with μSR. Here we will review the insights on μSR technique gained for the three different studies. Some specific difficulties will be addressed and considerations for future studies are given. Additionally, implemented and future improvement on μSR set-ups will be discussed in the next section, together with some future prospects.

7.1.1   Li$^+$ diffusion in Li$_x$[Mn$_{2-y}$Li$_y$]O$_4$

The interest in Li$_x$[Mn$_{2-y}$Li$_y$]O$_4$ stems from its possible application as cathode material in Li ion batteries. Here one would like to obtain insight in the transport and or diffusion of the Li$^+$ charge carriers. The motivation to include μSR in the study, was threefold. First of all the material was known to order magnetically around T_M=25 K, which can easily be monitored by μSR. But more interestingly, the muon often being used to study atomic hydrogen behaviour, might also mimic the dynamic properties of the relatively light Li atom. On top of that the Li motion can be studied with μSR via its nuclear magnetic moment. The latter option is only possible if fluctuating electronic moments on the Mn atoms do not obscure the nuclear contribution. Fortunately this was the case this compound, although fluctuations were observed in the related LiMnCl$_4$. The μSR data have been analyzed and interpreted assuming a static muon and the onset of Li diffusion at specific temperatures, which reduces the depolarization (see chapter 4). The quenching with a 10 mT field, supports the nuclear origin of the depolarization. The Gaussian shaped depolarization function, suggests a quasi-static muon if the strong collision approximation is valid here.

One could argue why the muon is static over the whole temperature range, whereas the Li starts to diffuse. Lord *et al.* in their study on Li$_2$O, assumed a mobile muon [1]. Here the muon hops back and forth between a limited number of sites. The model assumes a correlation between successive local fields at the muon sites. This is in conflict with the commonly used strong collision approximation (SCA), and therefore might effectively give a different depolarization function P$_z$(t). For SCA, P$_z$(t) gives a simple exponential, whereas for motion over a limited number of correlated sites P$_z$(t) could be more or less Gaussian, averaging over the local fields involved. As far as we know, no real study on this is published in the μSR literature, and thus the latter effective Gaussian lineshape is still under discussion. It is evident though that in the limit of a large number of muon sites visited, the SCA model will eventually be reached. It would be worthwhile to study the influence of muon dynamics over a restricted number of sites on the shape of the depolarization function. This would give information on the validity of the SCA model as a function of muon sites visited, or even better on the average distance traveled by the muon. For this purpose extensive Monte Carlo simulations will be needed over a large number of events monitoring the muon spins on a random walk in locally correlated fields.

A recurring problem with interpretation of μSR data is the muon site, as is even more clearly demonstrated for the Pd clusters. In the analyzes of Li$_x$[Mn$_{2-y}$Li$_y$]O$_4$ data could be explained with a distribution of the muon over two sites. Although muon distributions over different sites have been observed before [2], one could still argue why the muon does not prefer a single site. This is especially unsatisfactory since interpretation of the temperature

dependent data and the muon site are interwoven. One would prefer to determine the muon site independently. For metallic compounds the muon site is often determined with μSR Knight shift measurements. An illustrative example is given in $GdNi_5$ [2]. Here the symmetry of the muon site can be obtained from angular scans. The temperature dependence along the different axes, combined with susceptibility data determine the dipolar interaction. Both of these can be used to locate the muon site. However, such measurements require a paramagnetic single crystal sample. Here $Li_x[Mn_{2-y}Li_y]O_4$ could only be produced in nano crystalline powder.

μSR is sensitive over a wide range of time-scales, overlaps and interconnects time-scales of other nuclear probe techniques such as neutrons, Mössbauer and NMR. For $Li_x[Mn_{2-y}Li_y]O_4$, studies with the latter three techniques were performed within the department and at the NMR facility in Nijmegen. Here 2D NMR results have been interpreted with a model of Li atoms hopping between $8a$ and $16c$ sites on time-scales between 1 and 10 msec [3]. Since this technique directly probes the moving Li atoms, its arguments are rather convincing. The model of Li atoms jumping between neighboring sites on the millisecond time scale, however, seems in conflict with μSR results. Here the Li nuclear contribution is assumed to average out on a time scale of microseconds. This discrepancy has up to this moment not been resolved. It has been proposed that the reduced depolarization around 230 K, is in fact induced by a charge ordering transition. This random charge ordering has been observed with neutron scattering on these compounds. A picture of a mechanism reducing the depolarization by charge ordering of the muon surrounding is not obvious to the author. This option, however should not be disregarded in attempts to harmonize neutron, NMR and μSR results.

At the moment μSR studies on similar Li charge carrier systems continue. Proposals have been written and beamtime allocated for industrial Li battery materials. Furthermore a study is started on the Li dynamics in Li loaded $Li_{0.7}TiO_2$. This material finds its application in solar cells. Again these materials are only available in powder, which complicates the analysis as was mentioned above. In future a muon spin resonance experiment will be initiated. This alternative muon technique may be able to separate nuclear contribution, and focus on the Li dynamics. This could give insight and/or evidence into the whereabouts of the muon sites, and eventually help to solve the discrepancy with NMR.

Besides that preliminary attempts have been made with *ab initio* calculations simulating the muon as a light proton, to assist in assigning plausible muon sites within these materials. Here reliable computations do require insulator compounds. To gain expertise and confidence in this method, a few materials with well known muon sites should be considered. These could be obtained from literature.

7.1.2 Reorientational dynamics of ferrocene in KY zeolite

The deployment of μSR in the study on ferrocene in KY zeolite was initiated by work done by Roduner *et al.* on molecular dynamics. They used avoided level crossing μSR in a study of fullerenes and adsorbed benzene molecules. The development of the lineshapes with temperature is rather different for C_{60} as compared to C_{70}. The lineshapes were successfully modeled with two different types of dynamics. For C_{60} a spherical rotational diffusion was obtained whereas the axis of rotation for C_{70} wobbles over a limited angle [4]. For benzene adsorbed to a silica surface and in ZSM-5 zeolite a similar study provided

information on its dynamics [5].

To study molecular dynamics in zeolite, the model system of ferrocene in KY zeolite was used. Initially it was assumed that the ferrocene molecule might hop between the cations surrounding the supercage. This system has a good overlap with the compounds mentioned above, and thus an ALC-μSR study was initiated.

However, the ALC-spectra of ferrocene in KY zeolite proved to be much more complex. Comparison with ALC data on polycrystalline ferrocene by Jayasooria *et al.* showed that the increased complexity is mainly due to the ferrocene adduct. The reason for this is twofold. First, the molecular symmetry properties of both C_{60} and benzene cause all muon adducts to be identical. Ferrocene with it lower symmetry, can host three different muon adducts. Overlap of related peaks obviously complicates the spectra.

Secondly, in contrast to C_{60} and benzene, ferrocene incorporates the transition metal iron atom. This allows for additional interaction such as spin orbit coupling, which is absent in organic materials. The data have been analyzed with such a model (see chapter 5). Additional and separate proof of the existence of a muon metal adduct is needed here. An ALC study on deuterated ferrocene shows that the dominant peak assigned to a metal adduct is not effected by the deuteration [6].

Again, separate information on the origin, number and distribution of muon sites, would be valuable for an interpretation of the data. One way to obtain this information in these organic radical materials is via satellite peak positions in the frequency spectra of TF-μSR experiments [7]. This however, restrains the samples to single crystal or liquefied form. At the moment the option of a liquid ferrocene sample is being considered, to back up the present model.

Zero and longitudinal field measurements on polycrystalline ferrocene show two contributions. Combined with the ALC data, one contribution is assigned to a muon adduct to the iron, the other to a ring adduct. Maxima in the relaxation versus temperature scan, have been analyzed with an Arrhenius law. For polycrystalline ferrocene, the activation energy corresponds to those observed with NMR and QENS. For ferrocene in KY zeolite a clear increase is observed, which is related to the interaction with the zeolite. For both compounds a difference between the ring and iron adduct is observed. This is an indication that, although the muon does not change the ferrocene molecules moment of inertia, addition does effect the electronic properties.

A continuation of the study on ferrocene, will include ALC measurements below 0.1 T. These will be hard to observe, because repolarization to full asymmetry only starts here. A newly planned ALC instrument at ISIS, will be an asset for this study (see section 7.2).

7.1.3   Small magnetic moments on Pd nano-clusters

The interest in Pd nano clusters stems from the fact that they form an intermediate between atomic and bulk metal behaviour. The Quantum size effect (QSE) models this transition. Here the average level spacing in the particle decreases with increasing particle size. Magnetic susceptibility and specific heat, on a sequence of cluster sizes, could satisfactorily be analyzed with this model [8]. Interpretation of these bulk measurement data are based on two assumptions. Half of the clusters carry a 1 μ_B magnetic moment due to an delocalized electron in the cluster core. This gives the usual paramagnetic susceptibility, which is inversely proportional to temperature. The other half do not carry a moment. Furthermore a 0.2 T internal field was needed to explain the maxima in the

susceptibility data.

A μSR study was initiated here, because it is very sensitive to the small magnetic dipole field induced by the delocalized electron in the Pd-core. Additionally, the muon is a local probe and as such it could provide separate proof for an odd/even distribution over the cluster. The effect of cluster size and the 0.2 T field, were expected to be observable as well.

As the results and interpretation in chapter 6 have shown, no clear evidence for QSE could be obtained from the μSR results. Nor could spectra be divided into components related to an odd or even electron number contribution. The data however, were able to exclude the appearance of a 0.2 T field, because this would induce either oscillations or a strong depolarization; none of these were observed.

The Pd clusters are composed of a palladium core, surrounded by a shell of stabilizing oxygen atoms and ligands at the Pd surface. The muon can thus reside either in the Pd core or form muonated radicals in the ligands. Another option could be that the muon locates at the surface. The attempts to analyze the data based on the location of the muon site, have been described extensively in chapter 6. These were based on μSR signals expected from the different muon sites. For the Pd core, a model including a magnetic field distribution related to the 1 μ_B moment on half of the particles was used. Here a field exceeding the local field at the muon site is used to quench the depolarization. Muons in the ligands are assumed to form muonated radicals. Here relaxation is due to perturbation induced transitions. In order to identify and separate a contribution due to the ligands, measurements on the bare ligand material were made. Interpretation of the spectra however, remained complicated, and an attempt to locate the muon site based on these spectra proved to be inconclusive. It should be noted that effects of the surface, the oxygen or the bonding of the ligands to the surface, could not be measured separately.

Theory for μSR on muons in inorganic crystalline materials compared to muonium or muonated radicals, have developed separately, and are presented apart in chapter 3. To the knowledge of the author, no theoretical examination on combined systems is available in the literature. D. Gatteschi *et al.* have illustrated the opportunities for μSR on molecular magnets and magnetic nanoparticles [9]. Apart from organic magnetic materials, this also includes some ligand stabilized molecular clusters based on transition metals. Here however, one either observed oscillations, which are a clear sign of magnetism, or one was able to satisfactorily fit the data with a stretched exponential. The latter fit indicated that the muons are distributed over several sites. The convenience of stretched exponential fits however, is rather disputed, because they could cover up incorrect data characterization, see comments on Ref [10]. Furthermore, it should be noted that fits on raw spectra data are rarely shown in literature on these compounds, whereas in this work plausible models have been rejected based on the poor quality of the fits.

Altogether one could say that studies on molecular clusters is a relatively new and developing science for μSR. The combination of (transition) metal and organic ligands can give rise to new interactions, as was observed in ferrocene. Although internal magnetic fields have been observed in similar molecular systems, no indisputable evidence was found in the Pd clusters. Here we can conclude that the Pd clusters were probably too complex a system to start with. A continuation should select a less complex cluster, in order to gain more expertise and insight on these systems. Here two approaches are considered:

First of all, one could look for an organic-inorganic magnetic molecule with a less complex structure. Here a highly symmetric molecule would be preferred, because this

reduces the number of different muon sites. Furthermore, the muon site in the ligands should be obvious or at least identifiable. Also the absence of a 'crystalline' core would be preferential, since this again reduces the number of muon sites, and avoids the controversy between interstitial muon and muonated radicals. Last but not least, the transition element should carry a well established magnetic moment, which is within the range of μSR. This ideal sample can give information on the influence of magnetic ordering on the depolarization function of muonated radicals in these samples. The expertise will be very useful for further studies in this topic.

On the other hand, one may consider to continue on a cluster sample related to the Pd clusters. Here again, the magnetic moment should be well characterized and established and lie within the range of the spectrometer. This avoids any discussion on the presence and/or other origin of the magnetic moment involved. Magnetic ordering would be preferred in order to observe the μSR spectra develop from an oscillating signal in its depolarization function related to magnetic fluctuations.

A search for a suitable candidate material will probably not give a sample meeting all specifications. These have only been listed to optimize the changes on good results. Deviations on these requirements should, however, be carefully considered up on starting a new study.

7.2 Spectrometer improvements and future prospects

Over the last decade lots of improvements on the μSR facilities at ISIS and PSI have been made. First of all muon fluxes and reliability of the muon beams have increased, due to improved performance of the accelerators. The number of available spectrometers has increased. And both institutes have grown towards user facilities with proposal based beamtime allocation. Next to that, efforts have been made to improve the sample environment. This specifically refers to the cryogenic equipment available. Also during the four years of the PhD project recorded in this thesis, a few important advances have been achieved.

The installation of the MORE set-up on the πM3 beamline (see section 2.3.2) extends the applications of the GPS and LTF spectrometers, to longer time scales. Together with the continuous beam mode, the whole μSR time window is now combined within one spectrometer. Given a temperature range under study, this would allow for studies on both sides of the frequency and relaxation spectra, for a given compound. Apart from some anomaly at the first few time channels, analyses with MORE set-up could provide valuable information on sample parameters such as asymmetry and depolarization level. These are valuable as a first estimate needed for analyzing in the continuous beam set-up, for which the detector dependent background complicates analyses.

Main advances however were made on the background reduction, allowing for smaller samples to be measured. At both ISIS and PSI, the spectrometers have been equipped with fly-past facilities. On GPS this is done by logical coincidence electronics. At EMU the flow cryostat was given an outgoing window and an increased flight path behind the sample. These facilities even outdated some previous experiments on particularly the Pd cluster sample. Although we did not explore the very limits of these fly-past options, at least we have been able to measure samples down to 5 mm cross section and 50 mg in weight.

The reduced demands on sample weight and size offers new opportunities. Samples are often only available in small amounts, such as *e.g.* the Pd cluster compounds. On the other hand, single crystal materials can provide an extra dimension to the data interpretation. It may allow for measurements along the different axis, determination of the muon site, and comparison with bulk techniques such as magnetic susceptibility. In the past we performed measurements on mosaics of oriented slices of spark eroded lined up single crystals. These slices have typical dimensions of 5 mm, thus nowadays a single slice is sufficient. This allows for experiments studying the effect of an electric current on the flux line lattice. Such an experiment on a $NbSe_2$ single crystal by Dalmas de Réotier *et al.* is in progress. In general the reduced demands on the sample size makes μSR accessible for samples of higher quality and preferred state. This eventually provides more information and allows for a better founded analyses.

A new branch to the tree of μSR techniques uses the low-energy muons. Here surface muons are moderated to epithermal energies ($\sim$1-30 eV) and can afterwards be reaccelerated. In future this could could lead to deposition of muons at a well defined depth in the sample. This allows for application in thin films, multilayered structures and surfaces, which are playing an increasingly important role in science and technology. At the moment the flux on both the continuous beam at PSI and the pulsed facility at ISIS is rather limited [11, 12]. Progress on this aspect is made and the technique will become available for routine user facility experiments in near future.

Provision of a second neutron target station will be combined with an upgrade of the ISIS accelerator to increase the operating beam current from 200 μA to 300 μA. The resulting increased muon flux combined with detector segmentation, to prevent dead time, should increase the data rate by an order of magnitude. Additionally, attempts will be made to improve the maximum precession frequency/relaxation rate by time-slicing of the muon pulse. Replacements of beamline quadrupoles will decrease the spot size at EMU increasing the potential for smaller sample usage. Last but not least, the development and installation of a new instrument is proposed for 2003. The new instrument will be equipped with a high-field superconducting solenoid magnet, allowing for longitudinal fields over 5 T. This introduces techniques such as repolarisation/quenching scan and avoided level crossing resonance to the facilities at ISIS. Furthermore, the apparatus will be fully equiped for RF-μSR. Before, this technique was only available at the development beamline DEVA. It offers double resonance to decouple muon nuclear interactions, and rotation frequencies well beyond the normal ISIS limit. All these developments will improve current studies and open up new science areas for μSR.

In the far future, the European Spallation Source (ESS) will be realized. This project is now in the research and development phase, studying accelerator, target and instruments required. Although designed as a neutron source, this project will all most certainly include a muon source as a spin off from the accelerator facility. However, this 21st century facility will not be operational before 2010.

Summarizing one can say that at both PSI and ISIS, improvements have and will be implemented. Efforts have been made to increase the frequency and relaxation range of the spectrometers: towards higher rates for the pulsed source, and towards lower rates for continuous beams. Next to that, the number of μSR techniques available and the number of spectrometers will increase at both facilities. Finally, improvements in the sample environment and beamline allow for smaller samples to be studied. All together, this offers opportunities for new sciences and a bright future.

Bibliography

[1] J.S. Lord, S.P. Cottrell and W.G. Williams, J. Phys.: Condens. Matter **10** 7975 (1998)

[2] A.M. Mulders, C.T. Kaiser, P.M.C. Gubbens, A. Amato, F.N. Gygax, M. Pinkpank, A. Schenk, P. Dalmas de Réotier, A. Yaouanc, K.H.J. Buschow, F. Kayzel and A. Menovsky, Physica B **289-290** 451 (2000)

[3] V.W.J. Verhoeven, I.M. de Schepper, G. Nachtegaal, A.P.M. Kentgens, E.M. Kelder, J. Schoonman, and F. Mulder, Phys. Rev. Lett. **86** 4314 (2001)

[4] E. Roduner, K. Prassides, R.M. Macrae, I.M. Thomas, C. Niedermayer, U. Binninger, C. Bernhard, A. Hofer and I.D. Reid, Chem. Phys. **192** 231 (1995)

[5] E. Roduner, M. Stolmár, H. Dilger and I.D Reid, J. Phys. Chem. A **102** 7591 (1998)

[6] U.A. Jayasooria, private communication

[7] E. Roduner and H. Fischer, Chem. Phys. **54** 261 (1980)

[8] Y. Volokitin, J. Sinzig, L.J. de Jongh, G. Schmid, M.N. Vargaftik, and I.I. Moiseev, Nature **384** 621 (1996); see also N&V in the same journal, page 612.

[9] D. Gatteschi, P. Carreta and A. Lascialfari, Physica B **289-290** 94 (2000)

[10] A. Lascialfari, P. Carreta, D. Gatteschi, C Sangregorio, J.S. Lord and C.A. Scott, Physica B **289-290** 110 (2000), Physica B **289-290** 94 (2000)

[11] E. Morenzoni, H. Glückler, T. Prokscha, H.P. Weber, E.M. Forgan, T.J. Jackson, H. Luetkens, Ch. Niedermayer, M. Pleines, M. Brike, A. Hofer, J. Litterst, T. Riseman and G. Schatz, Physica B **289-290** 653 (2000)

[12] K. Träger, A. Bretirück, M. Diaz Trigo, A. Grossmann, K. Jungmann, J. Merkel, V. Meyer, P. Neumayer, B. Pachl, G. zu Putlitz, R. Santra, L. William, G. Allodi, C. Bucci, R. de Renzi, F. Galli, G. Guidi, T. Shiroka, G.H. Eaton, P.J.C. King, C.A. Scott, G.W. Williams, E. Roduner, R. Scheuermann, M.C. Charlton, P. Donnelly, L. Pareti and G. Turilli, Physica B **289-290** 662 (2000)

Diffusion, reorientation and small magnetic fields

studied by μSR

by C.T. Kaiser

Summary

Muon Spin Rotation and Relaxation, collectively known as μSR, has become an increasingly popular and accessible probe of condensed matter in the last decade. Here the muon, an elementary particle, is introduced by implantation in the compound under study. Through its spin the muon interacts with the local magnetic field. Consequently μSR provides fundamental and often unique information on both static and dynamic properties of the local magnetic field. For this reason μSR has occasionally been used to support studies on intermetallic magnetic materials within the department of Neutron scattering and Mössbauer spectroscopy at the Interfacultair Reactor Institute in Delft. The possible applications of μSR, however, cover a wider range of topics. It is commonly used to study flux distributions in superconductors, heavy fermions, diffusion processes in metals and semiconductors, and the dynamics of muonated radicals. The aim of the presented work was to explore the possibilities of μSR to provide complementary information on some of the research projects within our department. For this purpose three different compounds, originating from various scientific disciplines and interests, have been studied.

Materials of the composition $Li_x[Mn_{1.96}Li_{0.04}]O_4$ are very promising as cathode for Li batteries. For this reason one is interested in detailed information on the nature of the Li transport. A μSR study was started to fill up the μs time window between NMR and neutron scattering. Here two powder samples with $x = 0.2$ and $x = 1$, corresponding to a charged and empty state, were studied. For both samples a magnetic transition below $T_M \simeq 25$ K due to ordering of the manganese was observed. At temperatures above 50 K, the Gaussian lineshape of the spectra and the quenching of the depolarization with a 10 mT magnetic field, prove that the depolarization is due to a static field distribution induced by the nuclear moments on the Li and Mn nuclei. Above T=230 K, a

large decrease of the width of the static field distribution at the muon site is found for Li[Mn$_{1.96}$Li$_{0.04}$]O$_4$. For Li$_{0.2}$[Mn$_{1.96}$Li$_{0.04}$]O$_4$ a similar decrease is observed above 300 K. Dipole field calculations were able to reproduce the depolarization rate levels at either side of the transition. Here the muons are distributed over the 8a and 16c sites, and the contribution of Li nuclear moments is averaged to zero at the high temperature end, due to motional narrowing. An alternative picture, in which the muon starts to visit equivalent sites with in the same tetrahedral surrounding, was considered but did not give results corresponding to the levels observed in the experiment. Altogether we have observed the onset of Li^+ diffusion on a microsecond time scale in Li[Mn$_{1.96}$Li$_{0.04}$]O$_4$ at 230 K and in Li$_{0.2}$[Mn$_{1.96}$Li$_{0.04}$]O$_4$ at 300 K.

The interest for reorientational dynamics of molecules in the zeolite host frames stems from promising applications in heterogeneous catalysis. For this reason a model system of ferrocene in the supercage of KY zeolite has been studied extensively with NMR, Mössbauer spectroscopy and neutron scattering. From avoided level crossing μSR studies on a related system of benzene in NaY zeolite, Roduner *et. al* were able to obtain the characteristic geometry of the dynamics from the ALC lineshapes. Similar experiments on ferrocene in KY zeolite, however, gave a more complex accumulation of ALC peaks. The development the ALC lineshapes with temperature could not be related to any of the simulated spectra for several geometry models for the dynamics, such as the reorientational jumps of the molecular axis between the cations located at the edges of the supercage. Comparison with data on polycrystalline ferrocene revealed an equivalent development of the dominant ALC peak with temperature. Together with μSR relaxation data, this behaviour could be explained with a spin-orbit interaction for a muon adduct to the iron atom. Remaining ALC peaks and a second contribution in the relaxation data have been assigned to a muon ring adduct. From the temperature development of the relaxation rate, the Arrhenius parameters, activation energy and attempt frequency were obtained. These have been compared with similar values obtained from NMR and QENS, on both polycrystalline ferrocene and ferrocene zeolite. This suggests that the dynamics probed here is the rotation of the cyclopentadienyl ring around the five fold molecular axis. Both the activation energy obtained with QENS and μSR imply a decreased mobility of the ferrocene in KY zeolite as compared to polycrystalline ferrocene. This is probably due to the interaction of the cyclopentadienyl rings with the cations. Although the small muon mass hardly changes the moment of inertia, the muon initiated radical electron does disrupt the dynamics. For ferrocene this depends on the nature of the muon adduct. For the muon metal adduct the molecular rotation is less effected than for the muon ring adduct. This is probably due to a more intense interaction with the cations of the latter adduct.

Nanosize metallic particles are under study for a wide range of both scientifically and technologically important properties. One more fundamental study is the correlation between particle size and electronic properties, which mark the transition between atomic and bulk metal behaviour. A theoretical description suggests despite complex surface interaction an energy gaps between discrete levels statistically distributed around an average value. The width of this gap depends on the clusters size and the related theory is referred to as the Quantum Size Effect (QSE). For nanosize particles thermal energies comparable to this average gap are in the order of 1 to 100 K. At these temperatures drastic effects on the magnetic properties are expected, depending on whether a clusters contains an odd or even number of conduction electrons. Here an odd number will result in paramagnetic behaviour with an effective moment of 1 μ_B, due to an delocalized electron in the highest

occupied level. In contrast, an even number leads to a non-magnetic cluster. Specific heat and magnetic susceptibility measurements by Volokitin and Sinzig have confirmed thermodynamic properties predicted by QSE on a collection of monodisperse Pd clusters. Furthermore they predict the existence of a 0.2 T magnetic field.

Motivation for a μSR study stems from the fact that the muon is extremely sensitive to small dipolar fields, and is a local as opposed to bulk probe. Measurements have been performed on $Pd_{55}[PPh_3]_{12}O_{30}$ and $Pd_{561}Phen^*_{36}O_{200}$ samples, with predicted energy gaps of $\approx$100 and 10 K, respectively. Zero field μSR spectra could be fitted satisfactorily with a single exponential. Despite the local probe character of the muon, the spectra did not give rise to an analysis including an odd/even electron number distribution over the clusters. The development with temperature of the depolarization rate of the μSR spectra show two characteristic temperatures for each cluster. Comparison between related temperatures of both clusters, did not show correlation with the cluster size as was predicted by QSE.

Longitudinal magnetic field experiments were performed, in an attempt to determine the origin of the depolarization. The different nature of muon sites interstitial in the Pd core and muon adducts in the ligands, complicated the analysis. No conclusive evidence was found that the muon is located exclusively in either of these components. If the muon resides in the Pd, quenching of the depolarization rate with an applied field, suggest a field distribution in the order of 0.3 mT. This is in the order of magnitude as can be expected for a dipolar field distribution due to 1 μ_B magnetic moments on neighbor clusters. For a muonated ligand the influence of such a small moment is unknown. For both muon sites it can be stated a 0.2 T dipolar field is not apparent in these clusters. A super-exchange interaction cannot be ruled out here.

Diffusie, heroriëntation en kleine magnetische velden

onderzocht m.b.v. μSR

door C.T. Kaiser

Samenvatting

Muon Spin Rotatie en Relaxatie, gezamenlijk bekend onder de noemer μSR, is in de afgelopen tien jaar een veel gebruikelijker en toegankelijker meetmethode geworden in vaste stof onderzoek. Deze meettechniek is gebaseerd op het muon, een elementair deeltje, dat door implantatie geintroduceerd wordt in de te onderzoeken verbinding. De wisselwerking tussen de spin van het muon en het magnetisch veld levert fundamentele en vaak ook unieke informatie over zowel de statische en dynamische eigenschappen van het lokale magnetisch veld. Om deze reden is μSR af en toe gebruikt als ondersteunende techniek bij het onderzoek aan magnetische intermetallische materialen binnen de vakgroep van Neutronen verstrooiing en Mössbauer spektroskopie op het Interfacultair Reactor Instituut in Delft. De mogelijke toepassing van μSR, bestrijkt echter een groter scala van onderwerpen. Zo wordt het bijvoorbeeld regelmatig toegepast bij onderzoek aan flux verdelingen in supergeleiders, zware fermionen, diffusie processen in metalen en halfgeleiders, en bij de dynamica van door muon geinitieerde radicalen. Doel van dit werk was het verkennen van de mogelijkheden die μSR bied tot het geven van extra ondersteunende informatie bij een aantal van de onderzoeksprogrammas binnen onze afdeling. Om deze reden zijn drie materialen vanuit verschillende wetenschappelijke disciplines en belangstelling bestudeerd.

Materialen van de samenstelling $Li_x[Mn_{1.96}Li_{0.04}]O_4$ zijn veelbelovend voor toepassing als kathode voor Li batterijen. Men is voornamelijk geinteresseerd in gedetailleerde informatie over de wijze van het Li transport. Een μSR studie is opgestart om het μs tijdsvenster gebied tussen NMR en neutronen verstrooiing op te vullen. Twee poeder monsters met x=0.2 and x=1 zijn bestudeerd, overeenkomend met respectievelijk een geladen en ontladen toestand. Voor beide monsters werd beneden $T_M \approx$25 K een magnetische overgang waargenomen, veroorzaakt door het ordenen van de elektronische momenten op het mangaan. Boven de 50 K is de vorm van de spectra Gaussisch en wordt

de depolarisatie volledig onderdrukt met een 10 mT magnetisch veld. Dit toont aan dat de depolarisatie geinduceerd wordt door een statische veld distributie van de nucleaire momenten op the Li en Mn kernen. Voor $Li[Mn_{1.96}Li_{0.04}]O_4$ is een grote afname van de breedte van deze veld distributie boven de $T=230$ K waargenomen. Een zelfde afname is gezien in $Li_{0.2}[Mn_{1.96}Li_{0.04}]O_4$, boven $T=300$ K. De depolarisatie niveaus aan beide zijden van de overgang konden worden gereproduceerd met behulp van dipool berekeningen. Verondersteld is dat de muonen gedistribueerd zijn over zowel the $8a$ en $16c$ positie. Boven de overgang wordt de bijdrage van de Li kernmomenten uitgemiddeld tot nul, ten gevolge van diffusie. Daarnaast is een alternatieve verklaring, waarbij een muon enkele malen equivalente plaatsen binnen dezelfde tetraderische omgeving bezoekt, overwogen. Deze konden echter niet de experimenteel waargenomen depolarisatie snelheden reproduceren. Samengevat hebben we de aanzet van Li^+ diffusie waargenomen op een microseconde tijdschaal, voor $Li[Mn_{1.96}Li_{0.04}]O_4$ boven 230 K en voor $Li_{0.2}[Mn_{1.96}Li_{0.04}]O_4$ boven 300 K.

Belangstelling voor de dynamica van herориёnterende moleculen in zeoliet structuren komt voort uit veelbelovende toepassingen in de heterogene katalyse. Dit is de aanleiding van een uitgebreid onderzoek aan een model systeem van ferroceen in de superkooien van KY zeoliet, waarbij gebruik is gemaakt van NMR, Mössbauer spectroscopie en neutronen verstrooiing. Roduner *et. al* hebben aangetoond dat voor een gerelateerd systeem van benzeen in NaY zeoliet, de karakteristieke geometrie van beweging kan worden afgeleid uit de vorm van de ALC piek. Soortgelijke experimenten aan ferroceen in KY zeoliet, leveren echter een gecompliceerd signaal van samengestelde pieken. De ontwikkeling van deze ALC lijnvormen met temperatuur, kon niet worden gerelateerd aan een van de gesimuleerde spectra die enkele mogelijke geometrieёn van de beweging beschrijven. Onder deze gesimuleerde bewegingen valt onder andere de sprongsgewijze herориёntatie van de moleculaire as over de aan de randen van de superkooi gelegen cationen. De verschuiving van de meest prominente ALC piek met toenemende temperatuur komt over een met die gevonden in polykristallijn ferroceen. Samen met μSR relaxatie data, kan dit gedrag worden verklaard met een spin-baan koppeling van een aan het ijzer atoom gebonden muon. De overige ALC pieken en een tweede bijdrage aan de relaxatie, kunnen worden toegeschreven aan muonen gebonden aan de cyclopentadienylringen. Uit de temperatuur afhankelijkheid van de relaxatie zijn Arrhenius parameters zoals de activeringsenergie en de pre-exponentiёle factor de verkregen. Deze zijn vergeleken met soortgelijke waarden verkregen met NMR en QENS aan zowel polykristallijn ferroceen en ferroceen in zeoliet. Dit suggereert dat de hier waargenomen dynamica de rotatie van de cyclopentadienyl ring om de vijftallige moleculaire as. Zowel de activeringsenergie gevonden met QENS als met μSR impliceren een afgenomen mobiliteit van het ferroceen in zeoliet in vergelijking met polykristallijn ferroceen. Dit wordt hoogst waarschijnlijk veroorzaakt door de interactie van de cyclopentadienylringen met de cationen. Alhoewel het lichte muon nauwelijks het traagheidsmoment verandert, verstoord het door het muon geinitieerde ongepaarde elektron wel degelijk de dynamica van het molecuul. Bij ferroceen in KY zeoliet is dit afhankelijk van de binding van het muon aan het ferroceen. Voor een muon gebonden aan het metaal is de moleculaire rotatie minder beinvloed dan voor een muon aan de ring. Dit is waarschijnlijk te wijten aan de intensievere interactie met de cationen in het laatste geval.

Metallische deeltjes met de omvang van slechts enkele nanometer worden onderzocht vanwege een groot aantal zowel wetenschappelijke als technologisch belangrijke eigenschappen. Een meer fundamenteel gericht onderzoek houd zich bezig met de correlatie

tussen deeltjes grootte en elektronische eigenschappen, welke de overgang tussen atomair en bulk gedrag markeren. Een theoretische beschrijving veronderstelt, ondanks complexe interacties met het oppervlak, een statistische verdeling van de energiesprong tussen twee niveaus rondom een gemiddelde waarde. De grootte van deze sprong is afhankelijk van de grootte van de clusters en de bijbehorende theorie staat bekend onder de naam van Quatum Size Effect (QSE). Voor nano deeltjes komt deze energiesprong overeen met temperaturen van rond de 1 tot 100 K. Bij deze temperaturen zijn drastische effecten van de magnetische eigenschappen te verwachten, afhankelijk of een cluster een even of oneven aantal geleidingselektronen bezit. Een oneven aantal resulteert in een paramagnetisch gedrag met een effectief moment van 1 μB, veroorzaakt door een gedelokaliseerd elektron in the hoogst bezette niveau. Dit in tegenstelling tot het niet magnetische cluster in het geval van een even aantal elektronen. Soortelijke warmte en magnetische susceptibiliteit metingen van Volokitin en Sinzig aan een verzameling van monodisperse Pd clusters, bevestigen de het thermodynamisch gedrag zoals voorspelt was door QSE. Daarnaast veronderstellen zij een 0.2 T magnetisch veld om hun data te kunnen verklaren. De motivatie voor de inzet van μSR komt voort uit the feit dat het muon uiterst gevoelig voor kleine dipool velden. Bovendien meet μSR de lokale eigenschappen in tegenstelling tot bulk gedrag. Metingen zijn gedaan aan monsters van $Pd_{55}[PPh_3]_{12}O_{30}$ en $Pd_{561}Phen^*_{36}O_{200}$, met een verwachte energiesprong van respectievelijk $\approx$100 en 10 K. Nul veld μSR spectra konden goed worden beschreven door een enkele exponentiële functie. Ondanks het lokale meetkarakter van het muon, gaven de spectra geen aanleiding tot een analyse waarbij een verdelingen over clusters met een even/oneven aantal geleidingselektronen noodzakelijk was. De temperatuur afhankelijkheid van de depolarisatie snelheid vertoont twee karakteristieke temperaturen voor beide clusters. Een onderling vergelijk van deze temperaturen vertoont geen correlatie met de cluster grootte zoals die voorspelt door QSE. Aanvullende metingen met een longitudinaal magnetisch veld zijn gedaan in een poging de oorsprong van de depolarisatie te achterhalen. De analyse hiervan werd gecompliceerd door de verschillende aard van een mogelijk interstitieel gelokaliseerd muon in de Pd kern en/of een muon gebonden aan de liganden. Er kan geen sluitend bewijs worden gegeven dat het muon exclusief in een van beide componenten aanwezig is. Verondersteld dat het muon in het Pd verblijft, kan worden afgeleid uit de onderdrukte depolarisatie bij een zwak magnetisch veld, dat de variantie van het magnetisch veld in de orde van 0.3 mT is. Dit ligt in dezelfde orde van grootte als de verwachtte distributie bijdrage door 1 μ_B op omliggende clusters. Voor de invloed op een muon gebonden aan het ligand is de invloed van een klein veld onbekend. Voor beide muon posities kan wel gezegd worden dat met μSR een dipool veld van 0.2 T niet is waargenomen in deze clusters. Dit sluit echter het bestaan van een super-exchange interactie niet uit.

Dankwoord & Thanks

Curriculum Vitae

Carlo Kaiser werd op 3 oktober 1971 geboren te Noordwijkerhout. Daar doorliep hij vanaf 1984 het voortbereidend wetenschappelijk onderwijs aan het College Leeuwenhorst. Na het eindexamen begon hij in 1990 aan de studie Technische Natuurkunde in Delft, waarvan hij in 1992 het propedeutisch examen behaalde.

Zijn afstudeer project vond plaats onder supervisie van prof. L.A. de Graaf bij de toenmalige vakgroep Stralingsfysica van het Interfacultiar Reactor Instituut. Onder directe begeleiding van drs. W.H. Kraan werd verkennend onderzoek gedaan naar de mogelijkheden van de Larmorprecessie techniek in een neutronendiffractie experiment. Als testcase werd hierbij de spanningsverdeling over de doorsnede van een gebogen aluminium staaf bepaald.

Aansluitend begon hij in 1996 met een promotieonderzoek binnen de afdeling Neutronen verstrooiing en Mössbauer spectroscopie onder begeleiding van prof. G.J. Kearely en dr. P.C.M. Gubbens. Hierbij is gekeken naar de mogelijke toepassing van muon spin rotatie/relaxatie binnen het onderzoek van deze afdeling. De resultaten van dit onderzoek zijn vastgelegd in dit proefschrift. Gedurende 2 jaar heeft hij voor zijn onderwijstaak practica begeleid van de cursus stralingshygiëne, zowel op de lokatie in Delft als in Utrecht.

$$\star \quad \star \quad \star$$

List of publications

C.T. Kaiser, P.C.M. Gubbens, E. Kemner, A.R. Overweg and U.A. Jayasooriya, *Dynamics of ferrocene in KY zeolite studied with μSR*, to be published

A. Yaouanc, P. Dalmas de Réotier, P.C.M. Gubbens, C.T. Kaiser, A.A. Menovsky, M. Mihalik and S.P. Cottrell, *Evidence for a weak quasi-static magneitc component in UGe$_2$*, to be published.

P.C.M. Gubbens, C.T. Kaiser, P. Dalmas de Réotier, A. Yaouanc, S.P. Cottrell, A.A. Menovsky and M. Mihálik, to be published.

A.M. Mulders, P.C.M. Gubbens, C.T. Kaiser A. Amato, F.N. Gygax, P. Dalmas de Réotier, A. Yaouanc, K.H.J. Buschow, F. Kayzel and A.A. Menovsky, *Muon spin dynamics and sites in GdNi$_5$* Hyperfine Interactions, in press.

A.M. Mulders, P.C.M. Gubbens, C.T. Kaiser A. Amato, F.N. Gygax, P. Dalmas de Réotier, A. Yaouanc, K.H.J. Buschow, F. Kayzel and A.A. Menovsky, *Muon localization along a six fold ring shaped site and muon quantum hopping in GdNi$_5$* J. of Alloys and Comp., submitted.

P. Dalmas de Réotier, A. Yaouanc, R.H. Heffner, J.L. Smith, P.C.M. Gubbens and C.T. Kaiser, *Muon spin rotation and relaxation measurements on single crystals of the heavy fermion superconductor UBe$_{13}$*, Phys. Rev. B, 61 (2000) 6377

P. Dalmas de Réotier, A. Yaouanc, P.C.M. Gubbens, C.T. Kaiser, A.M. Mulders, F.N. Gygax, A. Schenck, A. Amato, C. Baines, A. de Visser, R.J. Keizer, P. Bonville, P.J.C. King, A. Huxley and A.A. Menovsky, *Magnetism and superconductivity of UPt$_3$ by muon spin techniques*, Physica B, 289-290 (2000) 10-14.

A.M. Mulders, C.T. Kaiser, P.C.M. Gubbens, A. Amato, F.N. Gygax, M. Pinkpank, P. Dalmas de Réotier, A. Yaouanc, K.H.J. Buschow, F. Kayzel and A.A. Menovsky, *Positive muon diffusion and localization sites in GdNi$_5$*, Physica B, 289-290 (2000) 451-454.

A. Yaouanc, P. Dalmas de Réotier, F.N. Gygax, A. Schenck, A. Amato, C. Baines, P.C.M. Gubbens, C.T. Kaiser, A. de Visser, R.J. Keizer, P. Bonville, A. Huxley and A.A. Menovsky, *Evidence for two magnetically inequivalent regions in UPt$_3$*, Phys. Rev. Lett., 84 (2000) 2702.

C.T. Kaiser, V.W.J. Verhoeven, P.C.M. Gubbens, F.M. Mulder, I. de Schepper, A. Yaouanc, P. Dalmas de Reéotier, S.P. Cottrell, E.M. Kelder and J. Schoonman, *Li Mobility in the battery cathode material $Li_x[Mn_{1.96}Li_{0.04}]O_4$ studied by muon spin depolarization*, Phys. Rev. B, 62 (2000) R9236.

C.T. Kaiser, V.W.J. Verhoeven, P.C.M. Gubbens, P. Dalmas de Réotier, A. Yaouanc and S.P. Cottrell, *Technological applications of μSR: Li Mobility in the battery cathode material $Li_x[Mn_{1.96}Li_{0.04}]O_4$*, ISIS98 Annual report CLRC ("Highlights") (2000), p. 60.

A. Yaouanc, P. Dalmas de Réotier, P.C.M. Gubbens, C.T. Kaiser, P. Bonville, J.A. Hodges, A. Amato, A. Schenck, P. Lejay, A.A. Menovsky, and M. Mihalik, *μSR investigation of the quasi-elastic magnetic excitations in strongly correlated compounds*, Physica B 259-261 (1999) 126

P. Dalmas de Réotier, A. Yaouanc, P.C.M. Gubbens, C.T. Kaiser, A.M. Mulders, S.P. Cottrell and P.J.C. King, *Duality in strongly correlated f-electron intermetallics*, ISIS98 Annual report CLRC ("Highlights") (1998) 52. W.H. Kraan, C.T. Kaiser, M.Th. Rekveldt, *High-resolution neutron diffraction using Larmor precession*, J. Appl. Crystallogr, 31 (1998) 742

W.H. Kraan, C.T. Kaiser, M.Th. Rekveldt, *Neutron diffraction using Larmor precession*, Physica B, 234-236 (1997) 1163

$\star$ $\quad$ $\star$
$\star$